©2013

Matthew Frank Parkinson

ALL RIGHTS RESERVED

ARCHITECTURAL INFLUENCE OF FEF_2 FILMS ON ELECTROCHEMICAL FAILURE MODES

By

MATTHEW FRANK PARKINSON

A Dissertation submitted to the

Graduate School-New Brunswick

Rutgers, The State University of New Jersey

in partial fulfillment of the requirements

for the degree of

Doctor of Philosophy

Graduate Program in Materials Science and Engineering

Written under the direction of

Professor GLENN G. AMATUCCI

And approved by

_____

_____

_____

_____

New Brunswick, New Jersey

May, 2013

ABSTRACT OF THE DISSERTATION

ARCHITECTURAL INFLUENCE OF FEF_2 FILMS ON ELECTROCHEMICAL FAILURE MODES

By MATTHEW FRANK PARKINSON

Dissertation Director:

Glenn G. Amatucci

Iron fluoride (FeF_2) is an attractive material for use as nanocomposite conversion reaction based cathodes in lithium ion batteries because of its high specific theoretical capacity of 571mAh/g. However, despite the optimistic potential of FeF_2 to advance battery cathodes, the cycling performance of the material requires further development for it to be a viable cathode candidate. A deeper understanding is required of how orientation, selective reaction fronts, and morphology impact the electrochemical performance. FeF_2 films of various degrees of vertical porosity and thickness were fabricated through the use of dynamic glancing angle deposition. Respectable performance was obtained with film thicknesses of 850nm, well above the nanodimensions typically required to trigger electrochemical activity. The structure – electrochemical property relationships were used to formulate insights on the electronic and ionic transport limitations seen in typical nanocomposite powders.

Dedication

This thesis is dedicated to the many that have provided me with support, inspiration, encouragement and love throughout my lifetime.

I believe there are no rewards without sacrifice and this dissertation was no exception. My wife Ashley is a wonderful human being that has supported my education in endless ways despite the short term sacrifices it has required from our relationship. I am grateful for her love and support. I am confident this education will make our family stronger as we move forward with our future filled with new opportunity, new priorities and happiness.

I would not have been able to achieve this dissertation with the support of my parents, two sisters, extended family and friends. I am blessed to have two inspirational parents who have lead me to success through passing their own unique life guiding principles along to me. My two elder sisters have supported me in many ways through my life including being my early academic tutors. I am grateful for my family's support and love.

Finally, I would like to acknowledge some of my early teachers who were inspirational and encouraging; Don Crockett one of my science teachers at Novi High School and the amazing engineering professors at Michigan Technological University. These teachers were largely responsible for igniting my passion for science and engineering.

Acknowledgements

I would like to thank the Material Science and Engineering Department for the opportunity to pursue my educational aspirations. Most importantly, I would like to thank my advisor Professor Glenn Amatucci for welcoming a mechanical engineer into his highly regarded energy storage research group (ESRG) and being patient with my scientific development. Professor Amatucci is an extremely dedicated scientist and professor. His endless commitment and passion for his research field sets an inspiring example for the road map to achievement. I would like to thank the graduate program director and committee member Professor Lisa Klein for the opportunity to join the department and her dedication to my education. I would like to thank my committee member Professor Ahmad Safari and the other Professors that have taught the coursework with excellence. In addition, I would like to thank Professor Kimberly Cook-Chennault for being on my committee.

There are many energy storage research group (ESRG) team members that without their support this thesis in its form would not have been possible. I would like to especially thank my fellow graduate student Jonthan Ko for his support with lab activities. In addition, I would like to thank the highly talented and always eager to assist engineers Barry Vaning and John Gural. Barry and John have contributed many innovated ideas supporting the design and development of the custom ebeam deposition chamber which was the foundation of this thesis. I would like to thank past student Dr. Andrew Gmitter for his willingness to assist me in the lab whenever it I needed his support. I would like to thank Sheel Sanghvi for his support with XRD and depositing the LiPON coating to the electrodes. In addition, I would like to thank the

following past and present members; Kimberly Scott, James Kantor, Dr. William Yourey, Anthony Ferrer, Josh Kim, Dr. Wei Tong, Dr. Nathalie Pereira, Anna Halajko, Fadwa Badway, Irene Plitz, and Linda Sung.

I acknowledge the U.S. Government and the Northeastern Center for Chemical Energy Storage (NECCES), an Energy Frontier Research Center funded by the U.S. Department of Energy, Office of Science, Office of Basic Energy Sciences under Award Number DE-SC0001294, for their financial support.

Table of Contents

ABSTRACT OF THE DISSERTATION ..... **ii**
Dedication ..... **iii**
Acknowledgements ..... **iv**
Table of Contents ..... **vi**
List of Figures ..... **viii**
List of Tables ..... **xiv**
1. Introduction **1**
1.1. Introduction to Lithium Batteries 1
1.1.1. General Lithium Cell Overview and Terminology 1
1.1.2. Lithium Cell Cathode Materials 3
1.1.3. Thin Film Batteries Brief Review 11
1.1.4. Metal Fluoride Thin Film Electrodes 13
1.1.5. Iron Fluoride (FeF_2) Thin Films 17
1.1.6. 3D Nanostructured Electrodes 18
2. **Electrochemical Impedance Spectroscopy (EIS)** 21
2.1. Theory 21
2.1.1. Double Layer Capacitance 21
2.1.2. Randles Impedance Nyquist Plot and AC Impedance Equivalent Circuit 23
2.1.3. Constant Phase Element (CPE) 26
2.2. Practical Applications 30
2.2.1. Charge Transfer Impedance and Diffusion 30
2.2.2. Electrolyte Accessible Surface Area 33
3. **Physical Vapor Deposition (PVD) Thin Films** 35
3.1. Introduction 35
3.2. Vacuum Pumps 36
3.3. Vacuum Measurement 39
3.4. Physical Vapor Deposition Processing 40
3.4.1. Source Vaporization Techniques 41
3.4.2. Vapor Flux Transport 45
3.4.3. Film Nucleation and Growth 46
3.4.4. Glancing Angle Deposition (GLAD) 50

4. Experimental Techniques 54
4.1. Preparation of the Thin Film Substrate and Current Collector 54
4.2. Programming of the Dynamic Substrate Drum System 55
4.3. X-Ray Diffraction (XRD) 57
4.4. Stylist Profilometer Thin Film Thickness Measurement 61
4.5. Field Emission Scanning Electron Microscope (FESEM) 64
4.6. Electrochemical Characterization 66
5. Design and Fabrication of a Custom E-beam Deposition System 67
5.1. Project Background 67
5.2. Vacuum Chamber Preparation, Assembly and Testing 69
5.3. Design of a Programmable Substrate Drum System 75
5.4. Design of an Electron Beam Deposition System 81
6. Effect of Vertically Structured Porosity on Electrochemical Performance of FeF2 Films 93
6.1. Introduction 93
6.2. Experimentation 97
6.3. Results 101
6.4. Discussion 123
6.5. Conclusion 131
7. Effect of FeF2 Thin film Microstructure on Surface Specific Capacitance 132
7.1. Introduction 132
7.2. Experimentation 138
7.3. Results 141
7.4. Discussion 154
7.5. Conclusion 155
8. Future Work 157
9. Summary 158
10. References 159
11. Curriculum vitae 165

List of Figures

Figure 1.1: Schematic of a typical coin cell battery 2

Figure 1.2: Schematic of the inner workings of an insertion LIB 5

Figure 1.3: Visual comparison of the three types of cathodes 7

Figure 1.4: FeF_2 rutile-type tetragonal structure showing the diffusion barrier contrast between the (110) and (001) channel 8

Figure 1.5: Thin film battery by Oak Ridge National Lab 11

Figure 2.1: Ions from solution forming a double layer capacitance within a porous electrode 23

Figure 2.2: Randles impedance Nyquist plot and equivalent AC circuit 24

Figure 2.3: Impedance plots for various shapes of pores 26

Figure 2.4: CPE equivalent circuits, a) non-porous and b) porous electrodes 28

Figure 2.5: Schematic of a pore with smooth walls and its represented Nyquist plot 29

Figure 2.6: Schematic of a pore which has porous walls and it's represented Nyquist plot. 30

Figure 2.7: Ideal conducting electrodes equivalent RC circuit and Nyquist plot 31

Figure 2.8: Ideal polarizable electrodes equivalent RC circuit and Nyquist plot 31

Figure 2.9: Nyquist plots of cells (a) balanced bulk and faradaic resistances, (b) more highly conducting electrodes with relatively large bulk resistance, and (c) nearly blocking electrodes with relatively small bulk resistance 33

Figure 2.10: Definition of pore type showing macro, meso and micro pores 35

Figure 3.1: Cutaway view of a typical Cryo-Torr pump 38

Figure 3.2: Effective pressure monitoring ranges of various vacuum gauges 40

Figure 3.3: Typical resistance heated thermal evaporation system 41

Figure 3.4: Typical pulse laser evaporation system 42

Figure 3.5: Typical glow discharge sputtering evaporation system 43

Figure 3.6: Typical electron beam evaporation system 44

Figure 3.7: Comparison of short verse long mean free 45

Figure 3.8: Cosine distribution of vapor particles leaving a point on the source 46

Figure 3.9: Steps in film growth 48

Figure 3.10: Step #4 in Film Growth, Heterogeneous Nucleation 49

Figure 3.11: Typical glancing angle deposition apparatus 51

Figure 3.12: Glancing angle shadow effect 52

Figure 3.13: Description of various GLAD 53

Figure 4.1: Substrate holder showing attached Al-7075 strips and glass slide 54

Figure 4.2: Typical manual hand press used to punch the substrate/film into discs 55

Figure 4.3: Ormec servo motion controller assembly and wiring diagram 56

Figure 4.4: NaCl unit cell showing atomic planes 57

Figure 4.5: Definition of Bragg's law 59

Figure 4.6: Definition of diffraction peak intensity 59

Figure 4.7: X-ray diffractometer used for the majority of XRD experiments a Bruker D8 61

Figure 4.8: Dektak 150 Profilometer used to measure film thickness and topography 63

Figure 4.9: Dektak 150 Profilometer3D topography mapping of a 58-62° FeF2 thin film 64

Figure 4.10: A Zeiss ΣIGMA Field Emission SEM used in the experiments 65

Figure 4.11: Solartron Models SI 1287 and SI 1260 used for EIS in the experiments ... 67

Figure 5.1: Previously used multiple chamber web coater 68

Figure 5.2: Detailed planning schedule for the vacuum chamber development 70

Figure 5.3: Completed ebeam deposition chamber valve switch panel 71

Figure 5.4: Removal and welding of the web coater chamber backing plate to create an individual custom chamber 73

Figure 5.5: FEA simulation of chamber backing plate L-bracket support 74

Figure 5.6: 2D Fabrication drawings of the substrate drum system 75

Figure 5.7: Substrate drum positional resolution calculation 77

Figure 5.8: Schematic of a ferrofluidic driveshaft 78

Figure 5.9: CAD showing the substrate drum in minimum height position 79

Figure 5.10: CAD showing the substrate drum in its maximum height position with 185mm of total vertical adjustment 79

Figure 5.11: Disassembly for drum geometry modifications 80

Figure 5.12: Completed fabricated substrate drum system 81

Figure 5.13: Picture of the completed ebeam deposition system 83

Figure 5.14: Results of a titanium deposition showing substrate thickness distribution 86

Figure 5.15: View of chamber with the substrate drum rotated in GLAD position 87

Figure 5.16: Joule cross section polisher 88

Figure 5.17: FESEM images of a titanium 55° GLAD film deposited with the substrate held at a 55° angle relative to horizontal base of the ebeam..... 89

Figure 5.18: XRD results confirming single phase synthesis of FeF2 thin film 90

Figure 5.19: XRD results of FeF2 a.) without Ti adhesion layer and b.) with Ti layer ... 92

Figure 6.1: Lithited film structures (a) classical static film and (b) porous dynamic film 96

Figure 6.2: Schematic comparing static verse dynamic deposition 99

Figure 6.3: XRD results (a) dynamic angular films (b) 48-52° dynamic films and (c) static films..... 103

Figure 6.4: FESEM images of Static 400nm (a) 2kX (b) 35kX, Static 700nm (c) 2kX (d) 35kX, and Static 850nm (e) 2kX (f) 35kX 105

Figure 6.5: FESEM images of 0.65rpm 28°-32°(a) 2kX (b) 35kX, 38°-42°(c) 2kX (d) 35kX, 48°-52°(e) 2kX (f) 35kX, 58°-62°(g) 2kX (h) 35kX and 68°-72°(i) 2kX (j) 35kX 107

Figure 6.6: FESEM images of 0.65rpm 48°-52° at 35kX (a) 400nm and (b) 850nm.... 108

Figure 6.7: FESEM images at 35kX of (a) 60°-80° at 6.5rpm (b) 40°-60° at 6.5rpm (c) 40°-80° at 6.5rpm (d) 40°-80° at 16.25rpm and (e) 40°-80° at 26rpm 110

Figure 6.8: Image processing of 0.65rpm at 35kX (a) 28°-32° (5.2%), (b) 38°-42° (8.2%), (c) 48°-52° (19.9%), (d) 58°-62° (26.4%) and (e) 68°-72° (39.2%)..... 112

Figure 6.9: Image processing of static films at 2kX (a) 400nm (1.1%), (b) 700nm (1.9%) and (c) 850nm (1.3%)..... 113

Figure 6.10: Plot of porosity and interfacial area dependence on dynamic deposition angle 114

Figure 6.11: Dynamic rocking angular electrodes (a) specific capacity as a function of cycle number and (b) 1st discharge specific capacity profile..... 117

Figure 6.12: Influence of dynamic deposition angle on perimeter surface area and capacity 118

Figure 6.13: Static vs. Dynamic electrodes (a) specific capacity as a function of cycle number (b) 1st discharge specific capacity profile 120

Figure 6.14: 400nm Static vs. Dynamic electrodes cycled galvanostatically between 4.50 V and 1.0V (a) static deposition (b) 48°-52° dynamic deposition 121

Figure 6.15: 700nm Static vs. Dynamic electrodes cycled galvanostatically between 4.50 V and 1.0V (a) static deposition (b) 48°-52° dynamic deposition 122

Figure 6.16: 850nm Static vs. Dynamic electrodes cycled galvanostatically between 4.50 V and 1.0V (a) static deposition (b) 48°-52° dynamic deposition 123

Figure 6.17: FESEM images of lithiated films Static 400nm (a) 2kX (b) 35kX and Dynamic 48°-52° 400nm (c) 2kX (d) 35kX 126

Figure 6.18: Image processing of Dynamic 48°-52° 400nm films at 35kX magnification (a) pre-lithiated and (b) lithiated 126

Figure 6.19: Voltage vs. Capacity of Static 400nm (a) LiPON=50nm and (b) LiPON=100nm 128

Figure 6.20: Voltage vs. Capacity of 48°-52° 400nm (a) LiPON=50nm and (b) LiPON=100nm 129

Figure 6.21: Voltage vs. Capacity of 48°-52° 700nm (a) LiPON=50nm and (b) LiPON=100nm 130

Figure 6.22: LiPON cells Discharge Capacity vs. Cycle Number (a) Static 400nm (b) 48°-52° 400nm and (c) 48°-52° 700nm 131

Figure 7.1: Ions from Solution forming a Double Layer Capacitance within Porous Electrode 135

Figure 7.2: Randles Impedance Nyquist Plot and AC Impedance Equivalent Circuit . 136

Figure 7.3: XRD results of (a) dynamic (b) 48°-52° 400nm,700nm,850nm (c) Static 400nm, 700nm, 850nm and (d) Static 600nm, 800nm, 1500nm 142

Figure 7.4: FESEM images of Static 400nm (a) 2kX (b) 35kX, Static 600nm (c) 2kX (d) 35kX, and Static 700nm (e) 2kX (f) 35kX, Static 800nm (g) 2kX (h) 35kX, Static 850nm (i) 2kX (j) 35kX and Static 1500nm (k) 2kX (l) 35kX 143

Figure 7.5: FESEM images of 0.65rpm 28°-32°(a) 2kX (b) 35kX, 38°-42°(c) 2kX (d) 35kX, 48°-52°(e) 2kX (f) 35kX, 58°-62°(g) 2kX (h) 35kX and 68°-72°(i) 2kX (j) 35kX. 144

Figure 7.6: Image processing of 2kX FESEM images of Static 400nm (a), Static 600nm (b), Static 700nm (c), Static 800nm (d), Static 850nm (e) and Static 1500nm (f). 145

Figure 7.7: Image processing of 0.65rpm (a) 28°-32° 35kX, (b) 38°-42° 35kX, (c) 48°-52° 35kX, (d) 58°-62° 35kX and (e) 68°-72° 35kX..... 147

Figure 7.8: Plot of static films capacitance verse frequency..... 149

Figure 7.9: Nyquist Plot of Static 400nm 150

Figure 7.10: Plots of static films (a) CPE-T vs. film thickness, (b) interfacial area vs. film thickness and (c) interfacial area vs. CPE-T 151

Figure 7.11: Plot of static films capacitance verse frequency..... 152

Figure 7.12: Nyquist Plot of Dynamic 48-52deg 700nm 153

Figure 7.13: Plot of dynamic films (a) CPE-T vs. deposition angle, (b) interfacial area vs. deposition angle and (c) interfacial area vs. CPE-T 154

List of Tables

Table 1: Conversion vs. intercalation comparison……..6

Table 2: Summary of XRD Analysis……..104

1 Introduction

1.1 Introduction to Lithium Batteries

One of the most important rechargeable energy storage technologies is the lithium ion battery (LIBs). Since early development at Exxon in the 1970's, lithium battery technology has been of interest due to the fact that lithium is the most electropositive (–3.04V versus standard hydrogen electrode) and is the lightest metal (MW=6.94g/mol, and specific gravity 0.53g/cc). Traditionally, LIBs are used for a variety of mobile equipment, including cell phones, laptop computers, and tools. Most recently, LIBs are showing as promising candidates of power sources to electrify the transportation sector.[1]

1.1.1 General Lithium Cell Overview and Terminology

In general, a battery cell such as the one in Fig. 1.1 is a means of storing energy by electrochemistry and transforms chemical energy into electricity by a redox chemical reaction. The battery consists of the anode, anode current collector, cathode, cathode current collector, separator, electrolyte and sealant mechanism to prevent exposure of the chemistry to the atmosphere. The anode is the negative electrode, typically consisting of an electrical conducting material connected to a current collector and is where oxidation occurs, resulting in electrons flowing out into the circuit during discharge. The cathode is the positive electrode typically consisting of an electrical insulating material with fillers such as carbon to improve electrical conductivity which allows discharge. The cathode is connected to a current collector where reduction occurs and electrons flow in from the circuit during discharge. The electrolyte, in the

form of an electrical insulating but ionic conducting liquid, gel or solid such as a polymer, is the passageway to exchange ions (Li^+) back and forth between the anode and cathode. The separator, typically in the form of a porous polymer or paper, is an electronically insulating material placed as a spacer between the positive and negative electrodes necessary to prevent a short circuit condition. The separator can be eliminated from the battery when an electrolyte of solid form with mechanical rigidity is used which has sole capability of adding space between the electrodes to prevent a short circuit.

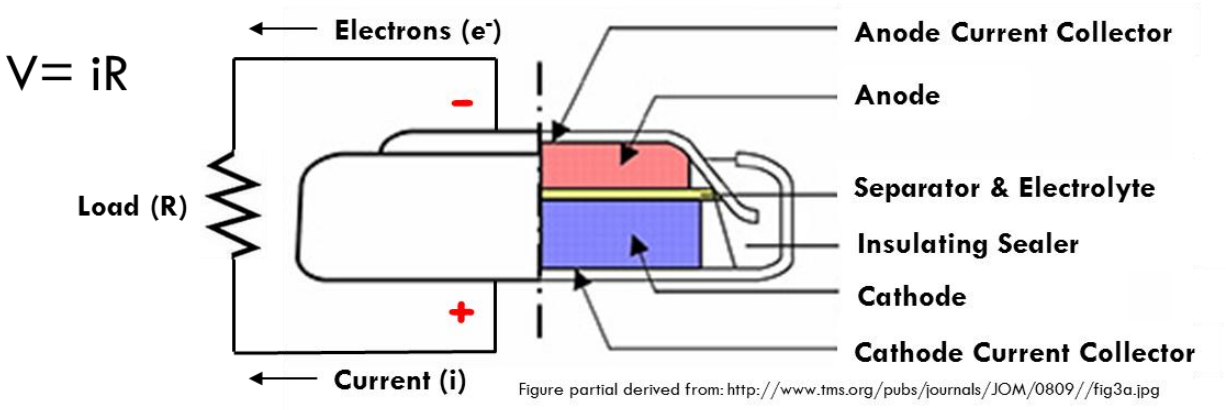

Figure 1.1: Schematic of a typical coin cell battery

Multiple battery cells can be assembly together in a series or parallel circuit arrangement to tailor the performance with a specific application. In applications that require higher operating voltage or higher capacity, multiple cells are arranged in series and parallel respectively.

There are two forms of battery cells, primary and secondary and their definition depends on how they discharged. A primary battery cell is limited to a single discharge due to the form of chemistry used in the cathode. Primary batteries can be found in applications such as medical pacemakers, watches and flashlights. Some advantages

to primary batteries are reduced up front cost compared with secondary batteries which make them ideal for single use applications and they have a relatively higher energy density and longer shelf life because no design compromises are necessary to accommodate recharging. Primary batteries are at a disadvantage due to the cost of continuous replacement which adds to waste streams and they are not suited for high load applications which would add to the frequency of replacement. Secondary batteries which are commonly called rechargeable batteries because of their ability to be charged to their initial energy condition by forcing current and ions in the direction opposite that of discharge. Secondary batteries can be found in applications such as power tools, laptops and hybrid vehicles. Some advantages to secondary batteries are cost efficiency over the long term due replacing less frequently, higher power densities, higher discharge rates under heavy loads and improved cold temperature performance. The limitations of secondary batteries include higher up front cost, poorer charge retention, lower energy density and special design considerations due to lithium's reactivity with oxygen.

1.1.2 Lithium Cell Cathode Materials

There are three known types of reaction mechanisms currently in LIBs, intercalation, displacement and conversion. For all three mechanisms, lithium ion chemistry moves electrons through an external circuit by insertion of Li+ into one electrode material while extracting Li+ from the opposing electrode material. In intercalation, the process is referred to as the "rocking chair" mechanism which is another name for "Li-ion battery".

For intercalation cathodes, lithium ions are reversibly removed or inserted into a host material of a layered or tunneled metal oxide structure. These layers are occupied by a redox active 3d or 1d transition metal which allows lithium insertion while simultaneously reducing the oxidation state of the transition metal within the structure during cell discharge. As a result, the host material experiences insignificant structural changes during the charge/discharge cycle.

, While these cathode materials offer desirable properties such as good cycling life, good rate capability, and high discharge voltages, they are restricted at most to a single electron transfer per formula unit. This restriction limits the energy density that can be achieved with current insertion materials. For example, layered compounds based on $LiCoO_2$ which are currently used in commercial LIBs have specific capacities of 120-150 mA h g-1, about 50% of their theoretical 1 e- transfer value.[2] Fig. 1.2 shows the insertion reaction equation and a schematic of the inner workings of an insertion LIB.[3]

$$LiXXO_y \leftrightarrow Li_{1-x}XXO_y + Li^+ + xe^-$$

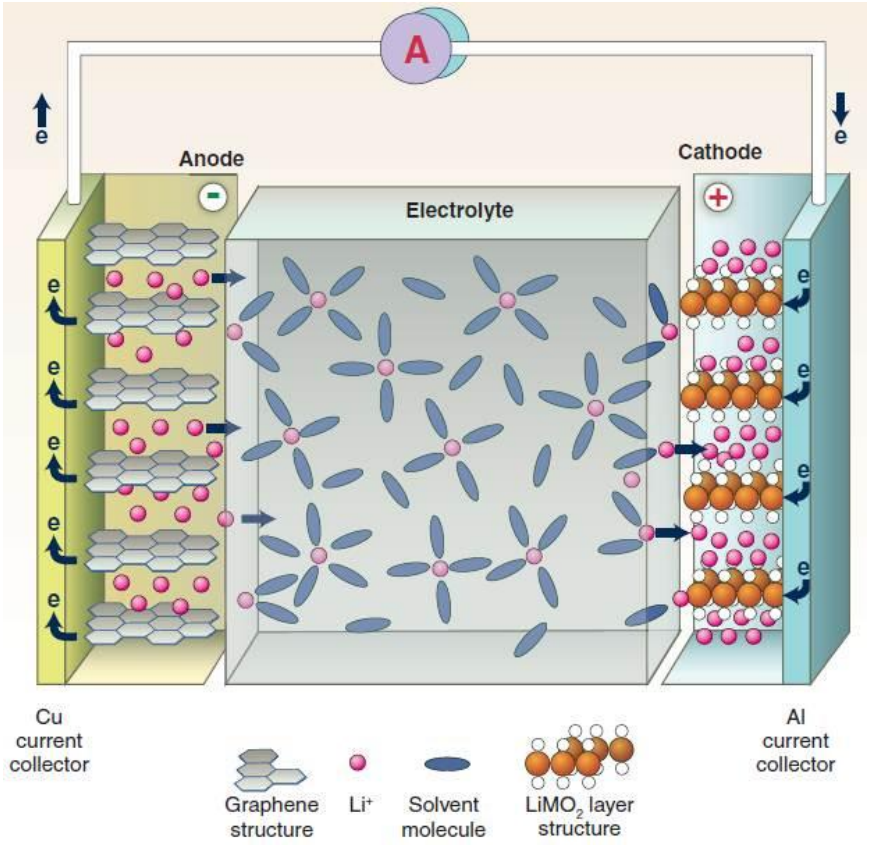

Figure 1.2: Schematic of the inner workings of an insertion LIB[3]

Displacement and conversion materials do not have to possess a layered type crystal structure. However, in contrast to conversion materials the crystal structure does not change during charge and discharge. With displacement, the structure is preoccupied with another mobile cation which is displaced and reduced with the insertion of the first Li^+ and there is full utilization of all the oxidation states of the active transition metal.

An alternative to Li^+ insertion reactions is the displacement or “conversion” reaction in which the active cathode electrode material, MX_y, is consumed by Li^+ and

reduced to the metal, M_0, and a corresponding lithium compound, $Li_{z/y}X$ and oxidation of these should return the material to its initial state.

$$nyLi^+ + M_xX_y + nye^- \leftrightarrow yLi_nX + xM$$

In the conversion reaction equation above, the metal cation is represented by M and the anion by X. A large theoretical energy density is possible because this reaction can make use of all energetically favorable valence states of the metal cation. Although, reversible conversion reactions have been demonstrated with a variety of materials including metal oxides, metal nitrides, metal sulfides, and metal fluorides, only metal fluorides have a high enough potential to be used as Li-ion cathodes.[4] This is due to the fact that the conversion reaction potential is directly proportional to the strength of the ionic bond. Despite metal fluorides high energy density they are limited by their wide band gap corresponding in electronically insulating behavior which has inhibited the use of metal fluoride electrodes when considering large particles. Table 1 compares several metal fluorides cathodes with two common intercalation materials and Figure 1.3 shows a visual comparison of the three types of cathodes.[5]

Compound	Class	E°_{cell} / V	mAh/g	Wh/kg	Ah/L	Wh/L
VF_3	Conversion	1.87	745	1389	2505	4673
CrF_2	Conversion	2.28	596	1360	2287	5224
CrF_3	Conversion	2.29	738	1689	2789	6383
MnF_2	Conversion	1.92	577	1107	2296	4405
MnF_3	Conversion	2.65	718	1902	2543	6732
FeF_2	Conversion	2.66	571	1522	2336	6224
FeF_3	Conversion	2.74	713	1954	2758	7561
CoF_2	Conversion	2.85	553	1578	2466	7039
CoF_3	Conversion	3.62	694	2509	2691	9735
SnF_2	Conversion	2.98	342	1021	1563	4665
α-PbF_2	Conversion	2.83	219	619	1852	5243
o-BiF_3	Conversion	3.13	302	946	2391	7484
T-BiF_3	Conversion	3.13	302	946	2539	7960
Li_xCoO_2	Intercalation	3.95	135-165	530-640	690-840	2700-3250
Li_xFePO_4	Intercalation	3.45	170	586	608	2097

Table 2: Conversion vs. intercalation comparison[5]

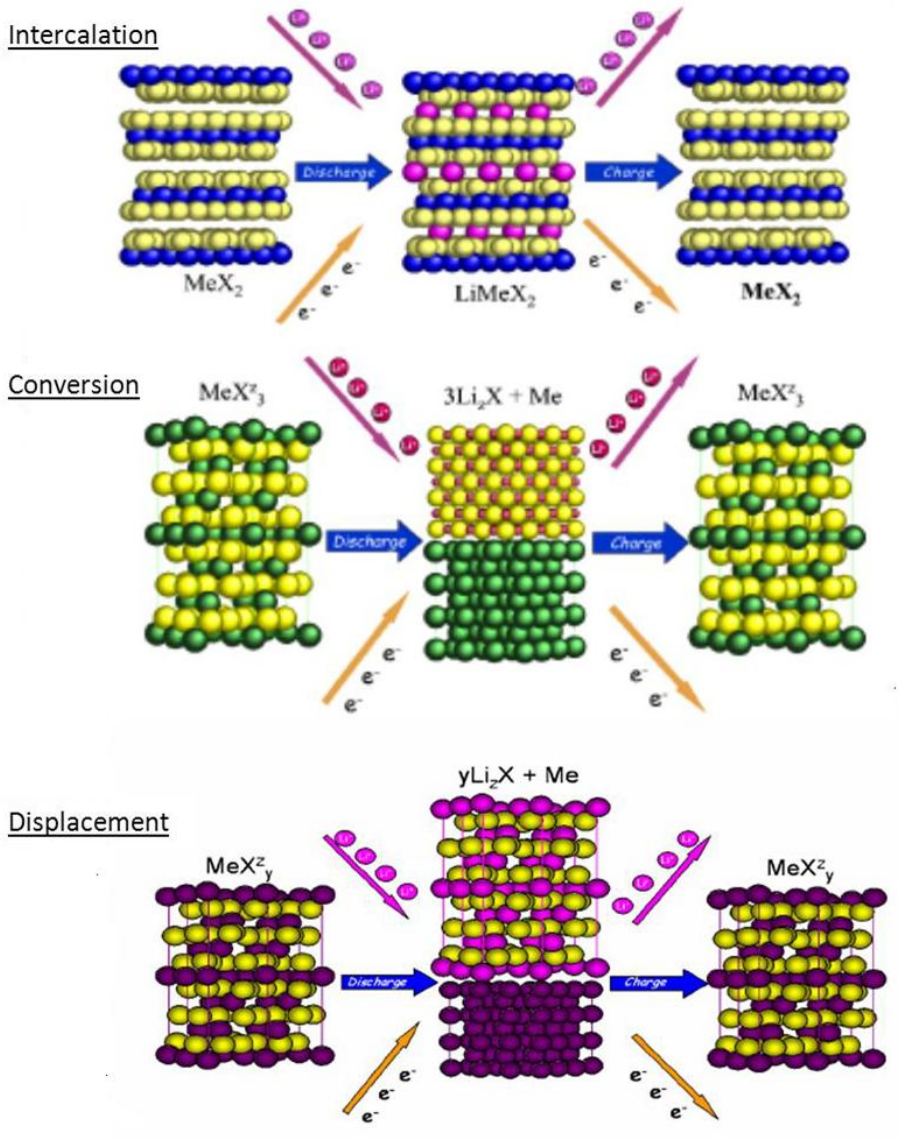

Figure 1.3: Visual comparison of the three types of cathodes[4]

This thesis investigates the conversion cathode material iron fluoride (FeF_2). FeF_2 has a tetragonal structure with space group symmetry P42/mnm. This structure shown in Fig. 1.4 is of the rutile type and is composed of an hcp anion lattice with

cations occupying half of the octahedral sites to form FeF6/3 octahedra. This octahedral link is in an edge-sharing manner along the [001] to form alternating chains of FeF6/3 octahedra and vacant channels. The channels along the [001] can reasonably be expected to accommodate Li^+ in either tetrahedral or octahedral sites.

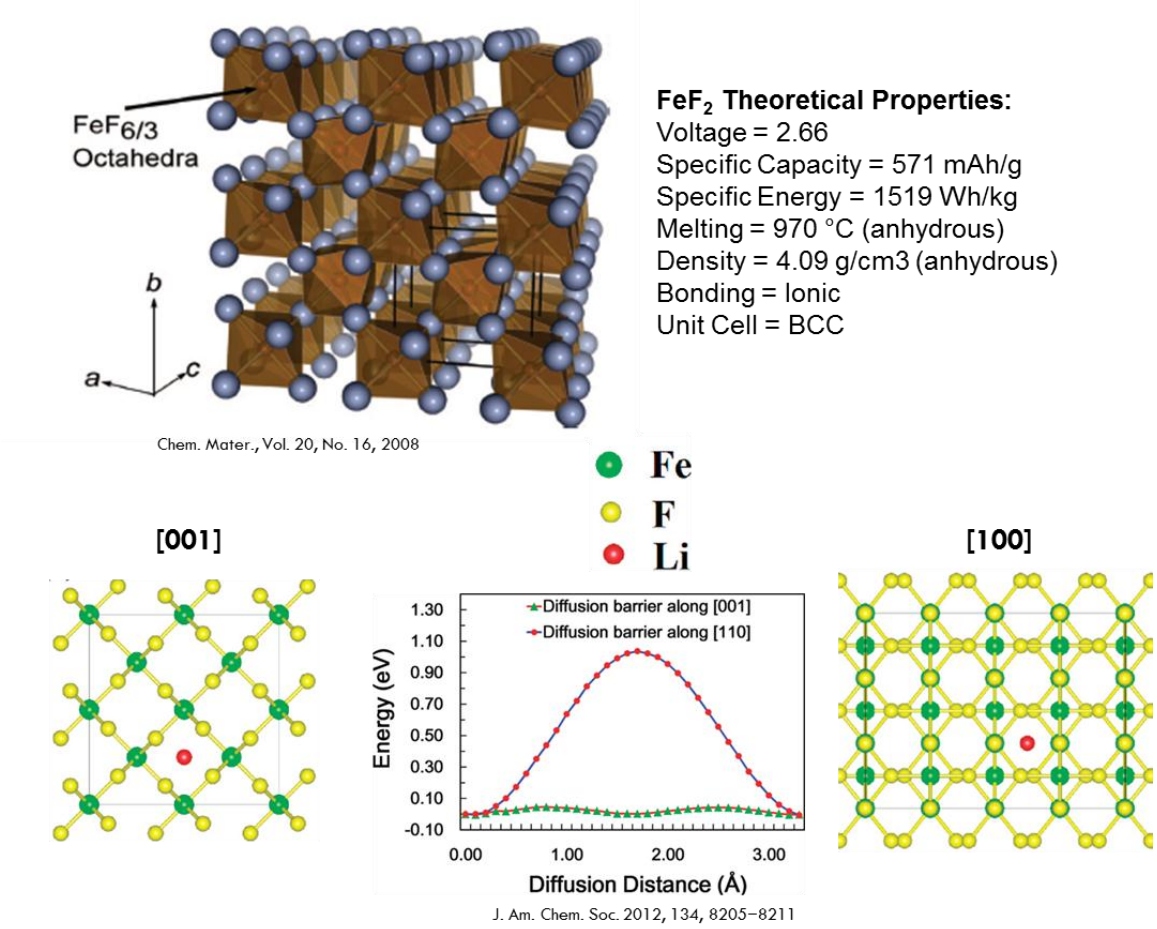

Figure 1.4: FeF_2 rutile-type tetragonal structure showing the diffusion barrier contrast between the (110) and (001) channel[2,6]

In terms of the FeF_2 conversion reaction mechanism, initial Li^+ insertion into FeF_2 is restricted because Fe^{2+} reduction is required. For Li^+ insertion to occur some Fe^{2+} would need to be reduced to either Fe^{1+} or disproportionation to Fe^0 and Fe^{3+} would

need to take place. In general, solid-state Fe^{1+} is very unlikely and oxidation states <2+ are uncommon for elements of the first transition series. If some Fe^{2+} reduction to Fe^{0} combines with some Fe^{2+} oxidation to Fe^{3+}, then metallic iron would likely precipitate out of the iron fluoride structure.[7] In this case, the mechanism would not be a strict insertion reaction because it requires an exchange of iron with lithium. During this process it would be possible for Li^{+} to either fill an interstitial site in the channels, occupy the site that Fe^{0} is removed from, or occupy space that is a combination of both limits. Another possibility exists in which two Li^{+} exchange for one Fe^{2+} of the rutile structure. There are many possibilities in which the FeF_2 structure can be altered during the conversion reaction. One of the goals of this thesis is to discover new knowledge to better understand this reaction mechanism.

Despite metal fluorides representing a route for high energy density positive electrodes, they are limited by their wide band gap corresponding in electronically insulating behavior and very poor ionic diffusion through the conversion front. The band gap and electrical properties of FeF_2 have been recently studied by YANG Zhen-hua et al 2012.[8] For their study, generalized gradient approximation calculations and the Hubbard parameter method described the band gap as 2.565 eV. It was concluded that the bond between Fe and F atoms in FeF_2 is a mixture of ionic bond and covalent bond. Another study, Santos-Ortiz et al 2013, provided insight into understanding of the band structure of FeF_2.[9] Their study used UV-Vis-NIR spectrophotometer, Photoluminescence (PL) and photoluminescence excitation (PLE) characterization. The results indicated that FeF_2 is a direct bandgap, n-type semiconductor, the Hall coefficients were negative, electron mobility was $0.33 cm^2/V.s$ and resistivity was 0.255

>Ω.cm and the band structure was 3.4 eV with a workfunction of ~4.51- 4.66 eV. Based on this band gap information, the study provided a guide for the selection of battery application current collectors (i.e., Ohmic contacts). They concluded that stable, low workfunction metals such as Al (Φ=4.19 eV), Ga (Φ=4.25 eV) or In (Φ=4.1 eV) could provide Ohmic contacts to FeF_2 films and are well suited for use as current collectors.

Due to the fact that FeF_2 is a high bandgap insulator, transport is limited with thick dense electrodes and the conversion reaction must proceed at the point of electron transfer typically near the current collector. However, it has been show that transport in powder FeF_2 electrodes is greatly enhanced by the use of carbon or mixed conducting matrices in combination with metal fluoride domains <30nm.[10,11]

The conversion reaction of FeF_2 proceeds with a rapid transport on the surface of material. This occurs as small metallic iron nanoparticles (<5 nm in diameter) nucleate in close proximity to the converted LiF phase. The iron nanoparticles are interconnected and form a webbed network, which provides a pathway for local electron transport within the insulating LiF phase.[12] There is a massive interface formed between nanoscale solid phases which provide a pathway for ionic transport. Molecular dynamics simulations have shown the limitation that after formation of the LiF crystal, the reaction slows down since fewer lithium ions are able to diffuse to unconverted Fe layers.[6] These simulations have shown that the Li^+ diffusion barrier along the [110] channel is approximately 70% greater than the barrier along the [001] channel and more lithium ions penetrate deeper into the FeF_2 (001) subsurface. The simulations predicted that a complete conversion would require sufficient lithium ions below the formed LiF crystals and Fe^0 clusters in order to convert deeper subsurface Fe.

1.1.3 Thin Film Batteries Brief Review

In the 1990's, research at Oak Ridge National Laboratory (ORNL) led to the development of a new application for thin films, solid state lithium and lithium ion batteries such as the one shown in Fig. 1.5.[13,14,15] By definition, thin film solid state batteries are less than 15 microns thick and have important applications in a variety of consumer and medical products. Thin film batteries are excellent in applications that require a small scale source of power. The advantages of these types of batteries are long shelf life, good reversibility capacity retention, high energy and high power densities.

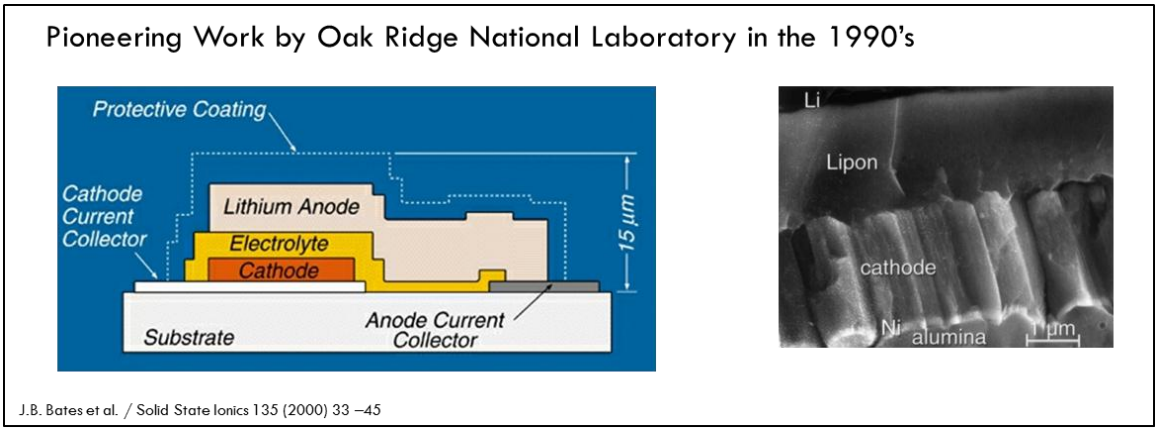

Figure 1.5: Thin film battery by Oak Ridge National Lab[10]

Thin film batteries are typically fabricated by physical vapor deposition process. The batteries are fabricated by sequential depositions in a multiple chamber deposition system. The most common method used deposits onto an insulating substrate such as alumina. The first chamber consists of DC magnetron sputtering which deposits the metal current collectors followed by RF sputtering which deposits the electrical

insulating cathode. Finally, the electrolyte is deposited by RF magnetron sputtering of a Li_3PO_4 source in a nitrogen plasma to create lithium phosphorus oxynitride (LiPON) and metallic lithium anode is deposited by thermal evaporation. In addition, there is a protective layered coating of Ti and parylene C to seal the battery to avoid exposure to the atmosphere.

Lithium Phosphorus Oxynitride (LiPON) is the thin film solid electrolyte invented at Oak Ridge National Laboratory in the early 1990s.[16] Today, LiPON continues to be the most widely used solid electrolyte for thin film batteries. The inventor J. B. Bates had previous knowledge of introducing nitrogen to sodium phosphate and sodium silicate glasses to enhance the chemical and thermal stability of the material and thought the application could be used with lithium glass. Bates found that only a small percentage of nitrogen replaces the oxygen in the composition. However, this small percentage of nitrogen has a substantial effect on the ion conductivity and electrochemical stability. A nitrogen/oxygen ratio of 0.1 in LiPON is associated with an ionic conductivity that is approximately 40 times higher than nitrogen free Li3PO4 but approximately 100 times less than liquid electrolytes. Typically a 1μm thick thin film of LiPON free of pinholes provides sufficient ion conductivity while maintaining an electrical insulating barrier between electrodes.

In addition to fully assembled batteries, thin films have several advantages which can be applied as useful research tools in characterizing the properties of lithium intercalation and conversion compounds. As a research tool the potential advantages of thin films include (i) allowing investigation of electrochemical properties of pure phases being free of binders; (ii) better accommodation of the strain of lithium insertion

and removal which improves cycle life; (iii) investigation of new reactions not possible with bulk materials; (iv) short path lengths for electronic transport (permitting operation with low electronic conducting materials or at higher power); and (v) short path lengths for Li^+ transport (permitting operation with low Li+ conducting materials or at higher power).

1.1.4 Metal Fluoride Thin Film Electrodes

From the theoretical thermodynamic calculations, metal fluoride electrodes show high energy density potential and have been studied for battery applications since the 1960's.[17] Metal fluorides have much higher voltage and the theoretical energy density from the conversion reaction of metal fluorides exceeds that for metal oxides and sulfides. This is due to the high electronegativity of fluorine which allows high ionic bond character with the metal. A vast array of metal fluoride materials have been studied for electrode application primarily comprised of powder verse thin films.[4] The following proceeding paragraphs will make brief reference to a few of these notable chemistries.

One of the highest energy density metal fluoride cathode materials is CuF_2. In 1976 thin film electrodes of CuF_2 were first studied by Hunter and Kennedy.[18] The electrodes were fabricated using Pb metal as anode, PbF_2 as electrolyte. The thin film cells developed open circuit voltages from 0.61 to 0.70V, compared to 0.70V theoretical. The current density at room temperature was >10 ~$\mu A/cm^2$ and showed vast improvement with elevated temperatures. For the room temperature cells, the cathode utilization was typically 30-40% in contrast to powder based CuF_2 electrodes at the time which had approximately 25% and slight improvement with sintering. The poor utilization of most metal fluorides is thought to be explained by their low electronic

conductivity due to their intrinsically high band gaps. The attempts to recharge both thin film and powder electrodes in these studies were unsuccessful. Nearly three decades would past with little research activity reported on CuF_2 electrodes until 2005 when Badway et al. reported >90% utilization of CuF_2 powder electrodes at theoretical voltages for the first time.[19] This was the first time nano-sized CuF_2 domains embedded in a matrix of metal oxide or sulfide mixed conductors. CuF_2 nano-domains improved the electronic transport difficulties, increased the current capability by allowing fast transport to the individual nano-grains. More recently in 2011, the electrochemical reaction of lithium and CuF_2 thin films fabricated by pulse laser deposition with a thickness of 100nm onto to stainless steel substrates was investigated by Z. W. Fu et al. for the first time.[20] Cycling showed a reversible capacity of 544mAh/g in the potential range of 1.0–4.0 V and the results confirmed an insertion process followed by a fully conversion reaction to Cu and LiF in the lithium electrochemical reaction of CuF_2 thin film electrode. It was noted that there was a reversible insertion reaction above 2.8V which could provide a capacity of about 125mAh/g, which is claimed CuF_2 is a potential cathode material for rechargeable lithium batteries.

In 2005, the electrochemical reaction of CoF_2 thin films with Li was investigated by Z. W. Fu et al. for the first time.[21] Thin films of cobalt fluoride were prepared in a fabricated by pulse laser deposition with a thickness of approximately 100nm onto to stainless steel substrates and a thin film coating of LiPON solid electrolyte was deposited on the surface of the CoF_2 as a separator between CoF_2 and liquid electrolyte to avoid a solution of CoF_2. It was discovered that if the cell consisted of the deposited CoF_2 thin film without LiPON, $LiPF_6$ as electrolyte and metal Li as the anode, the

charge/discharge curves of the cell were not achieved because CoF_2 would be dissolved in electrolyte and the voltage potential dropped to 0V during the initial discharge. The LiPON coated cells had a specific capacity during the first discharge of 595 mAh/g. The second discharge had a capacity of 252 mAh/g, indicating a large capacity loss of 58%. It was noted that the reversible conversion reaction of LiF with Co may involve in the decomposition and formation of CoF instead of CoF_2. Overall, the results demonstrated the formation of metallic cobalt and LiF after the initial discharge and the reversibility of CoF_2 with lithium.

In 2006, Makimura/ Tarascon et al. reported the electrochemical behavior of lithium and iron fluoride (FeF_2 and FeF_3) thin film electrodes fabricated by pulse laser deposition with a thickness of less than 150nm onto stainless steel substrates.[22] In addition, the influence of various deposition conditions such as the target FeF_2 or FeF_3 and the substrate temperature were considered. The cells had a large irreversible capacity loss on the first discharge but good cycling life was observed up to 30 cycles. However, the voltage capacity profiles obtained from the cycling from both of the iron fluoride thin films verse previously reported carbon metal fluoride nanocomposites were different.

Bismuth fluoride (BiF_3) was first investigated as a primary battery electrode material in 1978 in powder macro form.[23] Recently, Gmitter et al. 2012 for the first time utilized BiF_3 thin film electrodes deposited by thermal evaporation and of thicknesses of 1000 nm onto glassy carbon substrates in a study to investigate the impact of the electrolyte reactions on the surface and subsurface chemistry of the inorganic conversion material.[24]

In 2007, the electrochemical reaction of NiF_2 thin films with Li was investigated by Z. W. Fu et al. for the first time.[25] Previously, only Badway et al. reported the discharge and charge curves of NiF_2 prepared by high-energy milling.[26] Nano-sized 180nm thick NiF_2 thin films were prepared by pulse laser deposition (PLD) method onto stainless steel substrates. The discharge/charge behaviors of NiF_2 thin films were examined with the first discharge capacity of 650 mAh/g being more than the theoretical capacity 540 mAh/g and a 17% capacity loss on the second discharge. The NiF_2 thin films exhibited higher specific capacities and better cycle performance than the CoF_2 thin films. However, during the electrochemical conversion reaction mechanism with lithium upon cycling produced an intermediate product Li_2NiF_4 was identified in the counterpart process of NiF_2.

In 2010, the electrochemical reaction of lithium and MnF_2 thin films fabricated by pulse laser deposition with a thickness of approximately 100nm onto to stainless steel substrates was investigated by Z. W. Fu et al. for the first time.[27] During the first 50 cycles the material displayed a discharge capacity of 350 mAh/g to 530 mAh/g. The low polarization and high capacity of MnF_2 thin films showed that the material shows potential as a future rechargeable battery.

As a side notation, fluorides react with water forming HF, which causes difficulties in the preparation of fluoride materials. In addition, the fluoride ion and the hydroxyl anion are similar in size and there is potential substitution which occurs by a mechanism of isomorphic substitution and an accumulation of oxygen ions in the lattice of bulk fluoride samples leads to formation of the second phase (oxide or oxofluoride). However, the replacement of the fluorine atom by the oxygen atom is

thermodynamically unfavorable and fluorides are generally stable in dry air (oxygen) even on heating.[28] While working with metal fluorides, it is important to be aware of the hydrolysis sensitivity of the material to avoid sample contamination.

In 1937, Domange carried out extensive studies of the equilibrium constants of a wide variety of metal and alkaline fluorides at various temperatures.[29] His experiment utilized a platinum tube holding the fluoride, through which was passed a very specific regulated stream of water vapor and the composition of the vapor phase was established by analysis. The results concluded that the susceptibility to hydrolysis of some common metal fluorides was found to decrease in the following order: CuF_2, FeF_3, AgF, FeF_2, CrF_3, ZnF_2, NiF_2, CoF_2, CdF_2, PbF_2, MnF_2, MgF_2, CaF_2, and BaF_2.

1.1.5 Iron Fluoride (FeF_2) Thin Films

Prior to studying iron fluoride thin films for battery electrodes, there have been few reported applications of iron fluoride thin films in literature. The few previous literature studies involved investigating magnetic properties of iron fluoride using thin films.

In 1996, J. Nogues et al. studied iron fluoride thin films and discovered positive unidirectional exchange anisotropy in antiferromagnetic (FeF_2) and ferromagnetic (Fe) bilayers cooled through the antiferromagnetic critical temperature T_N in large magnetic fields.[30] The FeF_2 films were grown by sequential e-beam evaporation with a thickness of 90 nm and rate of 0.2 nm/s. The substrates consisting of MgO [100] were heated to 450°C for 15mins prior to deposition, then cooled to the FeF_2 growth temperature 200 <

T_S < 300°C. By following this procedure, the FeF_2 grows epitaxially along the [110] direction.

In 2001, Yamazaki et al. studied 2D magnetism in iron fluoride thin films to verify the results of theoretical studies on 2D spin systems and to identify novel properties intrinsic to lower dimensions.[31] FeF_2 films of nano scale thicknesses were deposited by electron beam evaporation at a deposition rate of 0.3˚A/sec on single-crystal substrate Al_2O_3 and MgO substrates held at a temperature of 300 < T_S < 400°C.

1.1.6 3D Nanostructured Electrodes

Traditional dense thin film battery electrodes with 2D geometries need a large footprint area to achieve large capacities. The mechanical integrity of the film decreases with thickness from the expansion and contraction during cycling so producing thicker electrodes to store more energy is not a feasible approach. In addition, when the thickness is increased in dense 2D electrodes the interfacial surface area remains constant this reduces the power density of the battery. In terms of increasing the rate capacity (power), the conventional approach with dense electrodes has been to reduce the particle size to a few nanometers. Due to the limiting accessible interfacial area which limits the opportunity to improve performance, 2D battery designs tend to be inefficient as they compromise between energy density and power density.

Discovering new approaches to improve battery performance has led to 3D nanostructured materials with porous morphologies. Nanostructured materials as battery electrodes are of increasing interest to develop lithium batteries with higher energy density, higher rate capability, and improved cycling stability. Nanostructures are beneficial as a result of their large interfacial surface area, short distance for mass and

charge transport and mechanical stress absorption from charge/discharge volume changes. For cathode materials with high band gaps, nanostructures have the potential to improve the problem of low electronic conductivity. Obtaining high power in any electrode can be achieved with porosity which ensures a ready supply of ions from the electrolyte. However, porosity can sacrifice volumetric capacity at the price of high rate capacity. This can be avoided if the optimum pore size is selected such that volume of the solid will be optimized.

Despite, the many benefits of nanostructures there are some potential challenges. The greater interfacial areas render the potential to increase solubility of electrode material in the electrolyte solution and increase unwanted side reactions that occur on electrode surface. In addition, the more open and exposed the area of the electrode the greater the chances of collecting impurities and contaminants within the material.

These structures are relatively new to battery electrodes and were initiated through studies by Nishizawa et al 1997 where it was demonstrated that nanotube morphologies formed in the pores of porous alumina templates improved the capacity retention and rate capabilities of $LiMn_2O_4$ during cycling.[32] Then in 2000, the same group consisting of Martin and coworkers completed more studies on nanostructured $LiMn_2O_4$ cathodes and tin oxide anodes.[33,34] This initial use of nanostructured battery electrodes, inspired a vast amount of studies using template synthesis as a means of producing nanotubes, nanowires, and nanorods for positive electrode and negative battery electrode materials.[35,36,37,38,39] Currently, there is focus on more commercial processes to form nanostructures such as thin film vacuum deposition and laser

etching.[40,41,42,43] Table 2 below is a list of some of the highly cited papers which have advanced nanostructures in battery electrodes.[44] This thesis will focus on physical vapor ebeam deposition as the method for creating nanostructures and will be the first study to apply these morphologies to conversion cathode electrodes.

Table II. Advances reported on the synthesis of 3D electrodes and 3D batteries.

Group	Chemistry	Cell type	Energy density ($mAh\,cm^{-2}$)	Power density ($mW\,cm^{-2}$)	Gravimetric capacity ($mAh\,g^{-1}$)	Comments
Nishizawa et al.[21]	$LiMn_2O_4$	Positive electrode	0.103	—	134	3D tubular arrays; current density = 0.1–1 $mA\,cm^{-2}$
Wu et al.[22]	MnO_2	Negative electrode	0.233	—	970	Electrochemical deposition; specific current = 85 mAg^{-1}
Cui et al.[23]	Carbon–Si core–shell nanowire	Negative electrode	4.0	—	2000	High surface area nanowires in 2D electrode arrangement; cycled at C/5 rate
Li et al.[24]	SnO_2	Negative electrode	0.037	—	720	Templated nanowire array; current density = 0.32 $mAcm^{-2}$ (8C)
Kotobuki et al.[17]	$LiCoO_2 - Li_4Mn_5O_{12}$	Full battery	0.0073	—	<1	Honeycomb $Li_{0.35}La_{0.55}TiO_3$ used as template and ceramic electrolyte
Teixidor et al.[25]	Carbon	Negative electrode	0.350	—	—	Mixture of pyrolized SU-8* and MCMB* in post array
Cheah et al.[26]	TiO_2	Negative electrode	0.0112	—	168	Electrodeposited TiO_2 on Al nanorods; current density = 1 μAcm^{-2}
Shaijumon et al.[27]	$LiCoO_2$	Positive electrode	0.110	—	—	Electrodeposited on Al nanorods; cycled at C/5 rate
Nathan et al.[12]	MCMB-MoO_yS_z	Full battery	1.0–2.0	0.35–1.75	—	Deposition of films in silicon or glass microchannel plate using centrifuge technique; current density = 0.2–1.0 $mAcm^{-2}$
Min et al.[28]	Carbon–PPYDBS*	Full battery	0.0106	0.06	—	Interdigitated design using pyrolyzed SU-8 electrodeposited with doped polypyrrole; current density = 0.02–0.09 $mAcm^{-2}$
Chamran et al.[29]	Zinc–Air	Full battery	8.93	32.5	626	2D commercial cathode used; current density = 0.42– 28.25 $mAcm^{-2}$

Table 3: Highly cited papers which advanced 3D nanostructured electrodes[44]

2 Electrochemical Impedance Spectroscopy (EIS)

2.1 Theory

2.1.1 Double Layer Capacitance

Electrochemical impedance spectroscopy is capable of predicting the electrochemical accessibility surface by measuring the double layer capacitance of the electrode. Double layer capacitance was discovered by Helmholtz in 1879, Gouy in 1910, Chapman in 1913 and Stern in 1924 when they observed that ionic charges from the electrolyte can be separated and forms a double layer across the surface of a conductor (electrode). The double layer is established at the electrochemical interface between the electrolyte and electrode where the charge transfer interfacial reaction occurs as shown in Fig. 2.1.[56] The capacitance of the double layer is proportional to the electrochemical accessibility surface area of the electrode and inversely proportional to the thickness of the double layer.

The double capacitance initially introduced by Helmholtz and then refined later by Stern and Geary can be described according to $C=\varepsilon A/d$, where ε is the electrolyte dielectric constant, A the surface area accessible to ions, and d the distance between the A and center of the ion.

It is known that the surface area generally increases by the development of porosity. However, O. Barbieri et al 2005 showed there is no simple linear relationship between the surface area and the capacitance.[45] It has been shown in several studies using carbons that the specific capacitance has a linear dependence on surface area for lower specific surface area, but as the surface area increases the relationship rapidly

plateaus.[46,47] It has been shown that amount of surface area alone doesn't alone impact specific capacitance but the way in which the porosity is developed such as the control of the pore size as well as pore size distribution plays a role.[48,49,50]

Electrochemical impedance spectroscopy can be used for relative comparisons between samples of identical composition with the interface double layer capacitance result being proportional to the accessible surface area. In a recent porous electrode study, Yan Yu et al 2009, a three-dimensional (3D) porous amorphous SnO_2 thin films were deposited on Ni foam substrates by Electrostatic Spray Deposition (ESD) technique as anodes for Li-ion batteries.[51] This study shows how electrochemical impedance spectroscopy can be used to compare the electrochemical accessibility surface area of electrodes and relate that information back to cycling performance. Additional studies have been conducted which utilized EIS to predict relative porosity between electrode samples.[52,53,54,55]

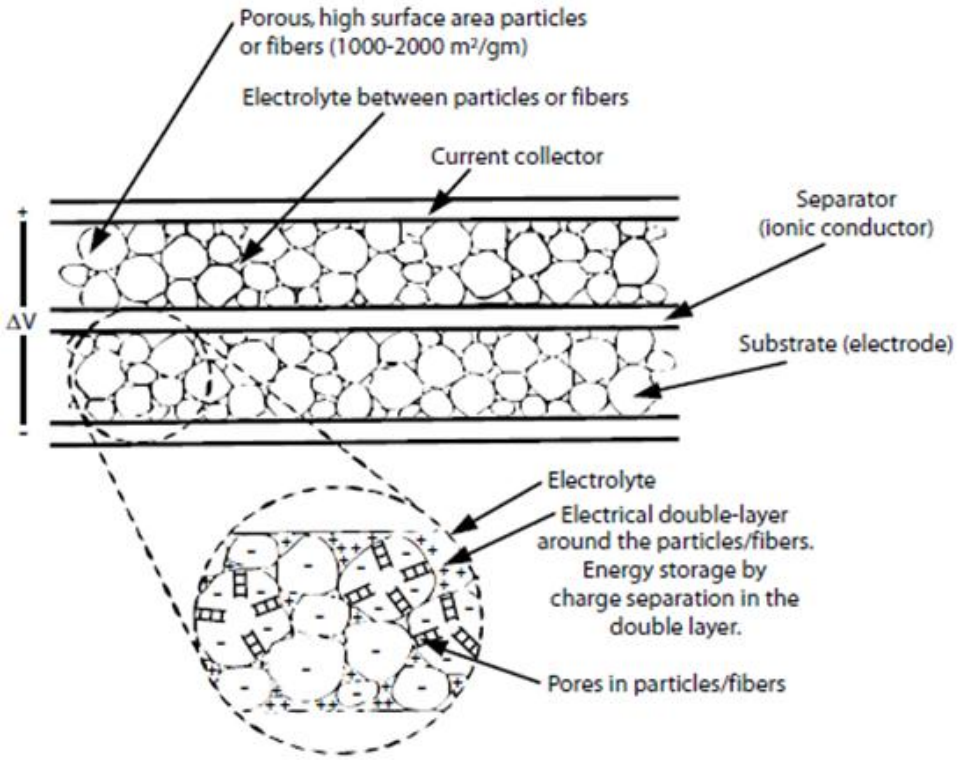

Figure 2.1: Ions from solution forming a double layer capacitance within a porous electrode[56]

2.1.2 Randles Impedance Nyquist Plot and AC Impedance Equivalent Circuit

The Randles circuit shown in Fig. 2.2 is used to calculate the double layer capacitance of an electrolyte-electrode interface using electrochemical impedance spectroscopy.[57] The equivalent circuit is comprised of the solution (electrolyte) resistance Rs, the charge transfer resistance Rct, the double layer capacitance Cdl and the Warburg impedance W. The plot in Fig. 2.2 is called a Nyquist plot which represents the impedance as a function of frequency. From the Nyquist plot, the double layer capacitance can be calculated from the frequency at the maximum of the semicircle ($\omega=2\pi f=1/Rct*Cdl$). The product of Rct and Cdl is often termed the time constant τ of

the electrochemical process. The 45° line indicating Warburg-limited behavior can be extrapolated to the real axis. The intercept is equal to Rs + Rct – 2σCdl, from which σ and diffusion coefficients can be calculated. The solution resistance, Rs, depends on the ionic concentration, type of ions, temperature, and the geometry of the area in which current is carried. The double-layer capacitance, Cdl, results from charge being stored in the double layer at the electrolyte-electrode interface. The charge transfer resistance Rct refers to current flow produced by redox reactions at the interface, and the Warburg impedance results from the impedance of the current due to diffusion between the electrolyte-electrode interface.

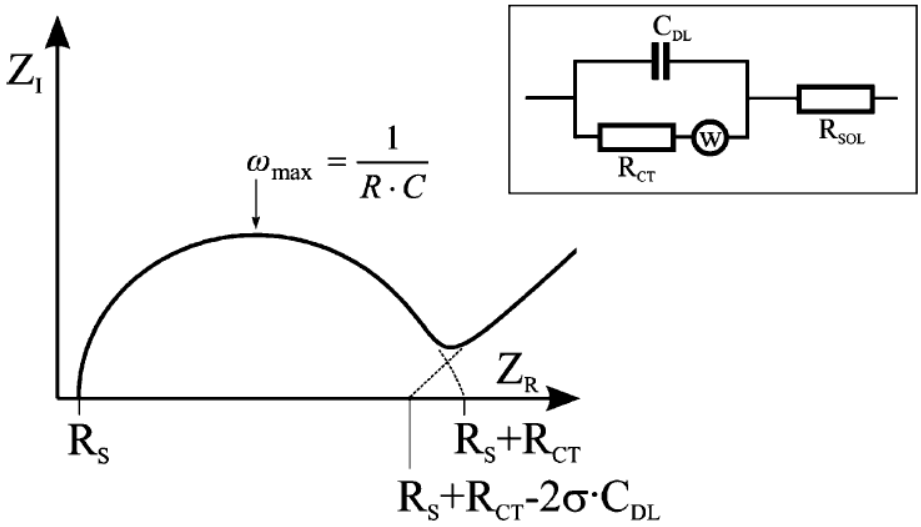

Figure 2.2: Randles impedance Nyquist plot and equivalent AC circuit[57]

The trend of a typical Nyquist plot for the Randles circuit can be explained. When the oscillation frequency decreases, a very thin film of charge (double layer) starts to grow on the electrode-electrolyte interface with time. With the formation of this film the charge transfer resistance increases with a decrease of frequency. This eventually

increases impedance. In the low frequency region (to the right of the plot), the accessible surface area becomes significant because large surface area allows more charge to pass by and thus reduces impedance.

As an example to better understand the trend of the Nyquist plot as it relates to the electrochemical accessibility surface area of a porous structure, simple models are defined. In Fig, 2.3 a Nyquist plot showing the dependence of impedance with frequency has been examined for various geometries of a single pore.[58] This comparison plot shows that the more sealed and less accessible the shape of a pore the more the impedance exhibits a pseudo transfer resistance which is represented by a semi-circle at high frequencies (to the left of the plot). Conversely, the more accessible the shape of a pore the more linear the impedance curve.

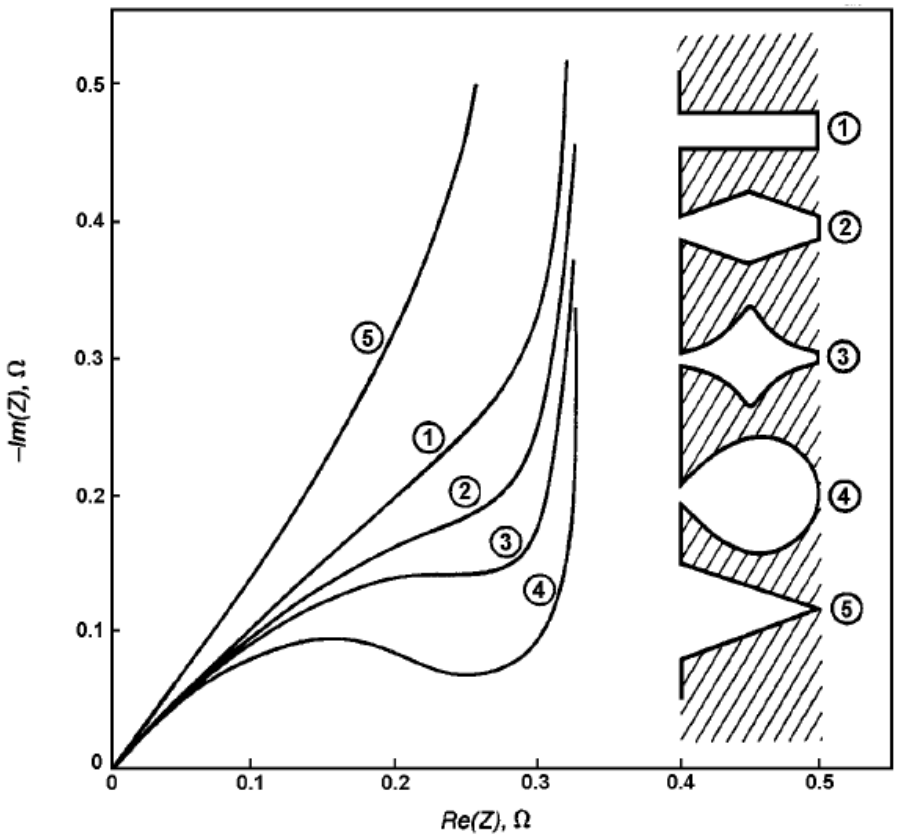

Figure 2.3: Impedance plots for various shapes of pores[58]

2.1.3 Constant Phase Element (CPE)

Despite the classical circuit definitions previously discussed, the impedance results for an electrode/electrolyte interface often reveal a frequency dispersion that cannot be described by simple circuit elements such as resistances, capacitances, inductances or convective diffusion (Warburg) impedance. The frequency dispersion is generally attributed to a capacitance dispersion expressed instead in terms of a constant phase element (CPE).[59] Therefore, constant phase elements (CPE) are used extensively in equivalent electrical circuits for fitting of experimental impedance data. In addition to be associated with electrode porosity, the CPE behavior is influenced by distributed

surface reactivity, surface inhomogeneity, roughness or fractal geometry and to current and voltage distributions associated with electrode geometry. The CPE consists of a transmission line and an impedance given by $Z = [Q (jw)^{\alpha}]^{-1}$, where $j=\sqrt{-1}$, Q is a constant combining the resistance and capacitance properties of the electrode, and α takes values between 0 and 1. However, this is only one definition for CPE and in the literature different equations are proposed and depending on the formula used, the CPE parameter is Q, 1/Q, or Qα and for capacitive dispersions the CPE exponent is α or (1 − α) with α close to 1 or close to zero. As a flexible fitting parameter, the CPE has been considered to represent a circuit parameter with limiting behavior as a capacitor for α = 1, a resistor for α = 0, and an inductor for α = −1. However, despite the fact that CPE is an extremely flexible fitting parameter, the different expressions given for the CPE underline that the physical meaning is still not clearly understood. Equivalent circuits for CPE are defined in Fig. 2.4 with a.) representing a non-porous flat electrode and b.) representing a porous electrode. R1: resistance composed of solution resistance (Rs) and electrode resistance (Re), R2: charge-transfer resistance across electrode/ solution interface, CPE1: constant-phase element representing interfacial capacitance, CPE2: pseudo capacitance of surface functional groups.[60]

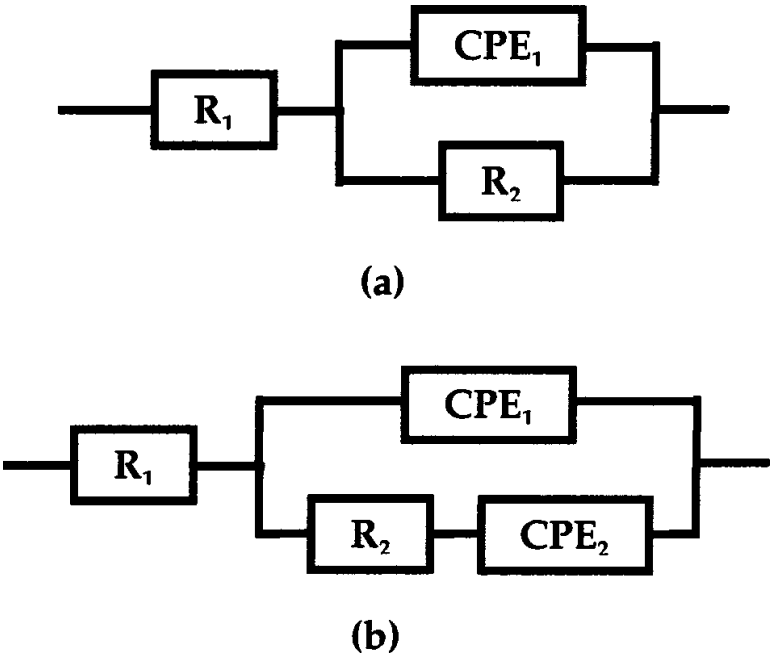

Figure 2.4: CPE equivalent circuits, a) non-porous and b) porous electrodes[60]

Electrochemical impedance spectroscopy can be utilized as a rarely used but alternative quantitative measurement approach for determining the accessible surface area. In electrochemical impedance spectroscopy, an AC voltage potential is applied to the electrochemical cell. Then a small sinusoidal excitation signal is applied to the potential producing an AC current signal which is recorded as a function of frequency. The regression of the measured impedance as a function of frequency provides insight about the electrochemical capacity of the electrolyte-electrode interface. [45,46,47]

To determine the surface impedance of porous electrodes two different wall surface conditions can be considered. For the first condition, smooth pore walls which have single length scale pores represented by the corresponding Nyquist plot shown in Fig. 2.5.[61] For the second condition, the electrode has two different length scales of

pores such as that a single large length scale pore containing many small scale pores on the pore's surface as shown in Fig. 2.6.[61]

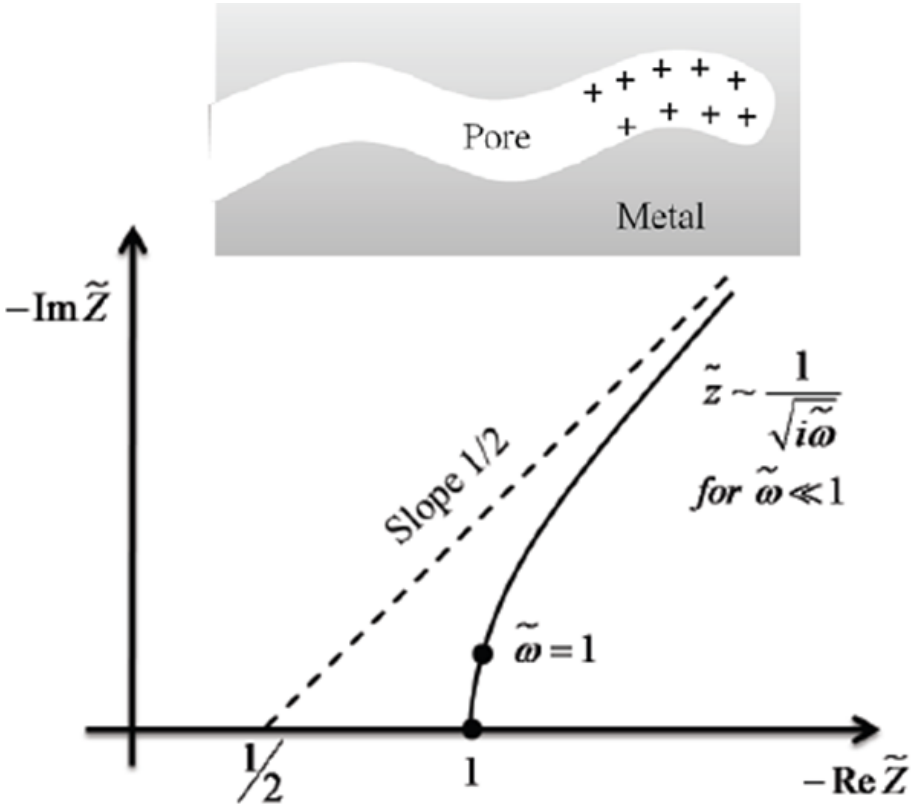

Figure 2.5: Schematic of a pore with smooth walls and its represented Nyquist plot[61]

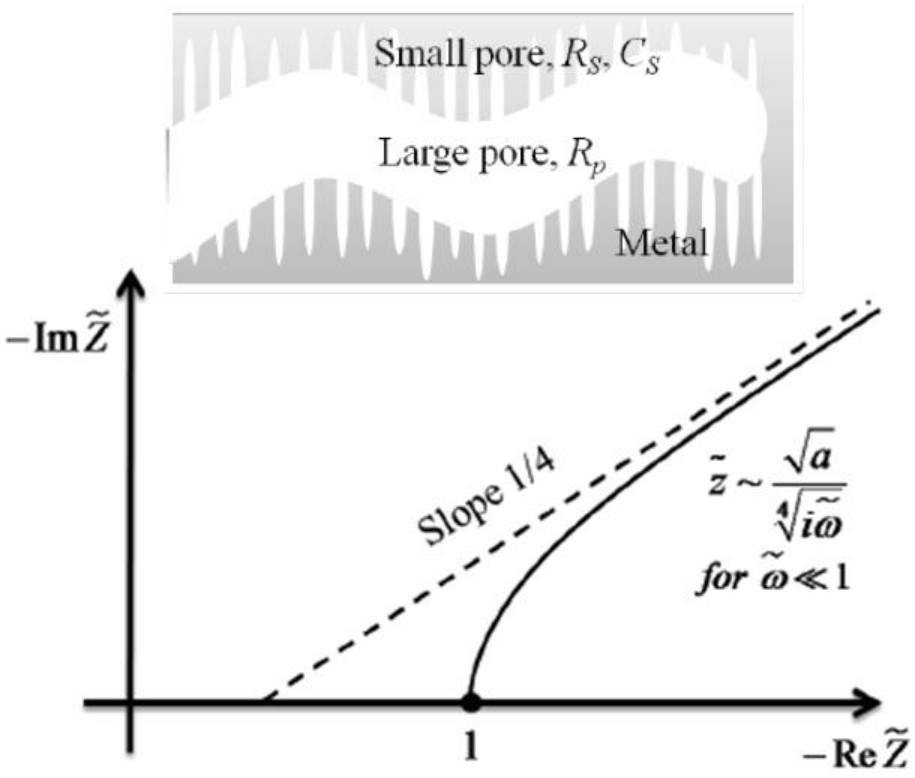

Figure 2.6: Schematic of a pore which has porous walls and its represented Nyquist plot[61]

2.2 Practical Applications of EIS

2.2.1 Charge Transfer Impedance and Diffusion

Considering two ideal conducting flat electrode cells for which faradaic reactions occur quickly and the charge transfer resistance negligible, then the bulk capacitance and bulk resistance is only considered. For this case, the equivalent RC circuit of the flat electrode cell can be expressed where Cb is the bulk capacitance per area and Rb is the bulk resistance per area. The equivalent RC circuit is shown in Fig. 2.7 along with the Nyquist plot of ideally conducting electrodes or ideally non-polarizable cell.[61] For this

case, the linear transformation of the dimensionless impedance should trace out a semicircle.

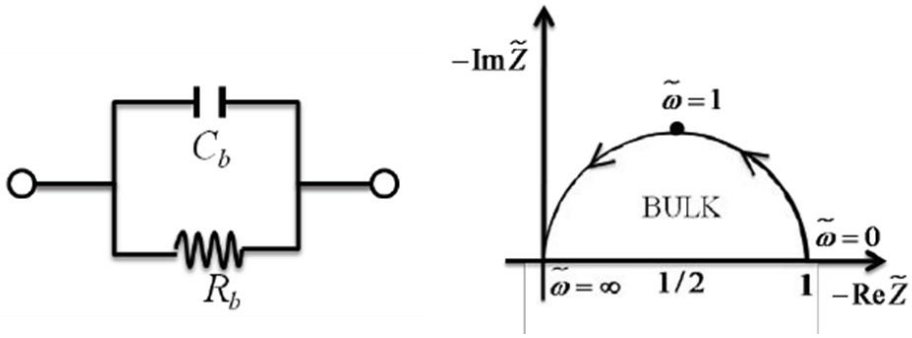

Figure 2.7: Ideal conducting electrodes equivalent RC circuit and Nyquist plot[61]

When considering two ideally blocking flat electrode cells that don't have faradaic reactions the current leads to capacitive charging of the double layers. The cell has ideally polarized electrodes and the RC circuit is determined by the double layer capacitance as shown in Fig. 2.8.[61] C_D is the double layer capacitance per area and can be obtained by $C_D=\varepsilon/\lambda_D$. The Nyquist plot represented with a vertical linear trend at the impedance of 1 shows ideally blocking electrode behavior.

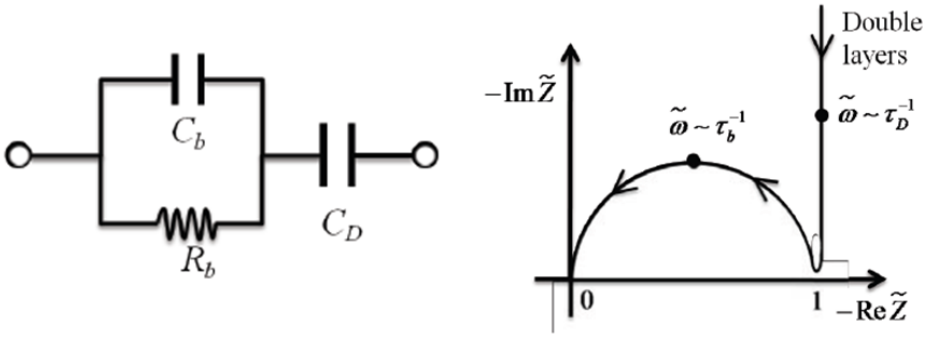

Figure 2.8: Ideal polarizable electrodes equivalent RC circuit and Nyquist plot[61]

When considering two partially polarizable electrodes flat electrode cells which have not-fast faradaic reactions then the electrodes have partially polarizable electrodes. The faradaic charge-transfer resistance, R_F, and double layer capacitance, C_D, is considered simultaneously and the RC circuit can be expressed as shown in Fig. 2.9.[61]

For partial polarized electrodes, depending on the speed of faradaic reactions there are different forms of Nyquist plots represented with the same RC circuit. Fig. 2.9 (a) shows a typical Nyquist for partially polarized electrodes. When faradaic reaction speeds are fast, the charge transfer resistance decreases, and it can be considered as blocking electrodes which is shown in Fig. 2.9 (b). Eventually if the charge transfer resistance can decrease to the point that $R_F \rightarrow 0$ the Nyquist plot become the same to that of ideally conducting electrodes previously shown in Fig. 2.7. In contrast, Fig. 2.9 (c) shows the case of slow faradaic reactions and higher charge transfer resistance. Eventually if the charge transfer resistance increases to the point that RF $\rightarrow \infty$ the Nyquist plot become the same to that of ideally blocking electrodes previously shown in Fig. 2.8.

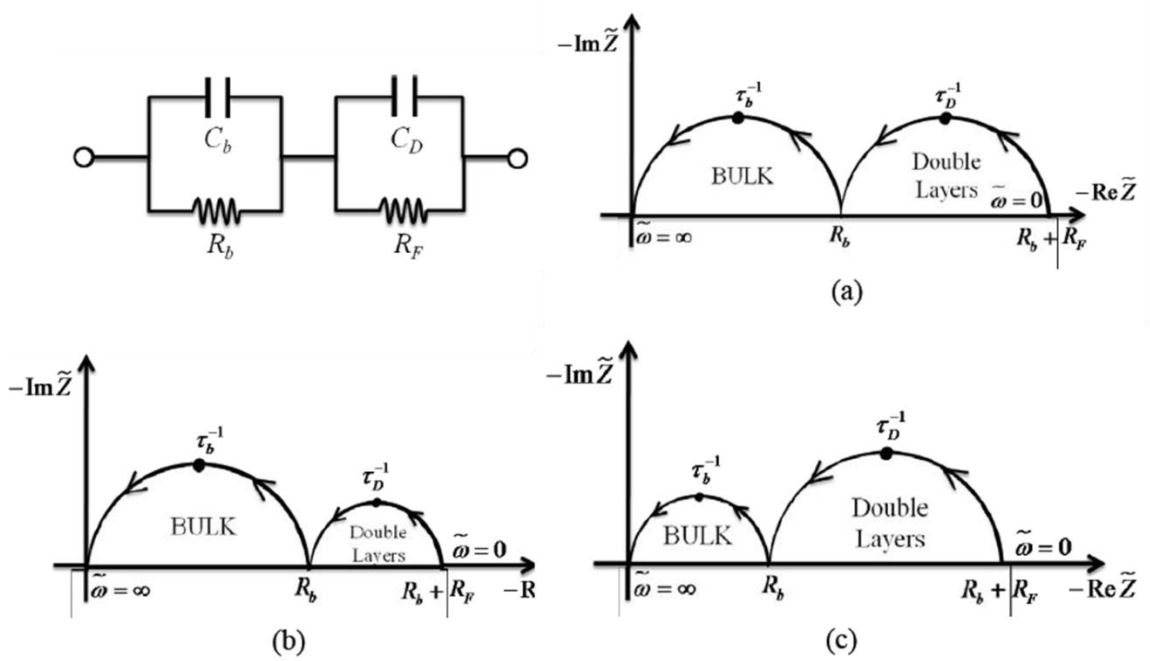

Figure 2.9: Nyquist plots of cells (a) balanced bulk and faradaic resistances, (b) more highly conducting electrodes with relatively large bulk resistance, and (c) nearly blocking electrodes with relatively small bulk resistance[61]

2.2.2 Electrolyte Accessible Surface Area

Rate performance of a battery improves when there is a large contact surface area between the electrode and the electrolyte. The contact surface area increases as the electrode becomes more porous to the onset of micro porosity at 2nm at which electrolyte molecules cannot easily enter. With increasing electrolyte accessible porosity and this surface area of the electrode, the kinetics of mass transfer of Li ion is increased.[56,62]

Typically the bulk mass transfer becomes more difficult as discharge continues from the result of the cathode volume expansion during discharge and temporary or permanent depletion of the vacancies near the surface of the primary particle depending

on the reaction mechanism. During the cathode volume expansion, the pores with fine openings are easily sealed. As a result, mass transfer in and out of these pores becomes more difficult. Designing an electrode that maintains large internal surface area and allows for fast mass transfer to access this area is the key one of the keys to achieving high rate capability.

Due to the aforementioned steric limitations, electrochemically accessible surface area is normally smaller than the common BET measurement method of surface area. Therefore, in designing an electrode for increased internal surface area it is important to note that the porosity of the electrode is inversely related to the size of the particles which comprise the electrode. For example, if the electrodes are produced from powder the primary particles sinter together due to surface forces to form secondary particles. Pores are formed in between the sintered secondary particles. The pore size depends on the size and shape of primary particles and the conditions in which they are packed. Pores with different sizes have different time constants and cannot be accessed at the same time. By definition, there are three types of pores Macro (>50nm), Meso (2<size<50nm) and Micro (<2nm) shown in Fig. 2.10.[56] In addition, not all the pores can be accessed electrochemically due to steric limitations relative to the size of the electrolyte species.

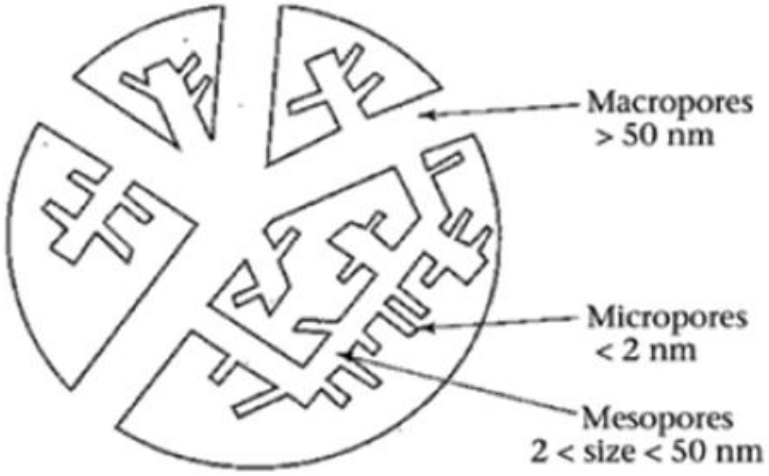

Figure 2.10: Definition of pore type showing macro, meso and micro pores[56]

3 Physical Vapor Deposition (PVD) Thin Films

3.1 Introduction

Vacuum and thin film technology has an interesting history. The technology arguably started with the invention of the first piston type vacuum pump in 1640 by Otto van Guericke which was used to pump water out of mines. Vacuum science started to evolve thereafter with various vacuum and pressure devices being invented. By 1800, the invention of the voltaic battery by A. Volta led to the rapid development of vacuum science involving electrical arcs. Faraday is credited for producing the first thin film deposition in 1857 in which he used a Lyden battery to produce an arc which vaporized a material for an optical property study. Ever since, vacuum and thin film technology has continued to rapidly evolve and contribute greatly to society.

In the more recent past, thin film vacuum deposition has increasingly changed everyday life with the influence it has in a large number of applications. Thin film vacuum deposition applications are broad and include, but are not limited to; wear

resistance in medical orthopedic implants, reflection of IR light in low emissivity architectural windows, flexible semiconductors for solar cell roof tiles, decorative corrosion resistant coatings for plumbing fixtures and integrated circuits for computers and electronic devices.

Thin film vacuum deposition starts with the selection of vacuum pressure that meets the requirements of the specific process. The level of vacuum pressure selected will depend on the materials being deposited and process equipment being utilized. Overall, the use of vacuum and clean practices when depositing films minimizes impurities to tolerable levels. The tolerable level of impurities depends on the material being deposited and the chemical reactivity it has to the impurities. In addition, a suitable vacuum level for the technology of equipment utilized needs to be considered. There is a vast selection of vacuum pumps, pressure monitoring gauges and material vaporization equipment in which to choose from. However, regardless of the equipment selected, the overall transport of the vaporized material and growth of the thin film is fundamentally the same.

3.2 Vacuum Pumps

Thin film vacuum deposition starts with the selection of vacuum pressure that meets the requirements of the specific process. The level of vacuum pressure selected will depend on the materials being deposited and process equipment being utilized. Overall, the use of vacuum and clean practices when depositing films minimizes impurities to tolerable levels. The tolerable level of impurities depends on the material being deposited and the chemical reactivity it has to the impurities. In addition, a suitable vacuum level for the technology of equipment utilized needs to be considered.

There is a vast selection of vacuum pumps, pressure monitoring gauges and material vaporization equipment in which to choose from. However, regardless of the equipment selected, the overall transport of the vaporized material and growth of the thin film is fundamentally the same.[63,64,65]

The vacuum is produced by a pump that collects gas and vapor molecules by giving them a direction of flow and preventing them from reentering the chamber. In thin film vacuum deposition there are mechanical, momentum transfer and capture pumps. Each pump type has a specific pressure operating range and its own disadvantages and advantages. The mechanical pump, such as the rotary vane, functions by capturing, compressing and then expelling the chamber molecules. Mechanical pumps typically have a base pressure of 10^{-4}Torr and are used initially in the process to rapidly reduce large volumes of gas. Momentum transfer pumps, such as the diffusion and turbo, functions by giving the molecules a preferred direction of flow. Momentum transfer pumps have an operating pressure range of 10^{-2} to 10^{-8}Torr and require a mechanical pump for initial pump down. Capture pumps, such as the cryogenic pump shown in Fig. 3.1, functions by collecting gas molecules.[66] In particular, the cryogenic or cryopump condenses gases on cold surfaces by running compressed helium at temperature of 10 Kelvin (K) through the pump to create a vacuum. The cryopump consists of three pumps in one by having three stages/arrays at progressively cooler surfaces. The inlet array of the pump operates at 60 to 100 K to condense water vapor and heavy hydrocarbons on metal surfaces. Behind the inlet array, a condensing array operates at 10 to 20 K to solidify argon, nitrogen, oxygen and most other gases. The temperatures of these arrays nearly all gases form dense solids with low vapor

pressures. However, hydrogen, neon and helium do not form solids at these temperatures and are held by adsorption into activated carbon which is shielded by the 10K condensing array. Cryopumps perform optimally at pressure range of 10^{-3} to 10^{-8} Torr. They require a mechanical pump for initial pump down of the chamber and cryopump maintenance.[66]

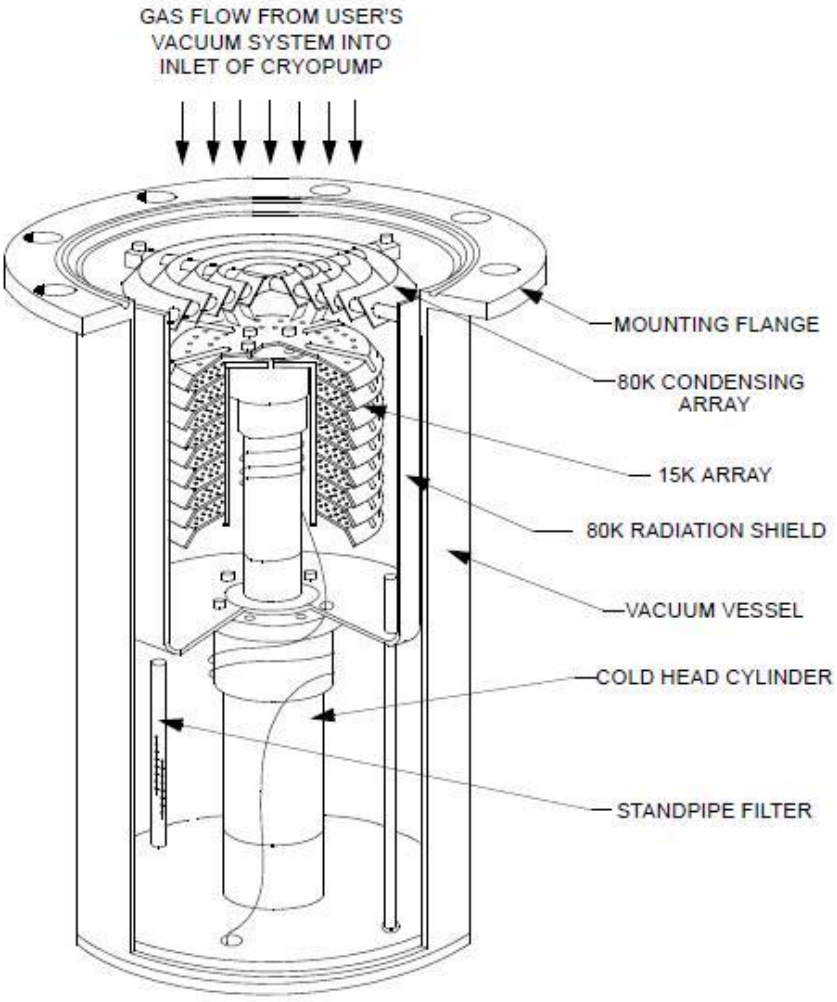

Figure 3.1: Cutaway view of a typical Cryo-Torr pump[66]

3.3 Vacuum Measurement

The level of vacuum pressure can be monitored by several methods.[63,64] There are pressure gauges such as the capacitance diaphragm (Baratron) which monitor directly from the force per area. There are indirect gauges such as the Pirani (Convectron) which calculates the pressure from the thermal conductivity of the gas. There is the indirect Bayard-Alpert (Ion Gauge) which ionizes and collects the gas molecules to determine the pressure. Gauge types vary in pressure range measurement capability. The type of gauge used is determined by the pressure level requirements and often multiple gauge types are used in combination to effectively measure varying pressure levels throughout the process. Fig. 3.2 shows the effective pressure monitoring ranges of various gauges.[63]

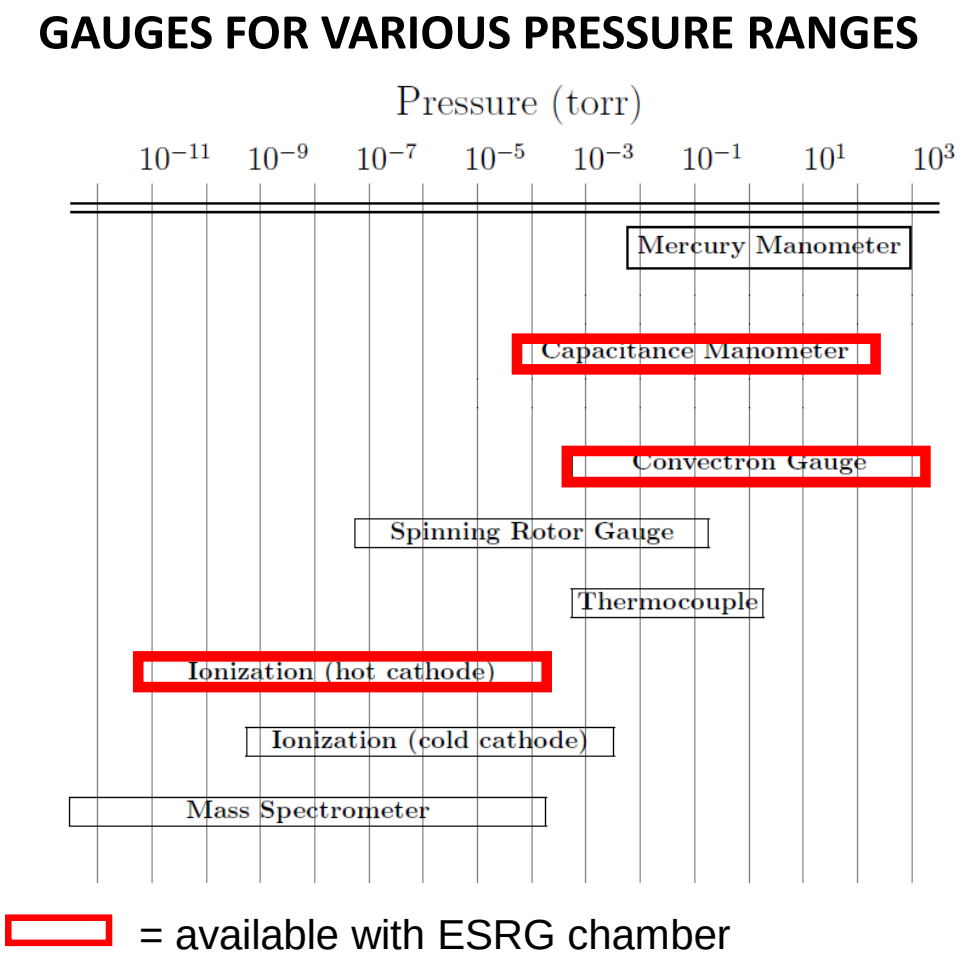

Figure 3.2: Effective pressure monitoring ranges of various vacuum gauges[63]

3.4 Physical Vapor Deposition Processing

In thin film physical vacuum deposition (PVD) a material referred to as the source is evaporated onto a substrate within a vacuum chamber by means of resistance heating or an energy beam of electrons, photons or positive ions. There are three typical steps in a physical vacuum deposition (PVD) process. The first step is vaporizing the source material, second is transport of the evaporated source material to the

substrate and third is condensation of the evaporated source material onto the substrate to form a thin film.

3.4.1 Source Vaporization Techniques

During the first step of PVD the source material is evaporated by means of resistance heating or an energy beam of photons, positive ions or electrons.[65] In resistance heated evaporation the source is held by device made from resistive heater material. The resistive heater holding device can be in the form of a wire, crucible, boat or basket and are made most commonly of tungsten, molybdenum and tantalum. A high current (several hundred amperes) with low voltage (less than 10 volts) is passed through the holding device which resistively heats the source to evaporation. Resistance heating is relatively simple and inexpensive but is limited to source materials with a melting temperature of less than 1500 °C.[64,65]

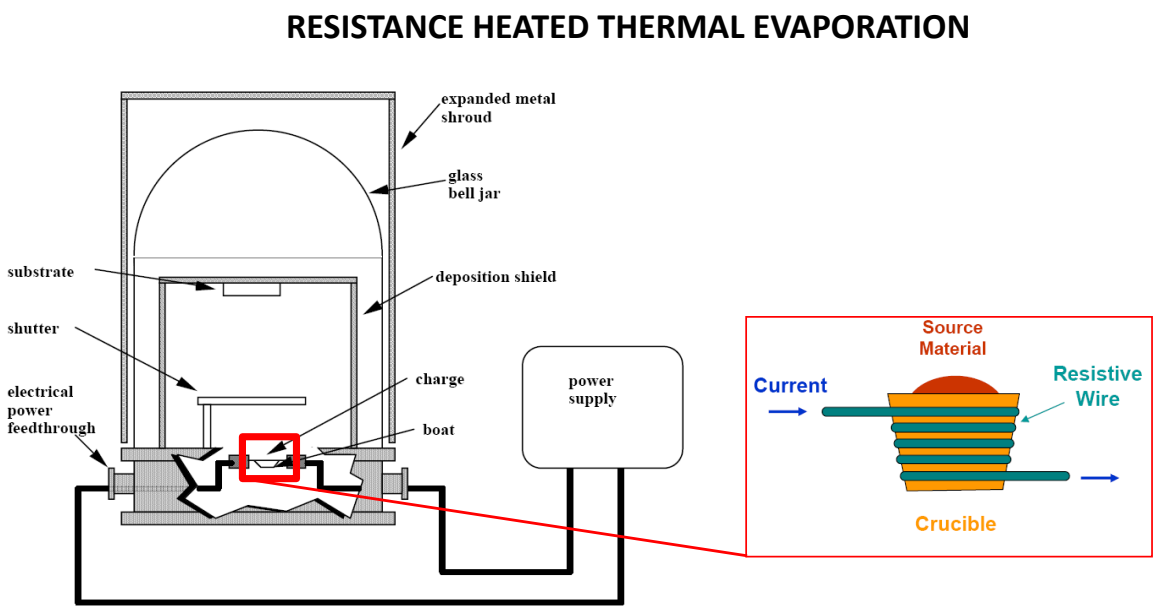

Figure 3.3: Typical resistance heated thermal evaporation system[67,68]

Utilizing an energy beam of photons to evaporate the source is called pulse laser deposition. The ultraviolet (UV) laser beam enters a vacuum chamber through a quartz window and directed at the source. The laser can operate within a greater pressure vacuum relative to other deposition processes and requires pressures only slightly less than 10^{2}Torr. The pulse control of the laser allows for fast switching which can be utilized to synchronize the evaporation of multiple sources. One disadvantage with pulse laser is the macro particle ejection of source material due to thermal shock. Depending on the optical absorption depth and thermal expansion coefficient of the source, surface heating can occur and create compressive stress stock waves which eject macro particles.[64,65]

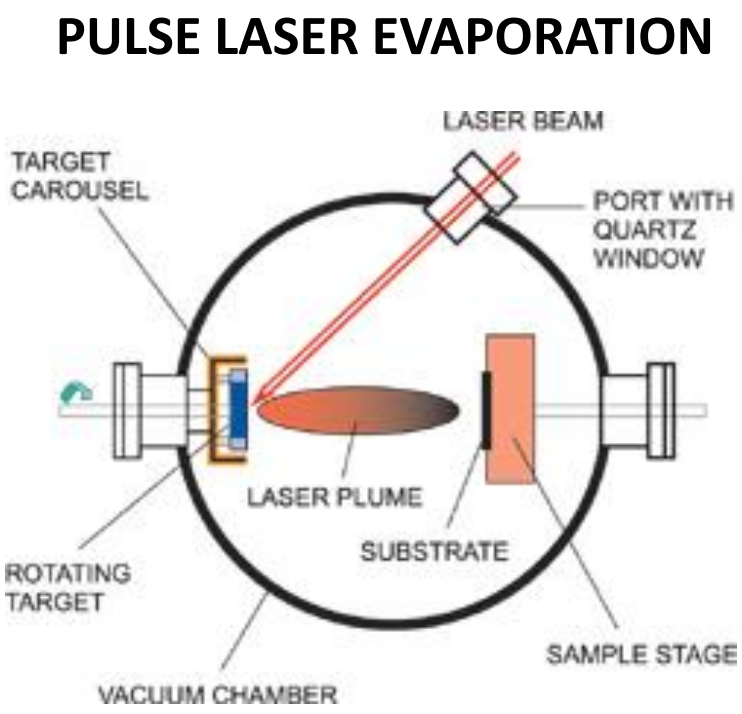

Figure 3.4: Typical pulse laser evaporation system[69]

Utilizing an energy beam of positive ions to evaporate the source is called sputter deposition. Contrary to the thermal evaporation processes mentioned previously, sputtering is a physical evaporation process which bombards the source with ions of a gas, typically argon, which are accelerated through an electric field. There are multiple variations of sputtering that are based on two concepts glow discharge or ion beam. In glow discharge a voltage bias is applied between the source attached to an anode and the substrate attached to a cathode. A gas, typically of argon, is placed between the electrodes. The applied negative bias creates an acceleration of particles; electrons from the source anode accelerate towards the substrate cathode creating plasma of positive argon ions which then bombard the source. From the bombardment, the source material is ejected and deposits on the substrate. Ion beam is similar in concept to the glow discharge however the plasma is generated and ions are accelerated from a self-contained ion gun. Sputter deposition has the advantage of being able to deposit any material. However, one disadvantage of sputtering is that the films tend to be non-uniform and it is expensive relative to other PVD processes.[64,65]

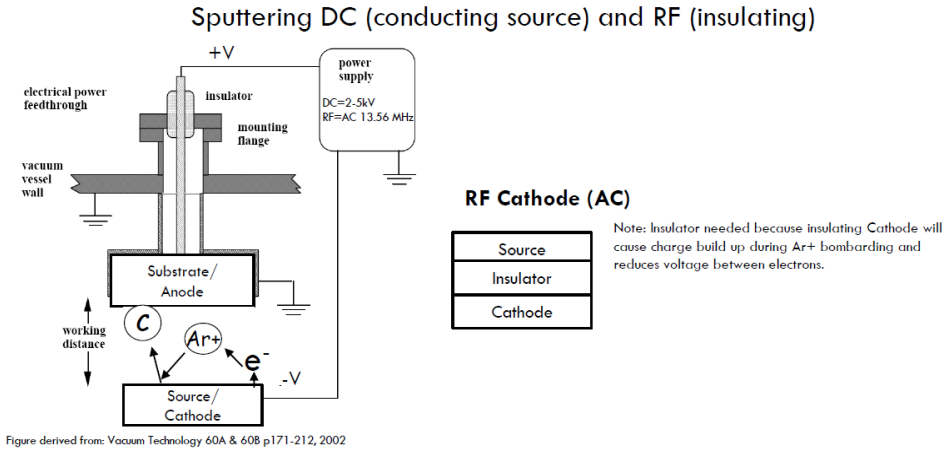

Figure 3.5: Typical glow discharge sputtering evaporation system[67]

Utilizing an energy beam of electrons to evaporate the source is called electron beam deposition. Electron beam deposition uses a gun which consists of a water cooled crucible to hold the source material, a filament to generate the electrons and internal magnets which direct the electrons to the source. To generate the electrons, low current (10-150 mill amperes) with high voltage (5-20 kilovolts) is passed through the filament. The electrons can be controlled through the magnets to raster in selected patterns over the surface of the source and allow for large areas to be heated uniformly. Electron gun may contain multiple crucibles so that more than one material can be deposited in chronological order to create layered thin films. Electron beam evaporation is considered the most versatile means of PVD. Electron beam evaporation offers several advantages over other processes which include; precise control of deposition rates, excellent material utilization, sequential deposition capability and cooler substrate temperatures.[64,65]

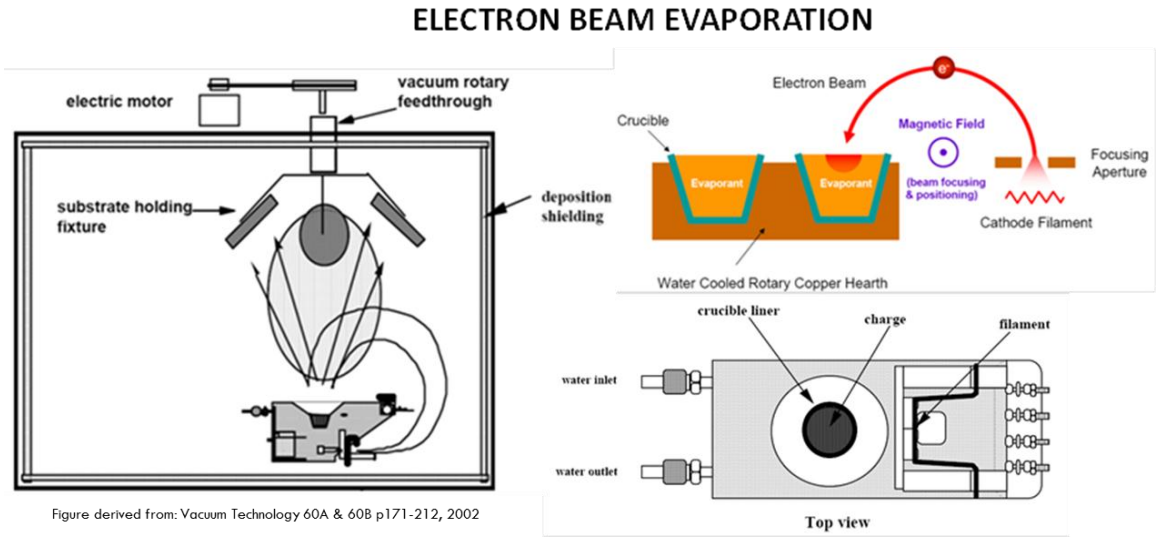

Figure 3.6: Typical electron beam evaporation system[67]

3.4.2 Vapor Flux Transport

Transport of the source vapor to the substrate is the second step of the PVD process. The vacuum environment reduces residual gas molecules and allows the vapor to be transported in a linear path to the substrate. The measure of the average distance between the residual gas molecules and the source vapor is called the mean free path. The mean free path is proportional to temperature and pressure T/P. In a typical vacuum chamber at 25°C and 10^{-6}Torr the mean free path is approximately five meters.[63,64,65]

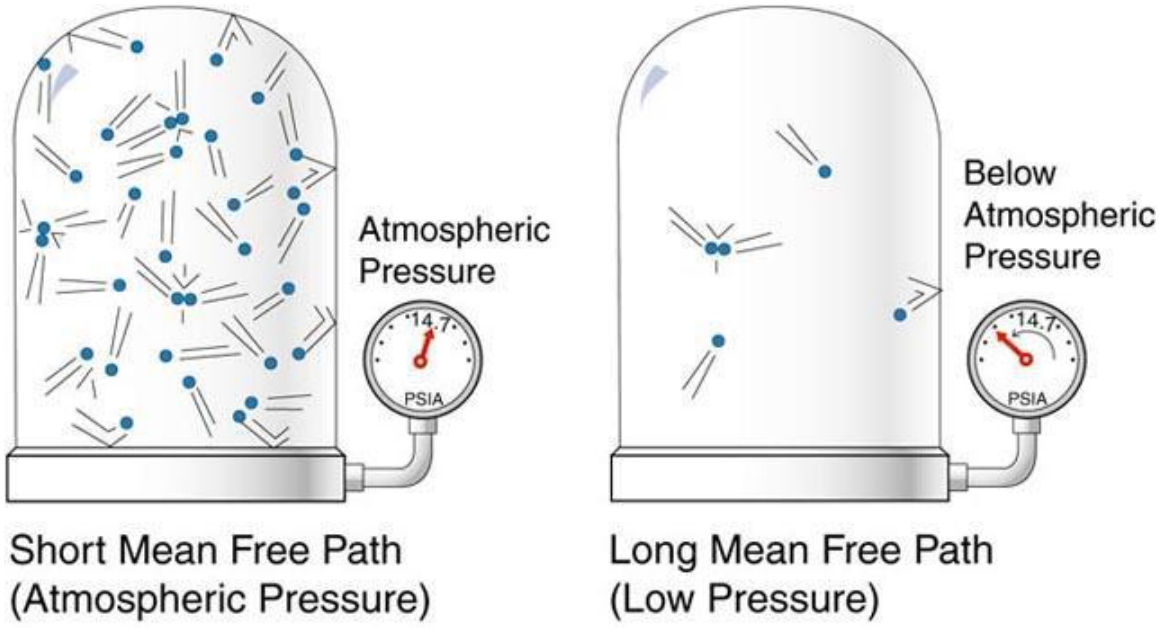

Figure 3.7: Comparison of short verse long mean free[70]

In general, the vapor molecules travel to the substrate at a mean velocity that is proportional to temperature in Kelvin and molecular weight $(T/M)^{1/2}$. Fig. 3.8 shows the distribution of the source vapor flux leaves the surface in geometric shape of a sphere having a cosine distribution. The perpendicular flux can be represented by J_o and flux at some angle from the point evaporation can be represented by $J_\theta = J_o \cos\theta$.[64,65]

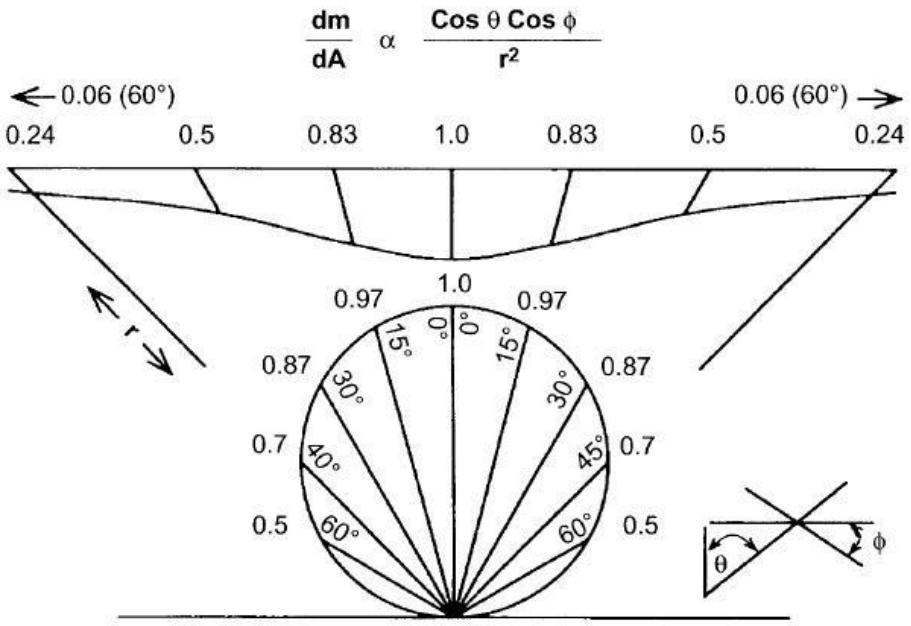

Figure 3.8: Cosine distribution of vapor particles leaving a point on the source[64]

3.4.3 Film Nucleation and Growth

Prior to deposition, film nucleation and growth starts with the substrate's surface conditions. The characteristics of the substrate's surface morphology, chemistry, flaws, outgassing, contamination and mechanical properties need to be consistently controlled to have a reproducible process. During the deposition there three stages of film nucleation and growth; adsorption, nucleation and continued growth on deposited material (condensation). The first stage of adsorption starts with the arrival of the source vapor to the substrate surface. With the vapor molecules a few atomic distances from the substrate, an attraction occurs between the two due to van der Waals force. The molecules then have some degree of mobility over the substrate's surface and are called adatoms. The adatom's degree of mobility depends on the energy of the adatom, adatom and surface chemical bonding and the surface's temperature, free energy and

crystallographic plane orientation. The second stage of nucleation begins when the adatoms lose mobility and form a nucleation site. With the presence of strong chemical bonding between the adatom and surface, each surface atom can act as a nucleation site. Without a strong chemical bond, the adatom will have high mobility. Preferential nucleation sites will be created when the highly mobile adatoms arrive at surface inconstancies such as lattice deflects (grain boundaries or point deflects), atomic steps, impurities, crystallographic orientation or charge sites on insulating substrates. In addition, highly mobile adatoms can collide with each other creating preferential nucleation sites.[64,65]

Once nucleation sites are created, diffusion between the deposited atoms and the substrate surface may occur to form an interfacial region. The adhesion and electrical properties of the film are dependent on interfacial region. In the third stage of growth, additional adatoms are collected on nucleation sites. The collection of adatoms or growth occurs laterally over the surface which is called wetting or perpendicular to the surface which is called dewetting. When there is weak chemical bonding between the nuclei and surface dewetting growth typically occurs forming less dense films that contain voids. In addition, weak bonding can create the nuclei to move like a liquid over the surface and crystallography align with each other. Conversely, when the bond is strong between the nuclei and surface wetting typically occurs. A special case called epitaxial growth occurs when there is a strong bond with no interfacial region formation and the nuclei's orientation is influenced by the substrate's surface crystallographic orientation. In the cases where there is weak bonding, no interfacial region formed and little substrate influence on growth, amorphous films typically form.

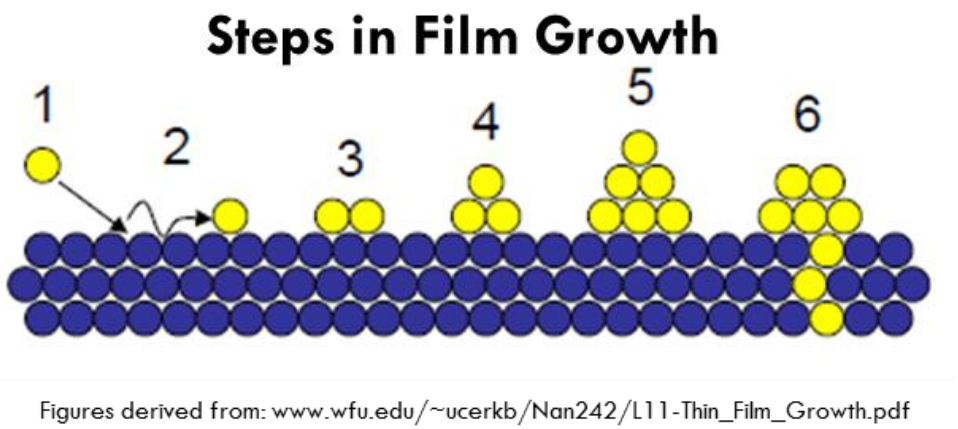

Figure 3.9: Steps in film growth[71]

Summary of Steps of Film Growth:

1.) Physical Absorption of the mobile vapor molecule

2.) Surface diffusion of the molecule which minimizes surface energy

3.) Chemical bonding of the molecule to substrate and molecule to molecule.

4.) Nucleation in which the energy barrier decreases as substrate temperature decreases and/or deposition rate increases.

5.) Microstructure formation of crystal structure and defects

6.) Bulk changes such as diffusion and grain growth

In step #4 there is heterogeneous nucleation in which the energy barrier of nucleation is described in Fig. 3.10.[71] During nucleation and growth, there is the potential of three forms of atom interaction with the film; physisorption, chemisorption and desorption in which the atom is ejected. In the case of physisorption and chemisorption there are local Gibbs free energy barriers to overcome which can be expressed in terms of a critical particle radius (r*) and critical energy barrier (ΔGV^*). During heterogeneous nucleation, the substrate's solid surface reduces the surface

energy by reducing the surface area. Nucleation depends on the wetting angle and relative surface energies produced from various interfaces such as between the substrate and vapor, film and substrate and film and vapor. The adsorption of an atom to the surface creates a tension in the surface atoms from stretching their bonds in response to the new atom and this produces surface energy. Once the critical radius and energy barrier are reached nucleation of the film will proceed.

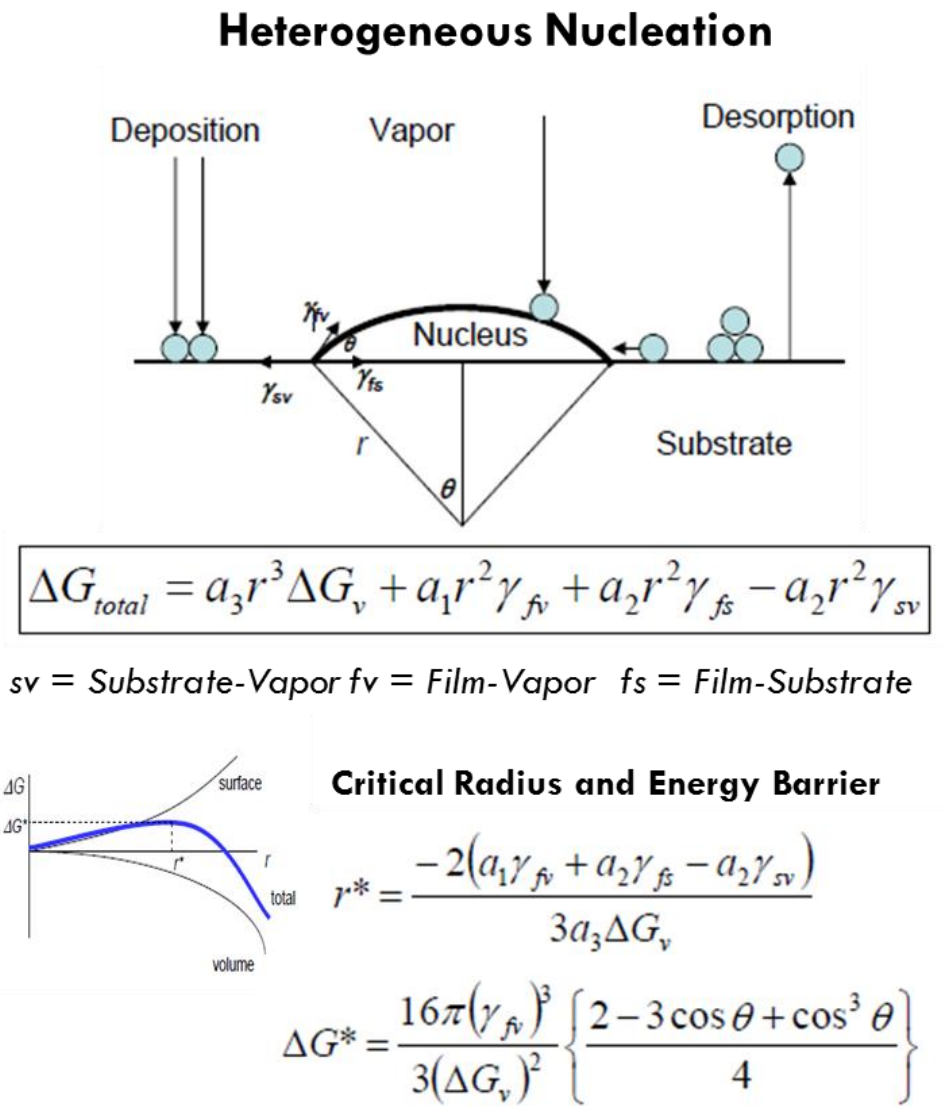

Figure 3.10: Step #4 in Film Growth, Heterogeneous Nucleation[71]

3.4.4 Glancing Angle Deposition (GLAD)

The past decades have resulted in a number of new insights on effective morphology controlled by variations in the static and dynamic substrate positioning. An effort to design and fabricate a multifunctional electron beam deposition system with capabilities including glancing angle, rocking through a programmable rotating substrate drum was undertaken. The ability to design a servo motor controlled horizontally rotating substrate drum that also exhibits the ability to adjust the deposition height in the vertical direction presented an acute mechanical design challenge that is not addressed by commercially available systems.

In a physical vapor deposition technique called glancing angle deposition (GLAD), the morphology of the film growth can be controlled through substrate rotational positioning at defined oblique angles to the source. Fig. 3.11 shows a typical glancing angle deposition apparatus.[72]

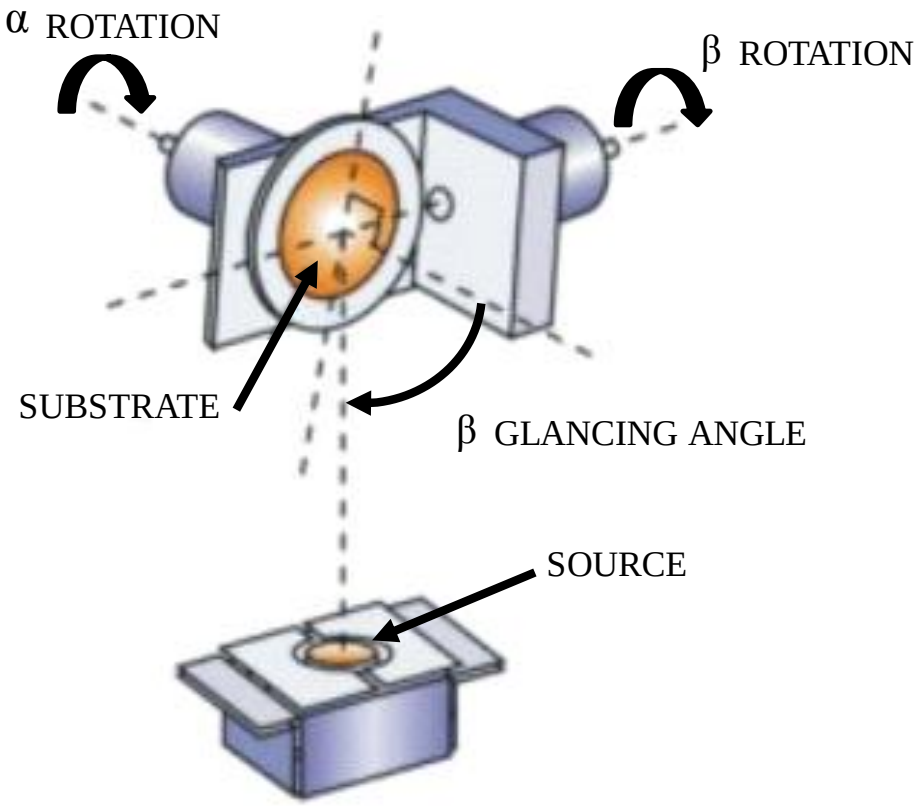

Figure 3.11: Typical glancing angle deposition apparatus[72]

The oblique angle positioning of the substrate relative to the source creates a lateral direction film growth component. This lateral film growth produces a shadowing effect from the incident deposition flux shown in Fig. 3.12.[72]

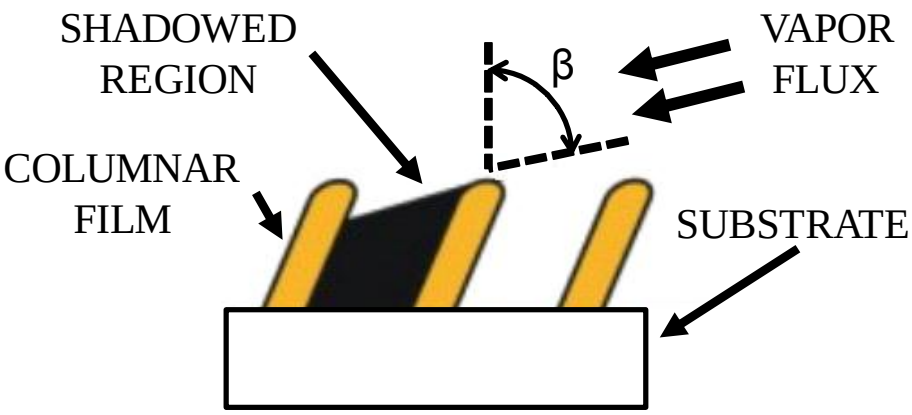

Figure 3.12: Glancing angle shadow effect[72]

Columnar film morphology is the result of the shadow effect. Changing the oblique angle positioning of the substrate relative to the source, changes the incident flux direction and therefore changes the angular growth direction of the columnar film. Rotating the oblique angled positioned substrate during the deposition will shape the geometry of the columns. In addition to the rotation rate, the geometry of the columns will have dependence on the deposition rate. By allowing the substrate to have a high rotational rate relative to the deposition rate vertical columns will result. A lower rotational rate relative to the deposition rate will produce helical columns. Fig. 3.13 shows the dependence of thin morphology on various process parameters.[72,73,74]

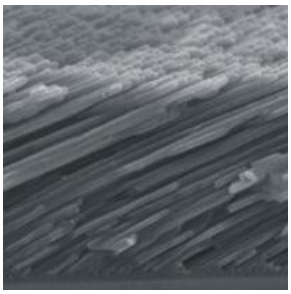

SLANTED NANOCOLUMNS:
Corresponds to holding axis α and β fixed throughout the deposition with glancing angle 30 < β < 80 .

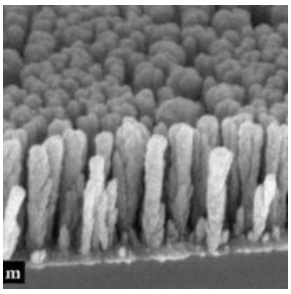

VERTICAL NANOCOLUMNS:
Corresponds to rapidly rotating axis α during the deposition.

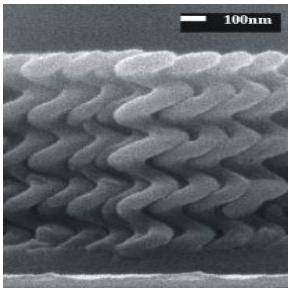

HELICAL NANOCOLUMNS:
Corresponds to slowly rotating axis α during the deposition.

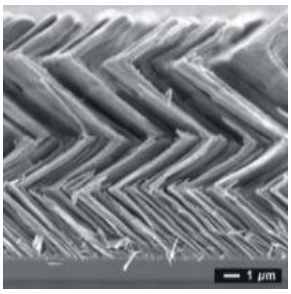

CHEVRONS:
Corresponds rotating β axis back and forth in 180 intervals. These are slanted nanocolumns deposited on each other with reversing directions.

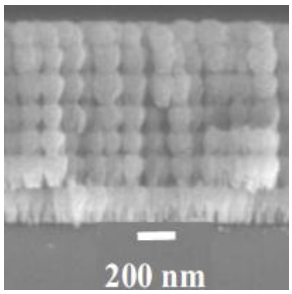

BALL NANOCOLUMNS:
Corresponds to rapidly rotating axis α and rotating axis β to change the glancing angle throughout the deposition.

Figure 3.13: Description of various GLAD[72,74]

4 Experimental Techniques

4.1 Preparation of the Thin Film Substrate (Current Collector)

Prior to the deposition the substrate, which served as the cell's current collector, was prepared using unpolished high-strength aluminum alloy 7075 (McMaster-Carr) with a thickness of 0.8mm. The Al-7075 substrate was cut into a 25mm x 75mm strip with the grains running parallel to the width of the strip. The Al-7075 strip was cleaned using a Kimwipe® which was soaked in acetone, then cleaned with methanol and placed in the center of a flat substrate holding plate along with two cleaned glass microscope slides 25mm x 75mm with a thickness of 1mm. Fig. 4.1 shows the substrate holding plate made of aluminum and the Al-7075 substrate and glass reference slides attached. The glass slides were laid flat and place on each side of the Al-7075 strip and the three pieces were secured to the substrate holding plate using Kapton® tape. The glass slides were later used to measure film thickness with a stylus profilometer. Once the film was deposited on the Al-7075 substrate and removed from the vacuum chamber, 14.3 mm diameter discs to be used as the cathode and current collector within the coin cell assembly were punched with a manual hand press such as the one shown in Fig. 4.2.

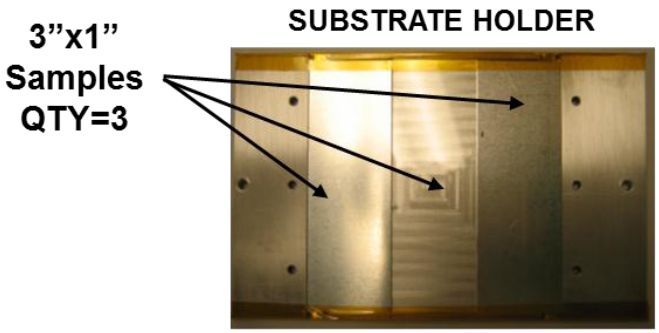

Figure 4.1: Substrate holder showing attached Al-7075 strips and glass slide

Figure 4.2: Typical manual hand press used to punch the substrate/film into discs

4.2 Programming of the Dynamic Substrate Drum System

The positioning of the dynamic substrate drum was controlled through Ormec servo motor hardware which included an F-Series PLC motion controller, power supply, servo drive and servo motor. This hardware is shown in Fig. 4.3 along with the wiring diagram that was used to assemble the components.[73] The software used in the dynamic substrate drum system was BASIC language loaded on a PC which interfaced with the PLC motion controller. The positioning of the drum was based on a servo count command (CNT) in which 77.625 CNT/degree. The drum rotation direction was +CNT for counterclockwise and -CNT for clockwise.

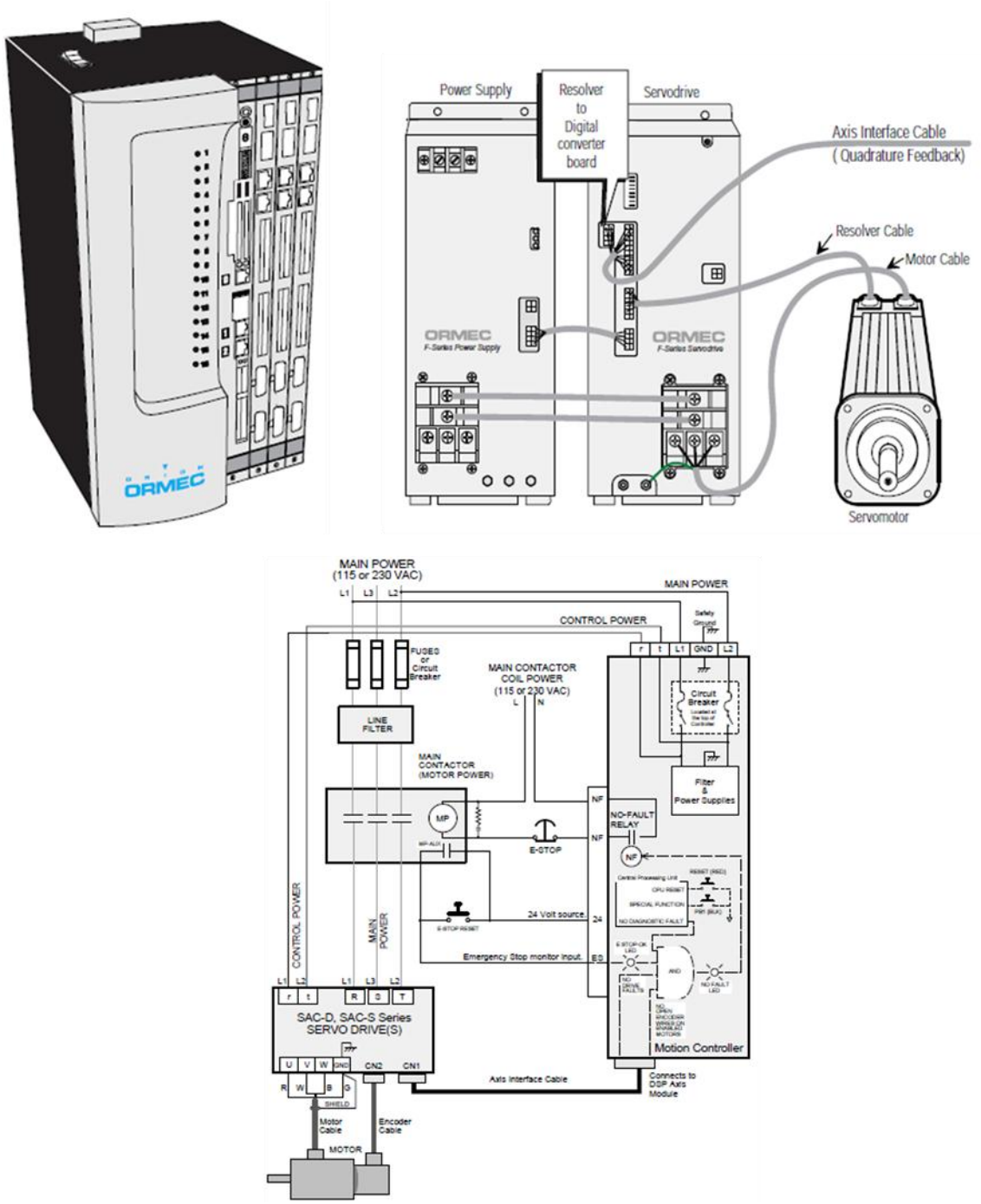

Figure 4.3: Ormec servo motion controller assembly and wiring diagram[73]

4.3 X-Ray Diffraction (XRD)

Approximately, 95% of all solid materials are classified as crystalline. By definition, in crystalline materials atoms are arranged in a regular pattern and the smallest volume element is called a unit cell. Contrast to crystalline is amorphous materials in which the atoms are arranged in a randomly and similar to the disorder found in a liquid.

The unit cell dimensions of a crystalline material are described by three axes a, b and c (lattice parameters) and the angles between them alpha, beta and gamma. The unit cell defines the crystal structure and repeats in all dimensions to fill space and produce the macroscopic crystals of the material. Parallel planes of atoms within the unit cell, shown for example in Fig. 4.4, define directions and distances in the crystal.[76] Miller indices (hkl) are used to identify different planes of atoms and define the reciprocal of the axial intercepts. The crystallographic direction is defined as [hkl] and is the vector normal to the (hkl) plane of atoms. The vector extending from the origin of the unit cell normal to the plane (hkl) is defined as d_{hkl}.

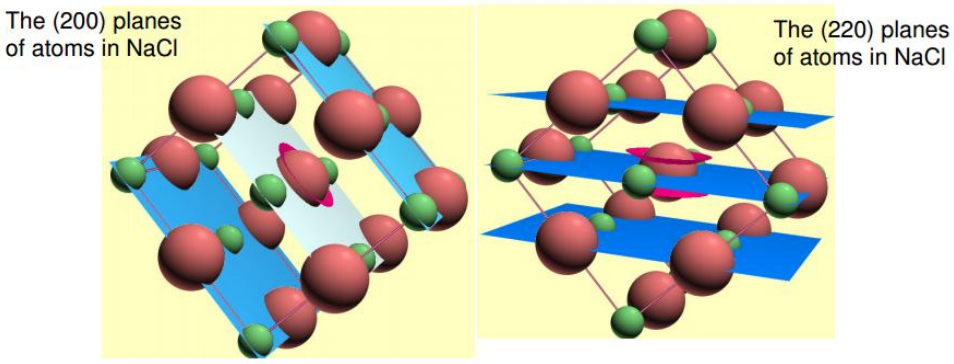

Figure 4.4: NaCl unit cell showing atomic planes[76]

The scattering of X-rays from atoms produces a diffraction pattern which is a result of the specific atomic structure of a crystalline material and the diffraction peaks are associated with the distance between parallel planes of atoms. For amorphous materials only broad scattering peaks are produced because they not have long-range atomic order. Diffraction is produced when light is scattered by a periodic array with long range atomic order which creates constructive interference at specific angles. During X-ray diffraction the beam strikes an atom and the electrons around the atom start to oscillate with the same frequency as the incoming beam. A destructive interference is created in all directions in which the combining waves are out of phase and there is no resultant energy leaving the solid sample. Due to the fact that the atoms in a crystal are arranged in a regular pattern very few directions will have constructive interference. This creates a situation where the waves will be in phase and well defined X-ray beams will leave the sample at specific directions depending on the crystal structure. The strength in which an atom scatters light is proportional to the quantity of electrons associated with the atom.

Bragg's law calculates the angle where constructive interference associated with scattered X-rays from parallel planes produce a diffraction peak as shown in Fig.4.5.[76] The X-ray wavelength λ is typically fixed and a family of planes produces a diffraction peak only at a specific detector angle 2θ. The vector d_{hkl} is used in Bragg's law to determine the location of diffraction peaks.

$$\lambda = 2d_{hkl} \sin\theta$$

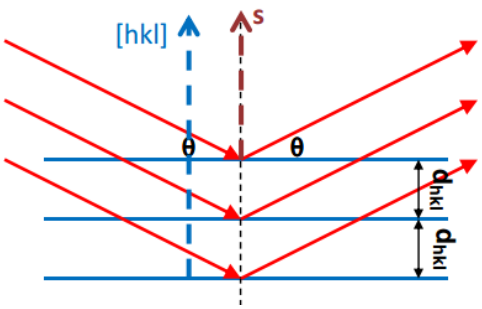

Figure 4.5: Definition of Bragg's law[76]

The arrangement of atoms in the entire crystal determines the intensity of the diffraction peaks. The diffraction peak is the result of summing the scattering from all the (hkl) planes of atoms in the unit cell which can be described by the F_{hkl} equation in Fig. 4.6. The equation shows that the amplitude of scattered light is determined by where the atoms are on the atomic planes and is expressed in terms of the fractional coordinates $x_j y_j z_j$. The scattering factor f_j quantifies the efficiency of X-ray scattering at any angle by the group of electrons in each atom and is equal to the number of electrons around the atom at detector angle theta (θ)= 0° then drops off as θ increases. Nj is the fraction of every equivalent position that is occupied by atom j.

$$I_{hkl} \propto |F_{hkl}|^2$$

$$F_{hkl} = \sum_{j=1}^{m} N_j f_j \exp\left[2\pi i\left(hx_j + ky_j + lz_j\right)\right]$$

Figure 4.6: Definition of diffraction peak intensity

For the experiments XRD was used for sample phase confirmation, determining purity and orientation indentification. X-ray diffraction was performed on a Bruker D8 advanced diffractometer shown in the Fig. 4.7 with a CuKα source in the 2θ range from 20-37° and 48-65°at a scan rate of 0.06°/min.[5] The range from 37-65°was removed

from the scan to due to large peaks from the Al-7075 substrate creating noise which prevents evaluation of the thin film in this range. The samples were placed on a glass slide and secured with Kapton™ tape on the edges. Once the scanning was completed Eva and Topas software was used to analyze the raw data file to determine the crystallite size, FWHM, peak height, dspacings and lattice parameters. To verify the lattice parameters determined by Topas, an excel spreadsheet created at Durham University and provided through their website was used along with the d-spacings from Topas to calculate the lattice parameters.

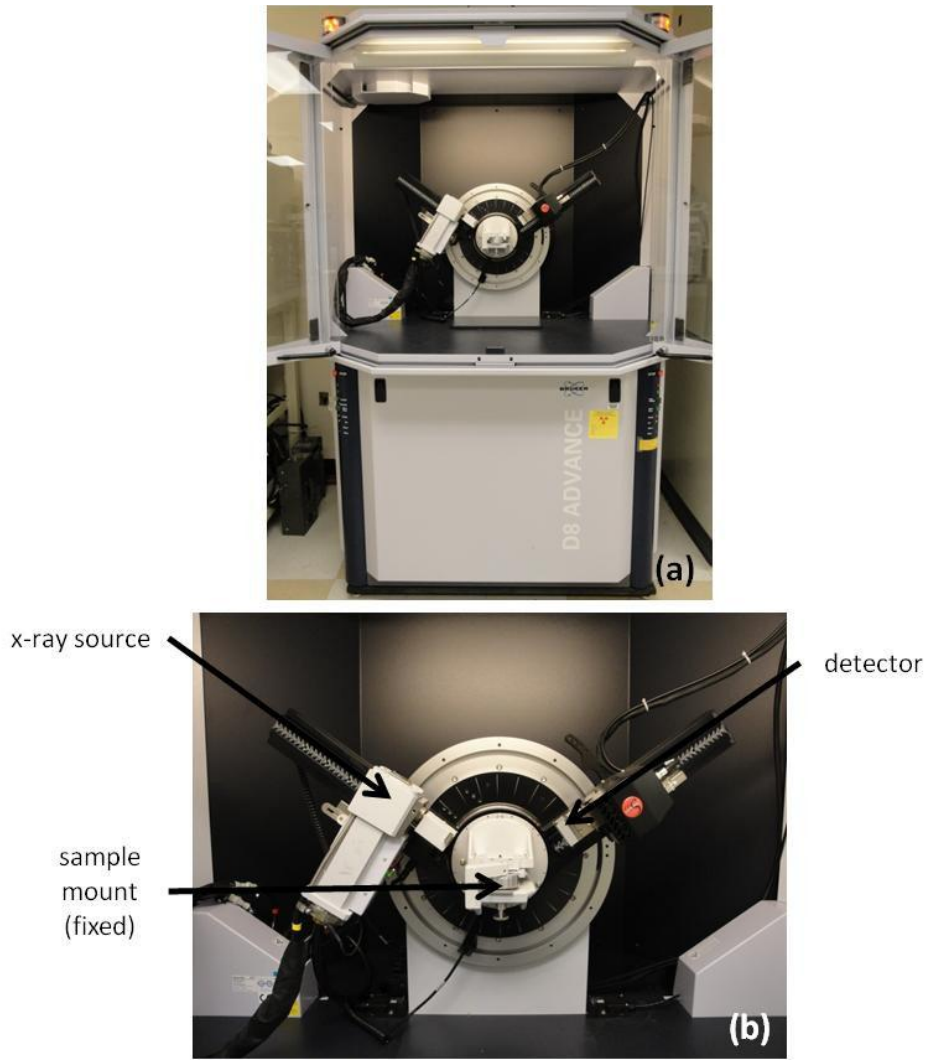

Figure 4.7: X-ray diffractometer used for the majority of XRD experiments a Bruker D8[5]

4.4 Stylist Profilometer Thin Film Thickness Measurement

A surface profilometer takes surface topography, roughness and step size surface measurements using contact profilometry techniques. Surface profilometers are accurate, reliable, repeatable and relatively inexpensive. The stylus tip is typically made of diamond and is moved in the vertical direction to contact the sample and then moves horizontally across the surface of sample. The radius tip of diamond stylus ranges from 20 nanometres to 50 μm and is selected based on the sample specifications. The scan

distance and force applied to the sample is for a specified through software commands. The profilometer is capable of measuring surface variations typically 10 nanometers to 1 millimeter in the vertical stylus displacement direction as a function of horizontal positioning. The stylus's height position generates an analog signal which is converted into a digital signal stored, analyzed and recorded. The resolution is controlled by the scan speed and data signal sampling rate. The stylus force applied to the sample can range typically from 1 to 50 milligrams. For the experiments a Dektak 150 from Veeco surface profilometer was used such as the one pictured in Figure 4.8. The Dektak 150 has features such as 3D topography mapping capability and 4-angstrom repeatability. The image in Fig. 4.9 shows a 3D topography mapping of the dynamic 58-62° film used to understand the surface roughness. The parameters for the profilometer scans were 2.5μm stylus radius, scan force of 2.5mg, scan length 500-1000μm, scan duration of 45sec and a resolution of 0.056μm.

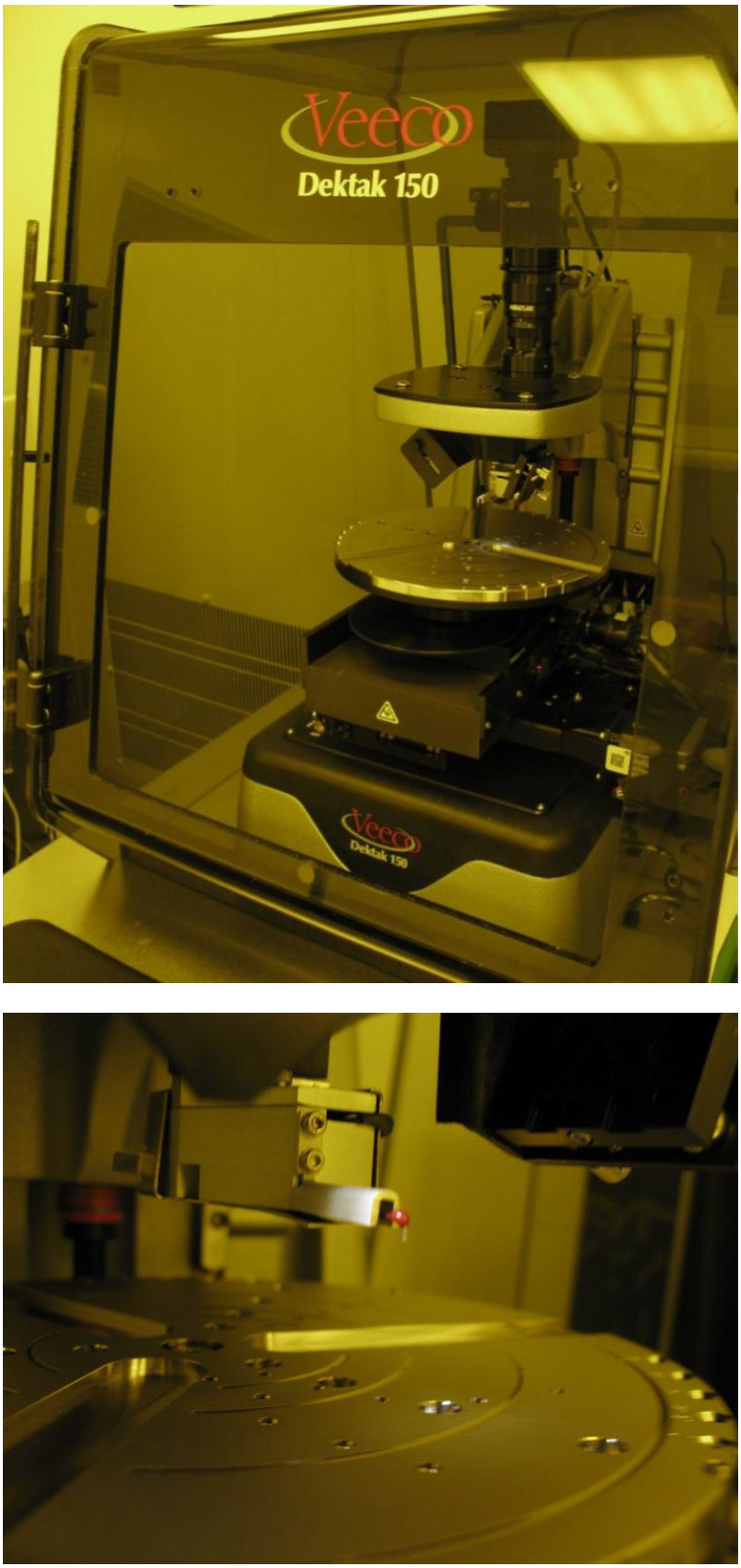

Figure 4.8: Dektak 150 Profilometer used to measure film thickness and topography

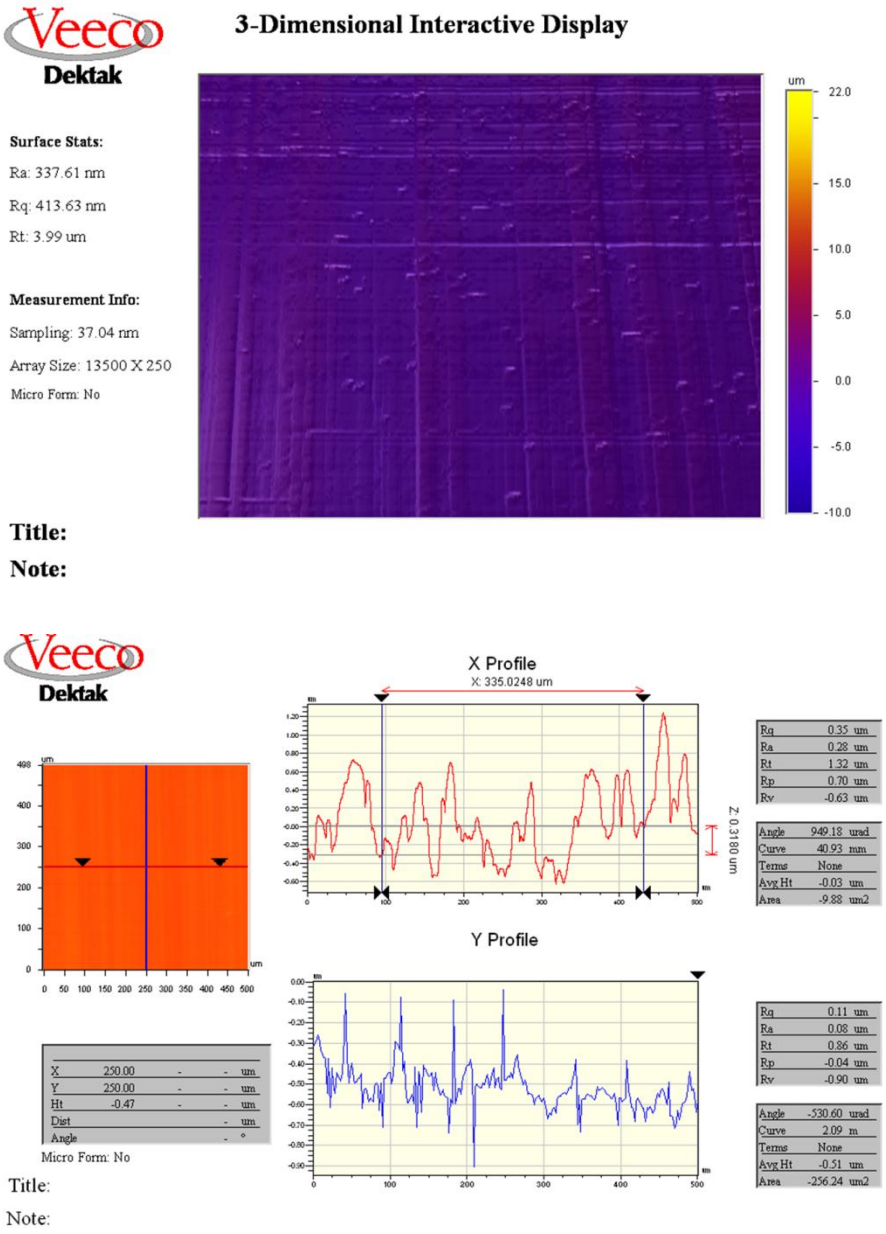

Figure 4.9: Dektak 150 Profilometer3D topography mapping of a 58-62° FeF_2 thin film.

4.5 Field Emission Scanning Electron Microscope (FESEM)

FeF_2 films were analyzed with a Field Emission Scanning Electron Microscopy (FESEM) (Zeiss ΣIGMA Field Emission SEM with Oxford EDS). The ΣIGMA is able of resolving structures as small as 1.5nm at 15 kV and 2.8nm at 1 kV. The microscopy has

acceleration voltages from 0.2-30 kV, utilizing a ZrO-W Schottky field emission source. The microscopy has high resolution imaging capability with a magnification range of 10x -1,000,000x. Fig. 4.10 shows an image of the type of microscope used in the experiments.

A field emission scanning electron microscope (FESEM) creates high resolution three dimensional images of a sample. The microscope performs by bombarding a sample with a focused beam of electrons which ejects secondary electrons from the sample's surface. Within the microscope is a detector that systematically registers the ejected electrons from the sample. The data from the detector is analyzed to determine the origin and emission intensity from the ejected electron which can then be assembled into a high contrast and high resolution image.

Figure 4.10: A Zeiss ΣIGMA Field Emission SEM used in the experiments

4.6 Electrochemical Characterization

All batteries fabricated for studies in this paper were aluminized 2032 coin cells (NRC) made with cathodes consisting of a 14.3 mm diameter disc of iron fluoride film, two layers of borosilicate glass fiber separator (Whatman) with a diameter of 15.9 mm soaked with electrolyte, and a 0.3mm thick 12.7mm diameter lithium metal foil as the anode counter electrode (half-cell) (FMC). The electrolyte was 1 M LiPF6 EC: DMC purchased from Ferro, stored in a helium filled glovebox and used without additional treatment. Galvanostatic cycling tests were performed on a MacPile II (Biologic). The cells were cycled galvanostatically between 4.50 V and 1.00 V at a constant current of 12.5 mA g-1 in an oven set at 60^{o}C.

To investigate the porosity of the cell, electrochemical impedance spectroscopy (EIS) was performed with a Solartron Models SI 1287 and SI 1260. The SI 1287 is capable of controlled potential and current techniques and requires pairing with the SI 1260 to perform electrochemical impedance spectroscopy. The two units are controlled by a computer through GPIB running ZPlot software (Scriber Associates). Fig. 4.11 shows of a picture of the system in the lab that was used for the experiments.[5] The EIS was performed at room temperature with a frequency range of 10^{-3} to 10^{5} Hz and AC voltage of 80mV. Using the Zplot software, the CPE-T value was generated and used to compare the relative porosity of the thin films.

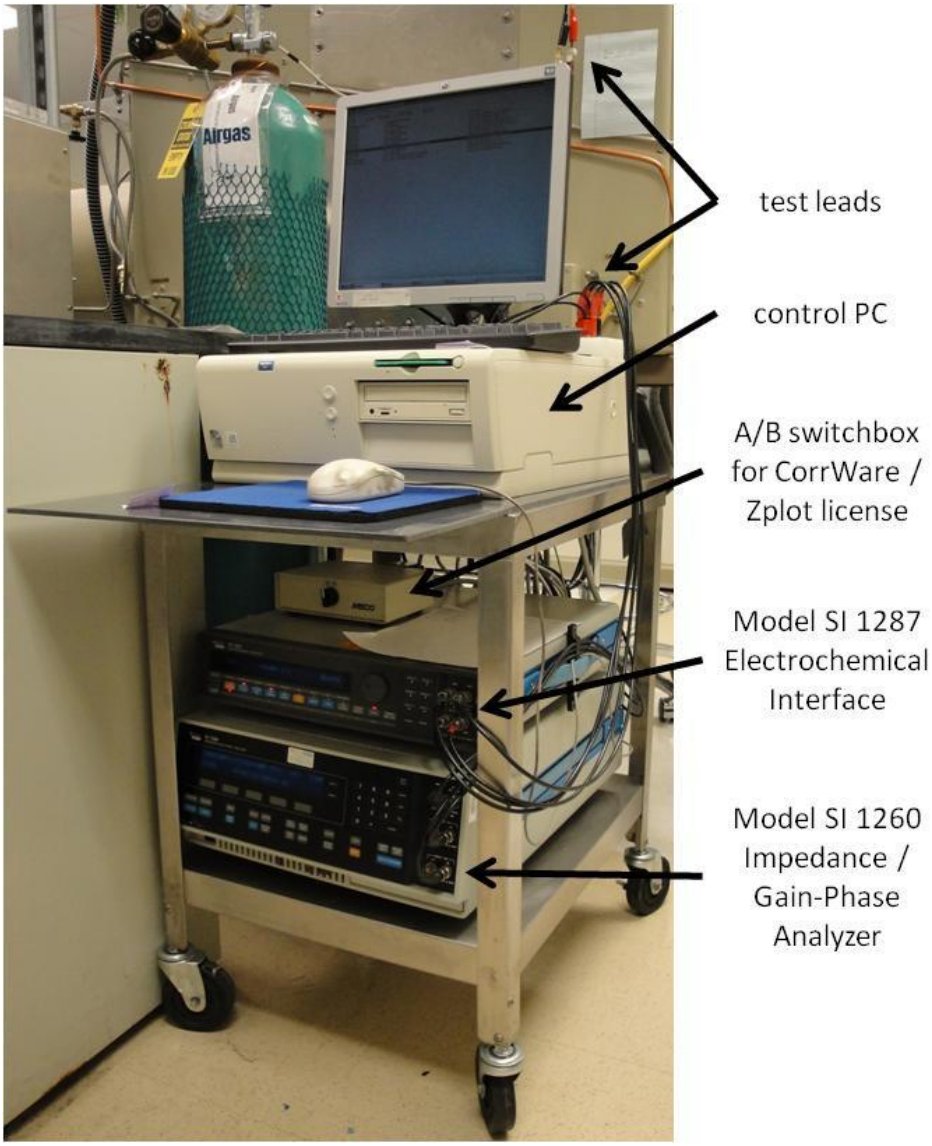

Figure 4.11: Solartron Models SI 1287 and SI 1260 used for EIS in the experiments[5]

5 Design and Fabrication of a Custom E-beam Deposition System

5.1 Project Background

The opportunity presented itself through a previously used multiple chamber web coating vacuum system shown in Fig. 5.1. The chamber system's dimensions were 13x7x4 feet and consisted of nine chambers which contained various PVD stations for

manufacturing thin film batteries. There were five cryogenic pumps, four diffusion pumps and rotary vane rough pumps which supplied the vacuum for the system. Conventron, baratron and ion gauges monitored the pressure level of the system. In addition, the system contained mass flow controllers, servo motors operated by a program logic controller (PLC) along with other thin film vacuum hardware. The objective of the project was to create a custom thin film deposition system by utilizing the system and hardware provided. New PVD equipment would be purchased that would best suit the application requirements. The scope of the project was a two year extensive undertaking consisting of planning, disassembly, design, fabrication, assembly and validation.

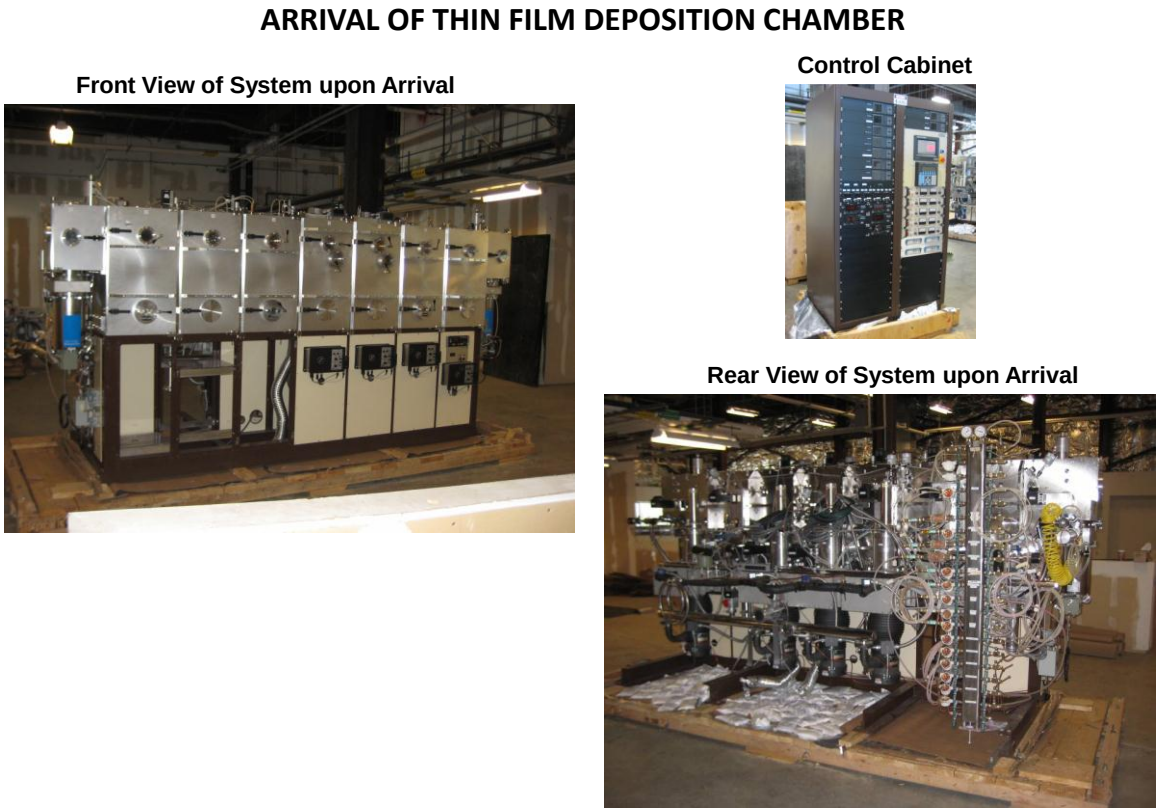

Figure 5.1: Previously used multiple chamber web coater

5.2 Vacuum Chamber Preparation, Assembly and Testing

Before the arrival of the system into the lab the planning phase of the project took place. A detailed schedule was made to estimate the timing to completion and to track any unexpected items that would arise during the vacuum chamber development. This schedule was a living document and was updated throughout the development. The planning phase started in September 2009 and was completed in July of 2011. Fig. 5.2 shows the tracking schedule that was used throughout the development.

Due to the large size of the system there was a concern that the system would not fit into the lab space. Footprint measurements, computer aided design drawings and full scale templates were used to determine the best way to move the system into the lab. It was determined that some disassembly of the system was required in order to ensure a successful move. The two chambers on the ends of system had to be disassembled along with pumps, vacuum piping and other external loose hardware. After two months of disassembly and preparing the lab, the system was successfully moved into the lab.

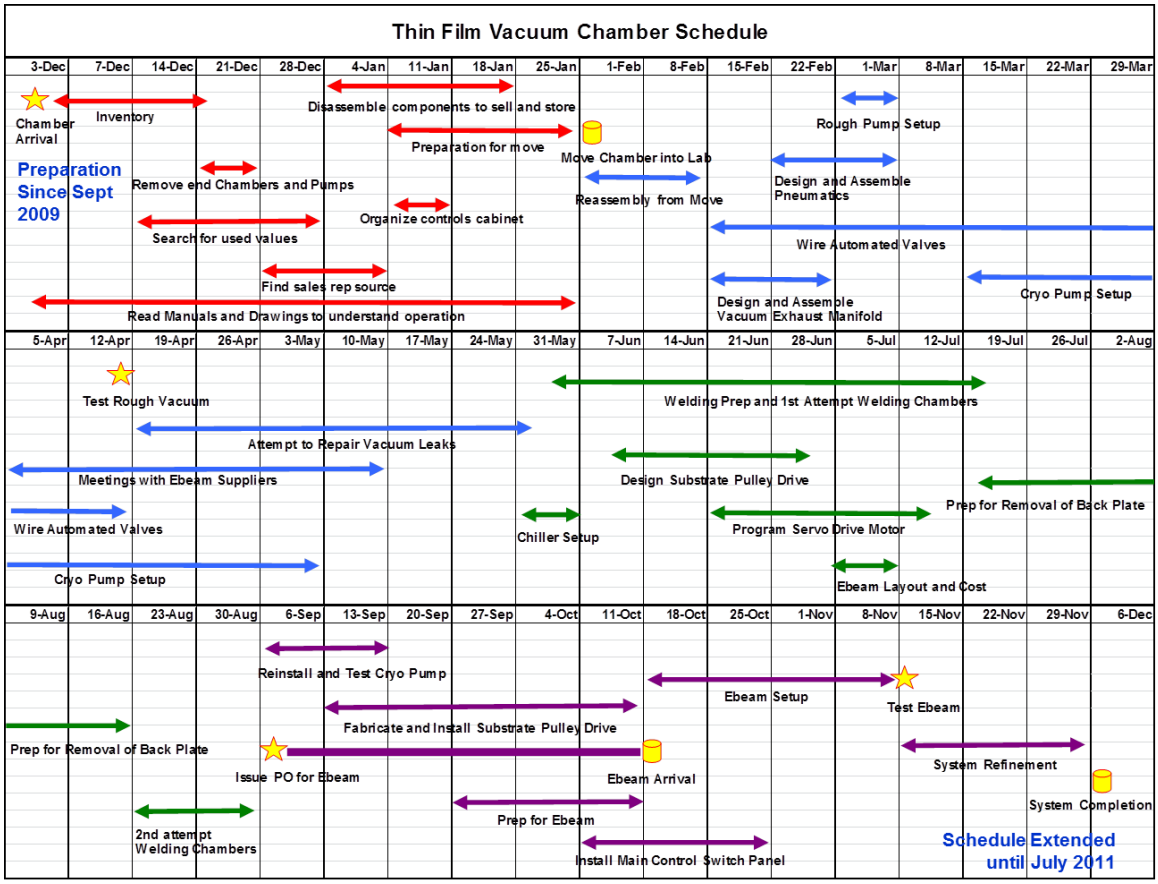

Figure 5.2: Detailed planning schedule for the vacuum chamber development

In addition to moving the system into the lab, the planning phase of the project included selection of a newly purchased PVD system for the chamber. Extensive investigation went into the types of e-beam systems and manufacturers prior to purchasing the specific system. By reviewing the advantages and disadvantages of the types of PVD systems it was determined that an e-beam would be best suited for the applications the lab planned to pursue.

Once the system was moved into the lab, the phase of design, fabrication and assembly started. It was determined that the chambers would be most functional as independent vacuum chambers. The nine chambers would be divided into three

independently operated chambers. This project focused on designing one of the three chambers with the other two being available for customization in the distant future. The original system was designed to be fully automated and ran through a central PLC panel. Since the chamber was being divided into separate chambers the PLC panel would not be utilized. Even though there was no longer a central PLC the electrical and pneumatic vacuum valves would be needed. A new custom central manual switch panel was fabricated to replace the PLC and control the valves shown in Fig. 5.3. In addition, the vacuum pipes and the control towers where reconfigured to meet the requirements of the individual chamber. After completing these modifications the rough vacuum of the individual system was tested.

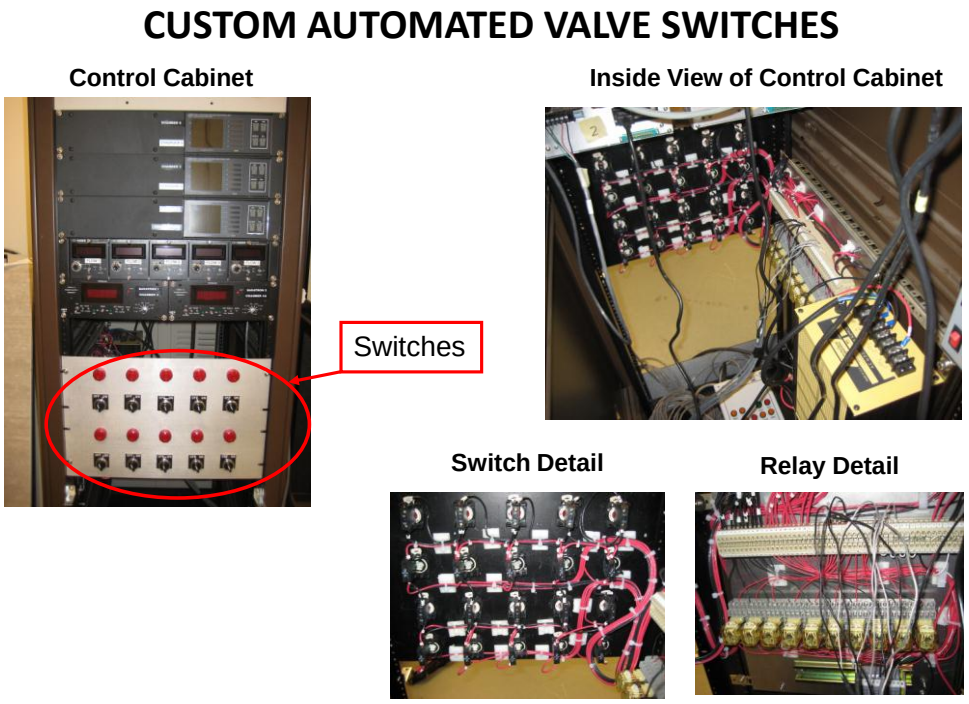

Figure 5.3: Completed ebeam deposition chamber valve switch panel

Prior to testing the rough vacuum, the nine interconnected chambers of the web coater needed to be separated into individual chambers. Steel plates were TIG welded as inside walls dividing the chambers individually as shown in Fig. 5.4. In preparation for welding, the large steel chamber backing plate weighting approximately 925lbs (~420kg) was unbolted and disassembled from the chamber. A 3”x3”x10’ L-shaped bracket was added under the backing plate to support the backing plate for the one inch move.

Finite element analysis (FEA) computer simulations (using CATIA V5 software) were used to determine the thickness, material type of the L-shaped bracket and the quantity of bracket mounting bolts needed to support the one ton weight of the plate. Fig. 5.5 shows the finite element analysis (FEA) computer simulations for when a force of 925lbs is applied to the support bracket made of A-36 steel. A maximum stress of 4.35MPa is experienced and the bracket’s yield stress is 150Mpa. Based on these results, there was more than enough strength to support the stainless steel backing plate. There were no concerns for the L-bracket mounting bolts since they were rated for 620MPa shear stress.

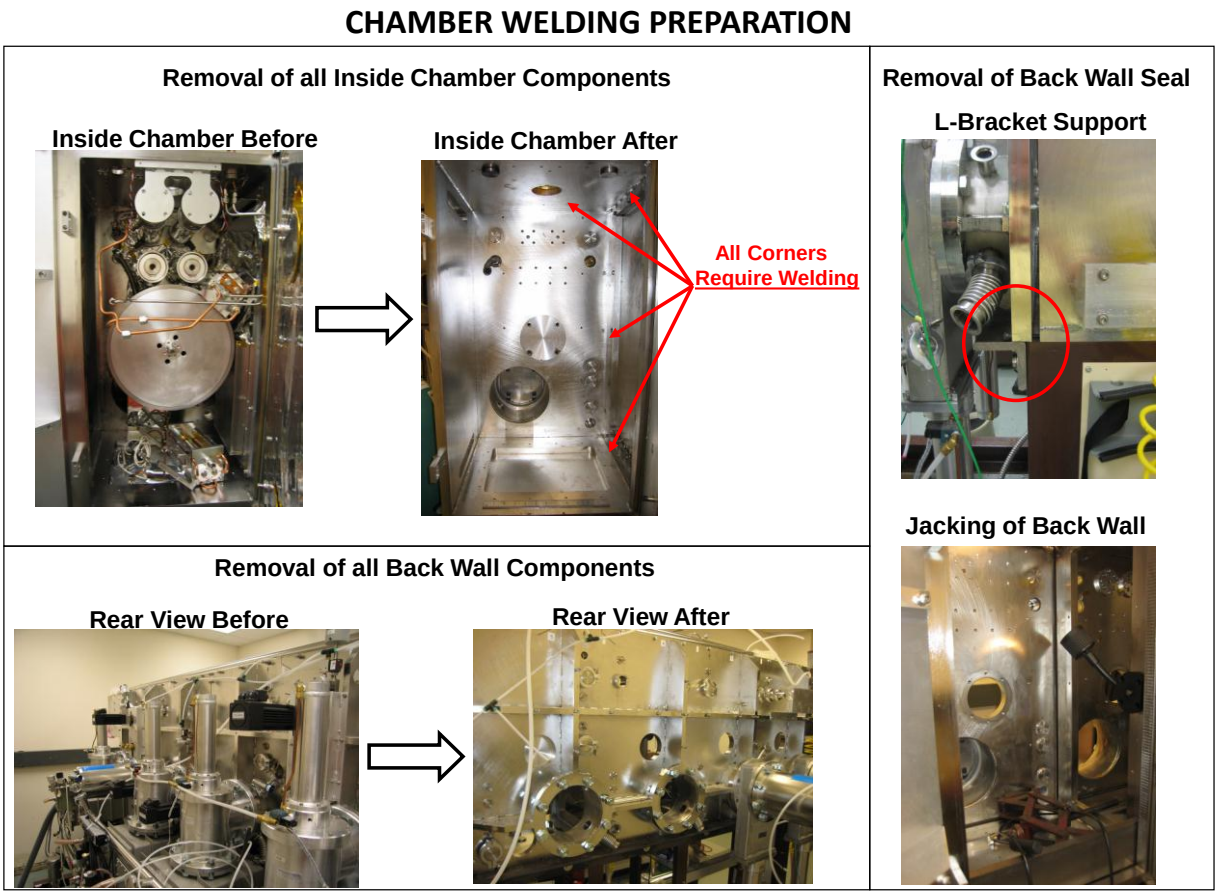

Figure 5.4: Removal and welding of the web coater chamber backing plate to create an individual custom chamber

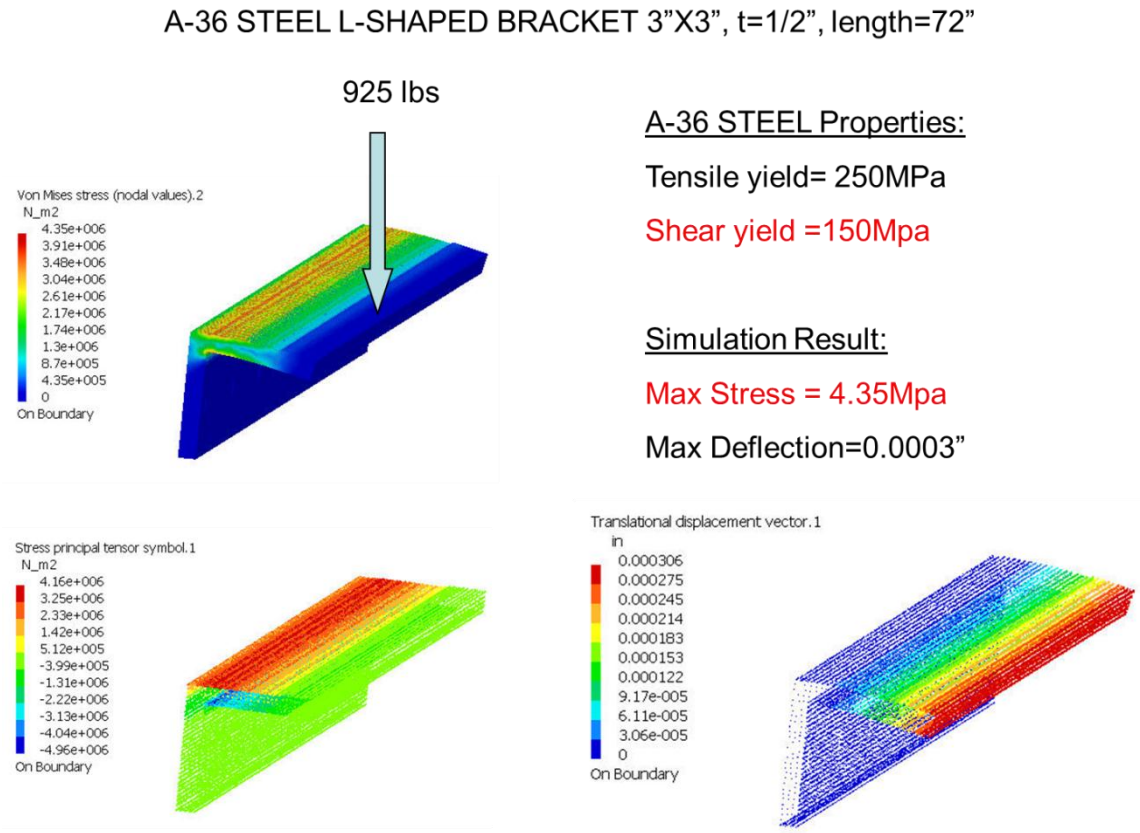

Figure 5.5: FEA simulation of chamber backing plate L-bracket support

The next stage of the project was to achieve high vacuum. During the removal of the back plate the cryo pumps had to be removed from the backing plate. To evaluate the high vacuum capability the cryo pumps were reassembled and connected to their helium compressor. A chiller would need to be purchased that met the cooling rate requirements of the compressor. To monitor the pressure during high vacuum an ion gauge was installed. The chamber's high vacuum capability was tested and achieved 1.0×10^{-7}Torr. With the achievement of high vacuum the chamber was ready for the design, fabrication and assembly of a novel thin film substrate holding drum and electron beam deposition system.

5.3 Design of a Programmable Substrate Drum System

A programmable (BASIC language) servo motor controlled substrate holding system was designed and fabricated with capability to produce glancing angle morphologies. The system was designed with a novel horizontally rotating substrate drum that also exhibits the ability to adjust the deposition height in the vertical direction.

Utilizing computer aided design (CAD) the system was initially developed in three dimensions (3D). Referencing the 3D design, two dimensional (2D) drawings were created to fabricate the individual components shown in Fig. 5.6.

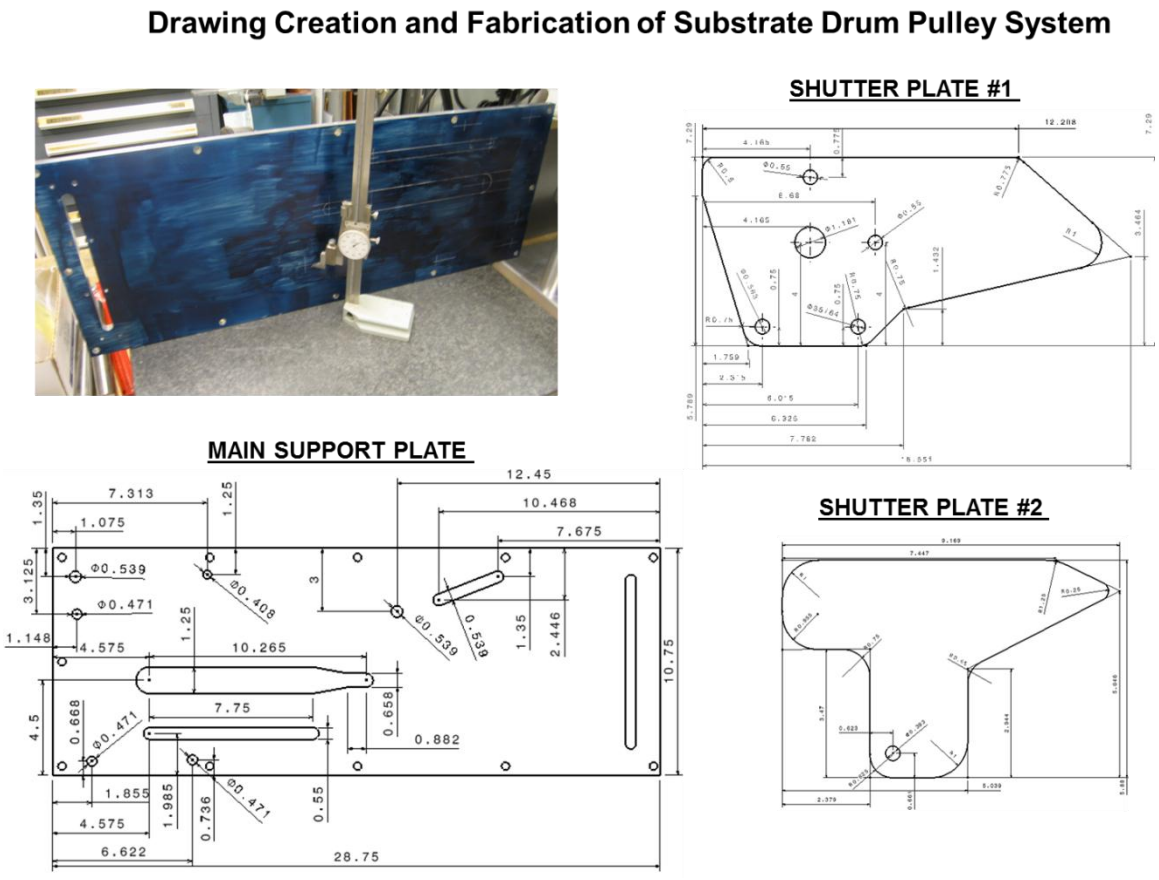

Figure 5.6: 2D Fabrication drawings of the substrate drum system

During the design of the deposition system three key variables were considered in order to control the glancing angle deposition morphology; the rotational velocity and angular direction of the substrate drum, the height of the substrate relative to the source and adjustment of the drum's geometry.

The components for the chain gear system were purchased from McMaster Carr and consisted of the following:

- Roller Chain Idler Sprocket STL W/Needle Bearing, for #25 Chain, 19 Teeth, 1/2" Bore (Quantity of 5)
- SS Machinable -Bore Roller Chain Sprocket for #25 Chain, 1/4" Pitch, 24 Teeth, 3/8" min Bore (Quantity of 2)
- Stainless Steel ANSI Roller Chain 25SS Single Strand, 1/4" Pitch, Rollerless,.130" Diameter, 5'L (Quantity of 1)

Considering these components along with the overall design of the custom substrate drive system, the drum positional resolution was calculated. The substrate drum's positional resolution was calculated from the belt attached to the servo motor, having a gear ratio of 100:1, to the drum where the substrate holder would be attached. Fig. 5.7 shows the result of the gear ratio summary to determine the substrate drum's resolution.

SUBSTRATE DRUM RESOLUTION:

Servo Motor Resolution = 4,096 counts/rev

Resolution with Gear Ratio (100:1) = 409,600 cts / rev

Belt Drive Gear Ratio= 4.75"/1.375" : 1 = 3.45:1

Resolution with Belt Drive =
409,600 x 3.45 = 1,413,120 cts / rev = Y

Resolution with Sprocket=
Y / (0.25" pitch x 24 teeth) = 235,520 counts / inch

Degree / Count = 360 / Y = 0.0015285 degree / count

2.05" diameter Arc Length / Count=
(6" / 360) x 0.0015285 = 0.00002547 inch

6" diameter Drum Arc Length / Count=
(18.85" / 360) x 0.0015285 **= 0.00008003 inch**
(2.033 microns)

Figure 5.7: Substrate drum positional resolution calculation

The control of the rotational velocity and angular direction of the substrate drum was achieved through the use of a programmable servo motor. On the outside of the vacuum chamber, the servo motor was attached to a ferrofluidic driveshaft feedthrough by means of a belt. Inside of the chamber, the size 25 roller drive chain connected the ferrofluidic driveshaft feedthrough to the substrate drum through the series of drive and idler gears listed previously. Fig. 5.8 shows a schematic of the internal components of a ferrofluidic driveshaft which holds a vacuum seal rated for 10^{-6} Torr by means of magnetic fluid.[77]

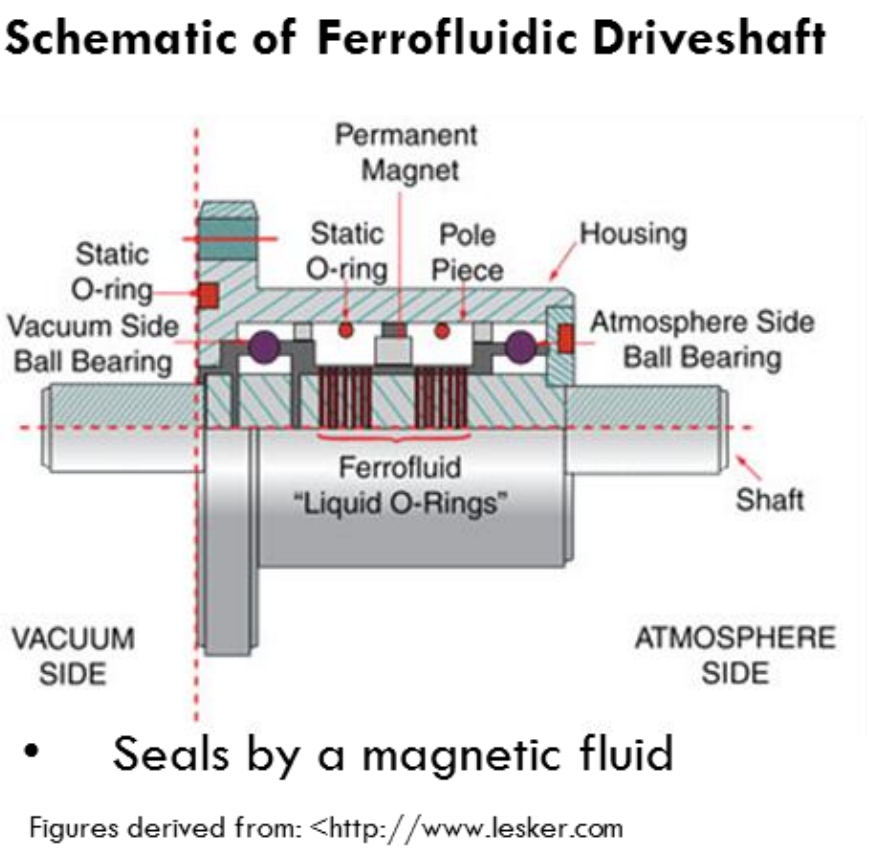

Figure 5.8: Schematic of a ferrofluidic driveshaft[77]

Fig. 5.9 shows the isometric, front and rear views of the 3D design of the system with the substrate drum in its minimum height position relative to the source. Fig. 5.10 shows the 3D design of the system with the substrate drum in its maximum height position relative to the source.

Fig. 5.10 shows the maximum height adjustment range of the substrate drum to be 185 mm. The height of the substrate drum was made adjustable by configuring the gears into a pulley system which is shown in Fig. 5.9 and 5.10. This pulley gear configuration follows the drum during height adjustments. A two piece chain shutter

moves in unison with the drum and assists the mounting plate to protect the chain from being coated during the deposition.

The adjustment of the substrate drum's geometry is achieved by replacing the drum prior to deposition. A threaded turn knob is loosened and removed to allow the drum to slide off of the drive shaft. A new drum which may contain a different size and/or shape can then be added to the drive shaft. Fig. 5.11 shows the removal of the drum.

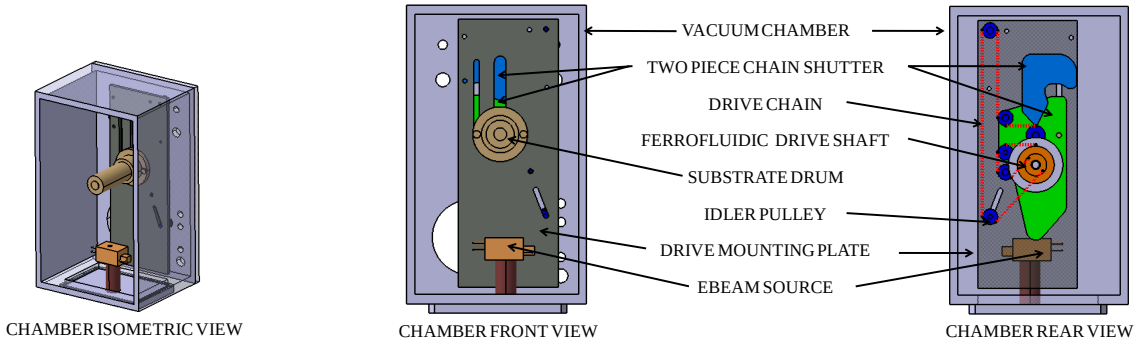

Figure 5.9: CAD showing the substrate drum in minimum height position

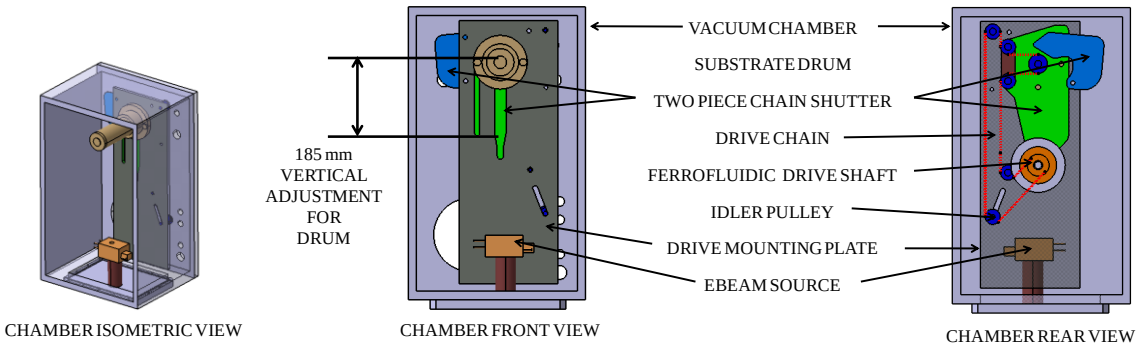

Figure 5.10: CAD showing the substrate drum in its maximum height position with 185mm of total vertical adjustment

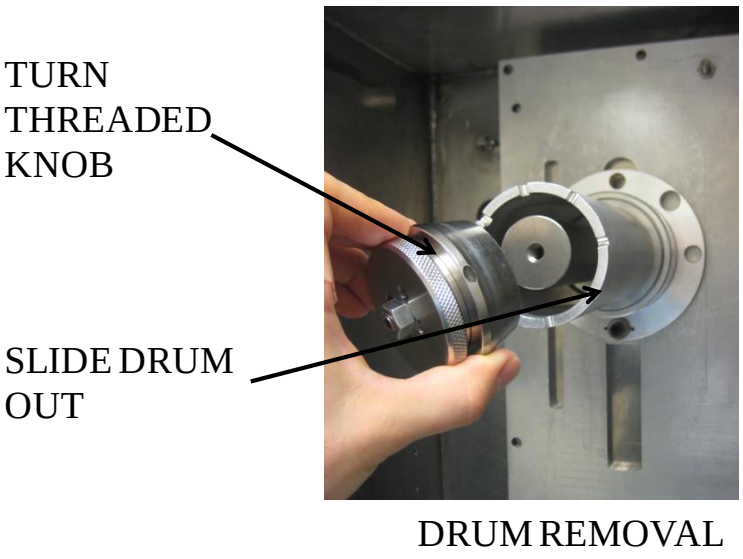

Figure 5.11: Disassembly for drum geometry modifications

The final result of the fabrication of the substrate drum system is shown in Fig. 5.12. The figure shows the front view of the substrate drive system with the system installed into the chamber. The substrate drive system was removed from the chamber to show the rear view of the system. The rear views of the system show the drum at its minimum and maximum height positions along with the two piece chain shutter adjustment locus. In addition, the figure shows the drive assembly feedthrough which is attached to the outside wall of the chamber.

In conclusion, a multifunctional deposition programmable substrate holding drum with capabilities including glancing angle, rocking, and rotating drum deposition was designed and fabricated. The system was designed with a novel horizontally rotating substrate drum that also exhibits the ability to adjust the deposition height by 185mm in the vertical direction.

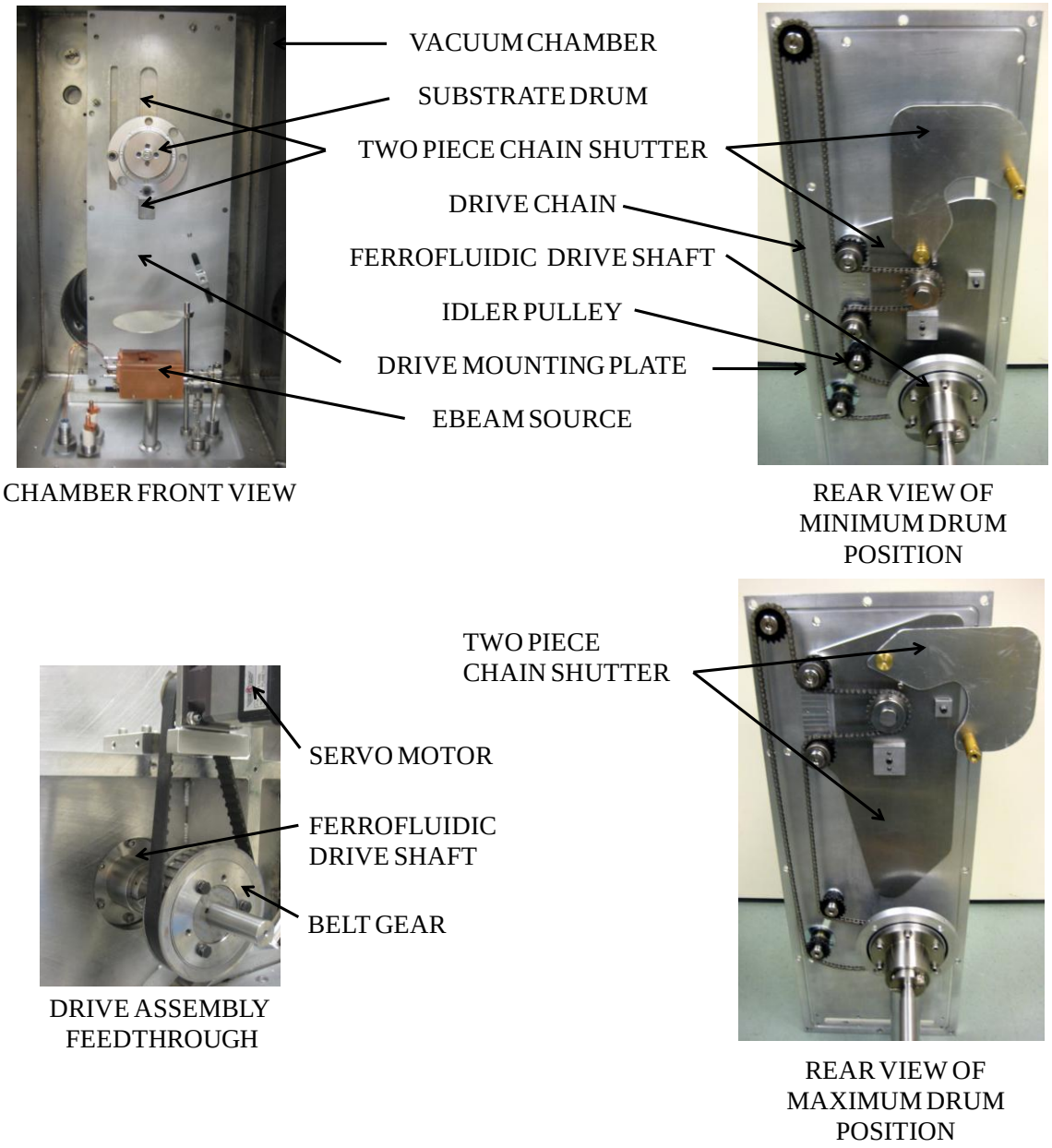

Figure 5.12: Completed fabricated substrate drum system

5.4 Design of an Electron Beam Deposition System

The design of the electron beam deposition system was completed concurrently with the design of the programmable substrate drum system. The location and mounting stand height for the electron beam gun was determined from the location and

height range of the substrate holder. The chamber was designed with the intention to add a second ebeam gun for co-deposition capability. However, initially there would be one ebeam gun. The chamber's bottom mounting plate which was attached by bolts and sealed with a Viton O-ring was removed, measured and modeled in CAD. Utilizing CAD, the ebeam gun mounting holes and feedthrough locations were determined. There were five feedthroughs consisting of the ebeam gun's water cooling lines, deposition shutter, rotating crucible gear assembly, high voltage and sweep control electrical. Once 3D CAD of the mounting plate was created a 2D drawing was created and the mounting plate was machined. Custom feedthroughs for the deposition shutter and rotating crucible gear assembly were designed and assembled. The mounting plate, the ebeam gun and feedthroughs were then installed into the chamber.

Next, the ebeam high voltage power supply, transformer and electrical lines were installed along with the quartz crystal monitor components. A single chiller would supply cooling to the cryo pump compressor, ebeam gun and quartz crystal. The chiller's supply and return water lines were constructed of Swagelok tubing and rubber hose. The water flow rate requirements of each of the three components differed and were individually calibrated using check valves. Once the waterlines were completed the ebeam system had a successful startup and began producing high quality films. Fig. 5.13 shows the completed assembly of the deposition system. The ebeam was manufactured by MDC and consisted of a 3kW Mighty Source 4 pocket x 2cc rotary electron beam source which is 2.4-inches tall by 4-inches long by 2.8-inches wide. The ebeam was powered by a MDC 6kW power supply and the deposition was controlled by a MDC Source Control Module and XY Programmable Sweep Controller. The film

thickness was controlled by an Inficon SQC-310 Series deposition controller and quartz crystal sensor.

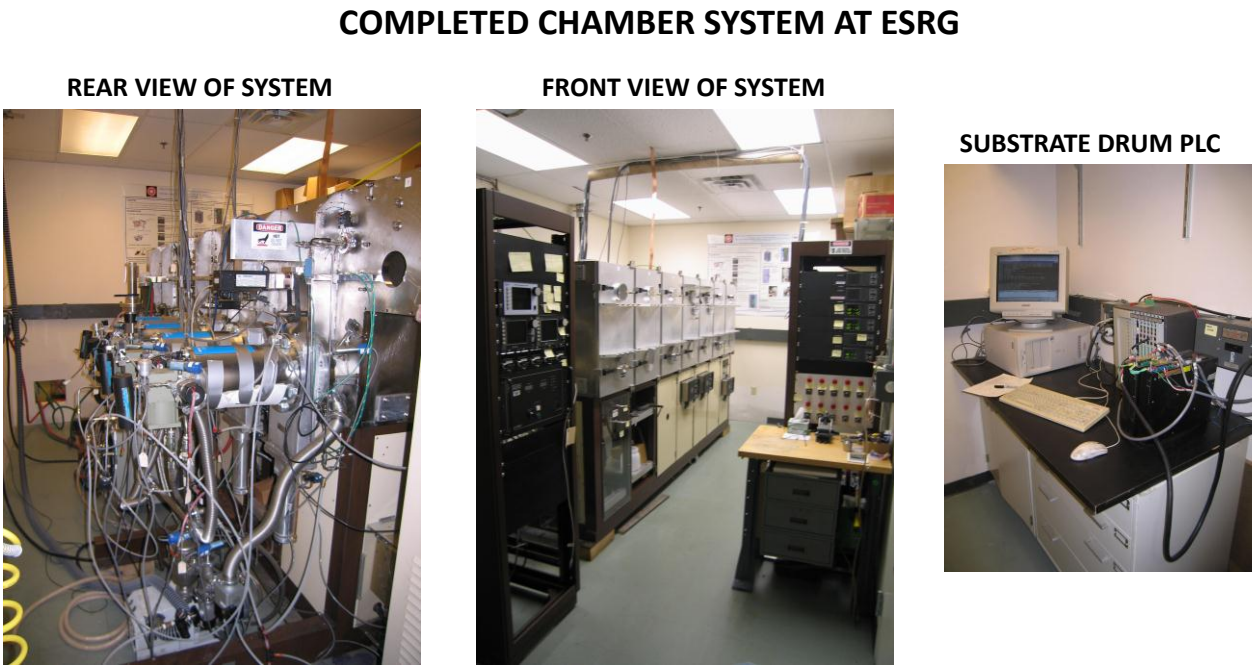

Figure 5.13: Picture of the completed ebeam deposition system

The chamber system operational readiness was validated through the conformation of producing specific selections of thin film materials. These materials included titanium, lithium fluoride, iron fluoride. The materials were selected based on their familiarity to the lab (being PVD film materials that the lab has produced in the past) and their applicability to the research goals of this thesis.

The vaccum chamber achieved an initial base pressure of 1x10^-7Torr before feedthroughs were added which then raised the base pressure to $5x10^{-7}$Torr that required 8 hours of overnight pumping. To save pump down time the depositions for the experiments were conducted at $3x10^{-6}$Torr. The chamber took 2.5 hours to achieve

this pressure level and consisted of pumping for 1.5 hours with a Leybold D16B Trivac Rotary Vane Dual Stage Mechanical Vacuum Pump until the pressure reached to $1x10^{-3}$Torr and then 1 hour of high vacuum pumping with the two CTI-Cryogenics-8 cryo pumps. The rate of rise (ROR) of the chamber when the cryo pumps gates were closed at an initial chamber pressure of $3x10^{-6}$Torr was 2.5Torr over 2 minutes then stabilized to less than 50millTorr per hour.

Titanium was selected for the first thin film material to validate due to its stable deposition evaporation rate, high melt temperature, solid pellet source form and the extensive PVD experience the lab has with producing films of this material. The first step in validating the system was to calibrate the quartz crystal thickness monitor (QCM) and determine a tooling factor for titanium. The source material of titanium was of pellet form and placed into a 2cc graphite crucible. To calibrate the QCM, titanium was deposited on a substrate consisting of three glass slides (1”x3” each) that were placed ten inches from the source. During the deposition the ebeam current was set at 100mA and a voltage of 5kV which produced a QCM reading of 2 angstroms per second (A°/sec). The vacuum pressure was $3x10^{-6}$Torr before the deposition, then the pressure rose to $8x10^{-6}$Torr for the first 5 minutes of the deposition and then stabilized back to $3x10^{-6}$Torr for the remaining duration. Since the crystal of the QCM was located eighteen inches from the source (ebeam) and the substrate nine inches from the source (ebeam), the deposition readings of the QCM were underestimating the rate. To determine a tooling factor for the QCM four independent depositions were completed and the thickness of the film on the glass slides was measured between each deposition. The thickness of the film was measured using a Dektak 150 stylus surface

profiler. Taking the actual measured thickness of the film and dividing it by the QCM thickness reading determined the tooling factor for titanium. The tooling factor for titanium was calculated to be approximately 4.0. By multiplying the tooling factor by the QCM deposition rate of 2A°/sec it was determined that the actual deposition rate during the first four depositions was approximately 8 A°/sec. This identical QCM calibration procedure would be needed for each new material that the system deposited in order to have an accurate understanding of the real time QCM readings. The second step of the validating the system was to center the electron beam with the center of the source crucible. With the initial depositions set at 5.0kV and inspecting the solidified previously melted source material in the crucible the beam alignment was determined. A visual inspection of the solidified source for a concaved region indicated the contact position of the beam. Over the next three depositions, the voltage was adjusted to 4.6kV, 4.8kV and 4.75kV respectively to align the electron beam with the crucible center. Once the electron beam was initially centered it would not require centering with new source materials and would be set at 4.75kV moving forward. Fig. 5.14 shows the Dektak profiler thickness results of the first titanium deposition with 4.75kV and the electron beam centered.

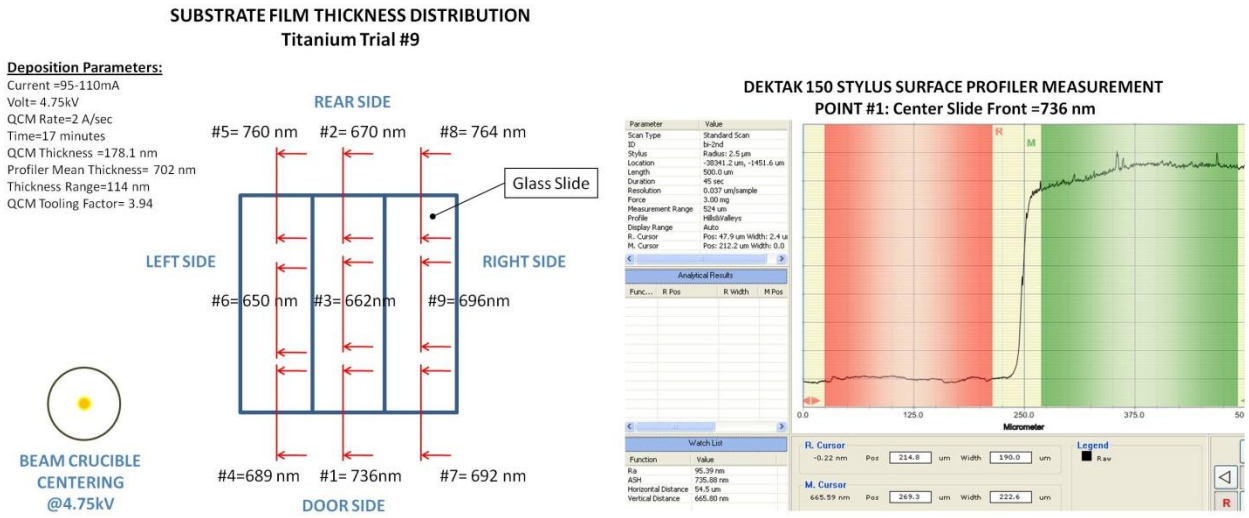

Figure 5.14: Results of a titanium deposition showing substrate thickness distribution

The third step of system validation process was to begin to understand the glancing angle deposition (GLAD) capabilities. The next depositions would focus on static glancing angle depositions at substrate angles of 35°, 55° and 75°. The substrate consisting of three glass slides were mounted on the substrate holder and drum. Using the programmable logic controlled servo motor the substrate drum was rotated into the required glancing angle. The position of the substrate in the chamber can be seen in Fig. 5.15.

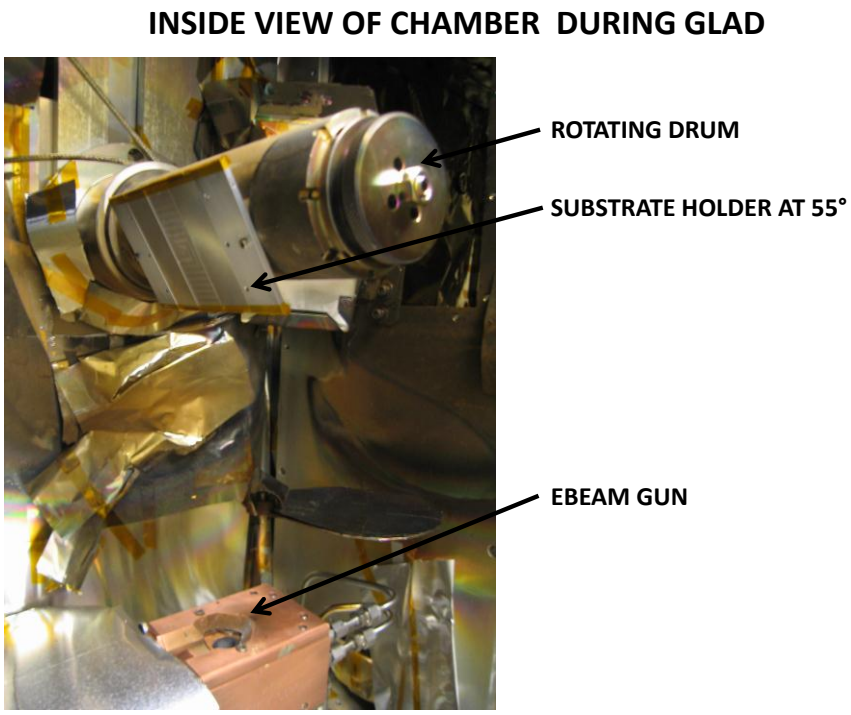

Figure 5.15: View of chamber with the substrate drum rotated in GLAD position

Once the deposition was completed the films were placed in a Joule IB-09010CP ion beam cross section polisher pictured in Fig. 5.16 to render defect free cross sections for FESEM imaging. Ion beam polishing can avoid the scratches, delamination and other damages from the applied forces of conventional mechanical polishing or cutting technique and is a stress free process which employees an argon ion beam to remove material from the sample. An ion beam resistant mask is placed on half of the sample surface to block half of the beam while the other half of the ion beam gradually removes the sample material protruding from the mask producing a straight cross section with a clearly defined edge. The samples are mounted on a SEM sample mounting block during the cutting process for ease of transfer into the SEM for imaging. The samples for the experiments were polished with an ion accelerating voltage of 3.5kV for 2 hours

producing a cross sectioned length of approximately 3mm. Fig. 5.17 shows the FESEM images of the titanium film deposited at 55° which was cross section polished and clearly shows the angular growth of the Ti film relative to the substrate.

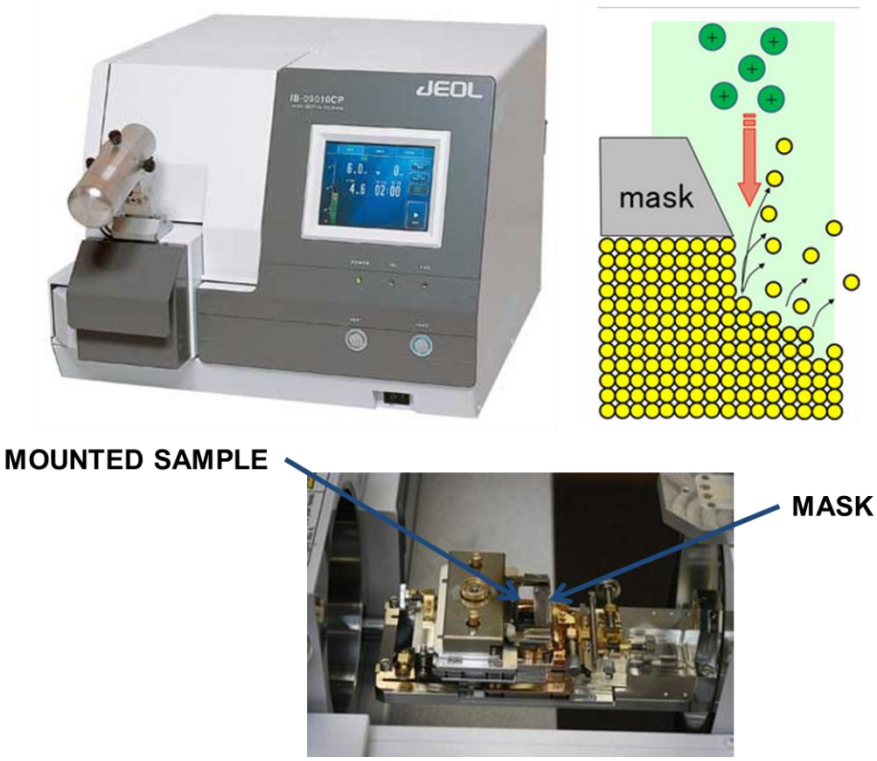

Figure 5.16: Joule cross section polisher

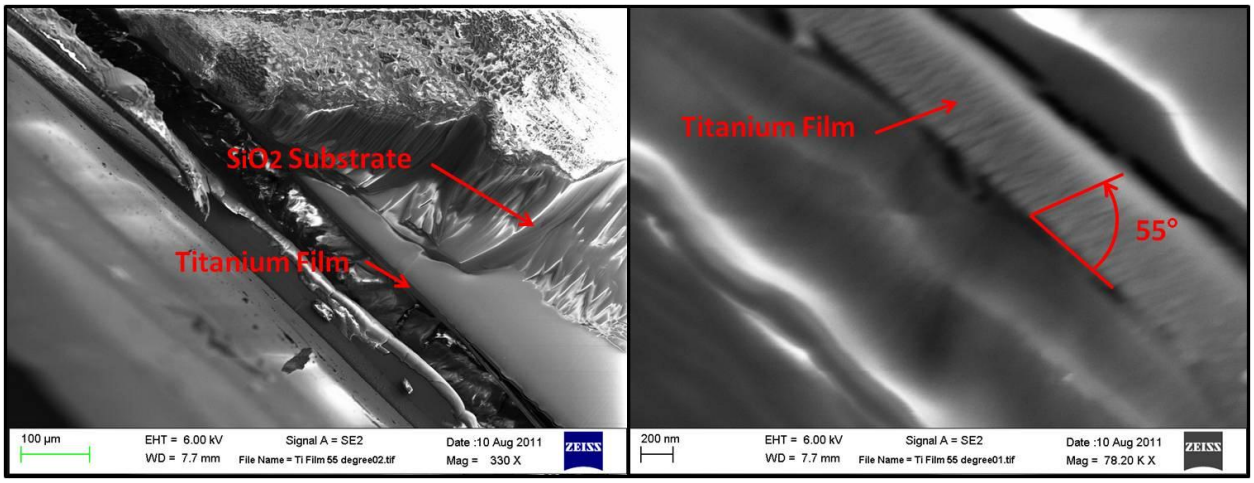

Figure 5.17: FESEM images of a titanium 55° GLAD film deposited with the substrate held at a 55° angle relative to horizontal base of the ebeam.

The validation of the next material to be processed with the ebeam system was iron fluoride. The iron fluoride source material was powder form and placed directly into a 2cc graphite crucible. The XRD scans in Fig. 5.18 confirm the successful thin film deposition of single phase FeF_2 by comparing it to the initial powder.

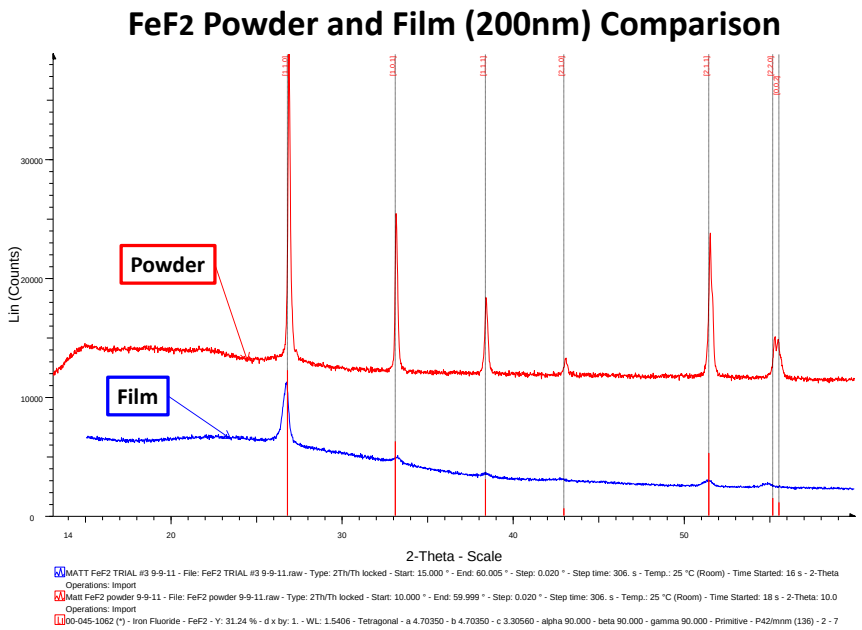

Figure 5.18: XRD results confirming single phase synthesis of FeF_2 thin film

When depositing iron fluoride (FeF_2) on Al-7075 substrates, the addition of the titanium adhesion layer affected the preferred orientation growth of FeF_2. Figure 5.19 shows XRD scans of the FeF_2 film with and without a 50nm titanium adhesion layer. The FeF_2 film with the adhesion layer showed a more preferred (110) orientation then the film without the adhesion layer. This preferred crystallographic orientation aligned with one particular lattice plane is a common phenomenon in polycrystalline films. Generally, the film is preferentially oriented parallel to the substrate and often the degree of preferred orientation increases with increasing thickness. Orientation of the film is dependent on crystal structure. If the film material is face centered cubic (FCC) structures then typically it has a [111] texture, body centered cubic (BCC) structures then typically it has a [110] texture and diamond structures exhibit a [110] or [100] texture depending on the deposition temperature. However, dependence of texture on

crystal structure is not assumed and different mechanisms can produce or modify texture. These mechanisms include the substrate temperature, pressure during the deposition, crystallographic orientation of the substrate, deposition rate and in addition, texturing can be caused by the tendency to minimize volume strain energy in thicker films and minimize the surface energy in very thin films. [31,78,79,80,81,82] Considering that these FeF_2 films with and without the titanium adhesion layer were deposited with the same thickness and process parameters, it is likely that the texturing was produced from the crystallographic orientation differences between the aluminum (FCC) and titanium (HCP).

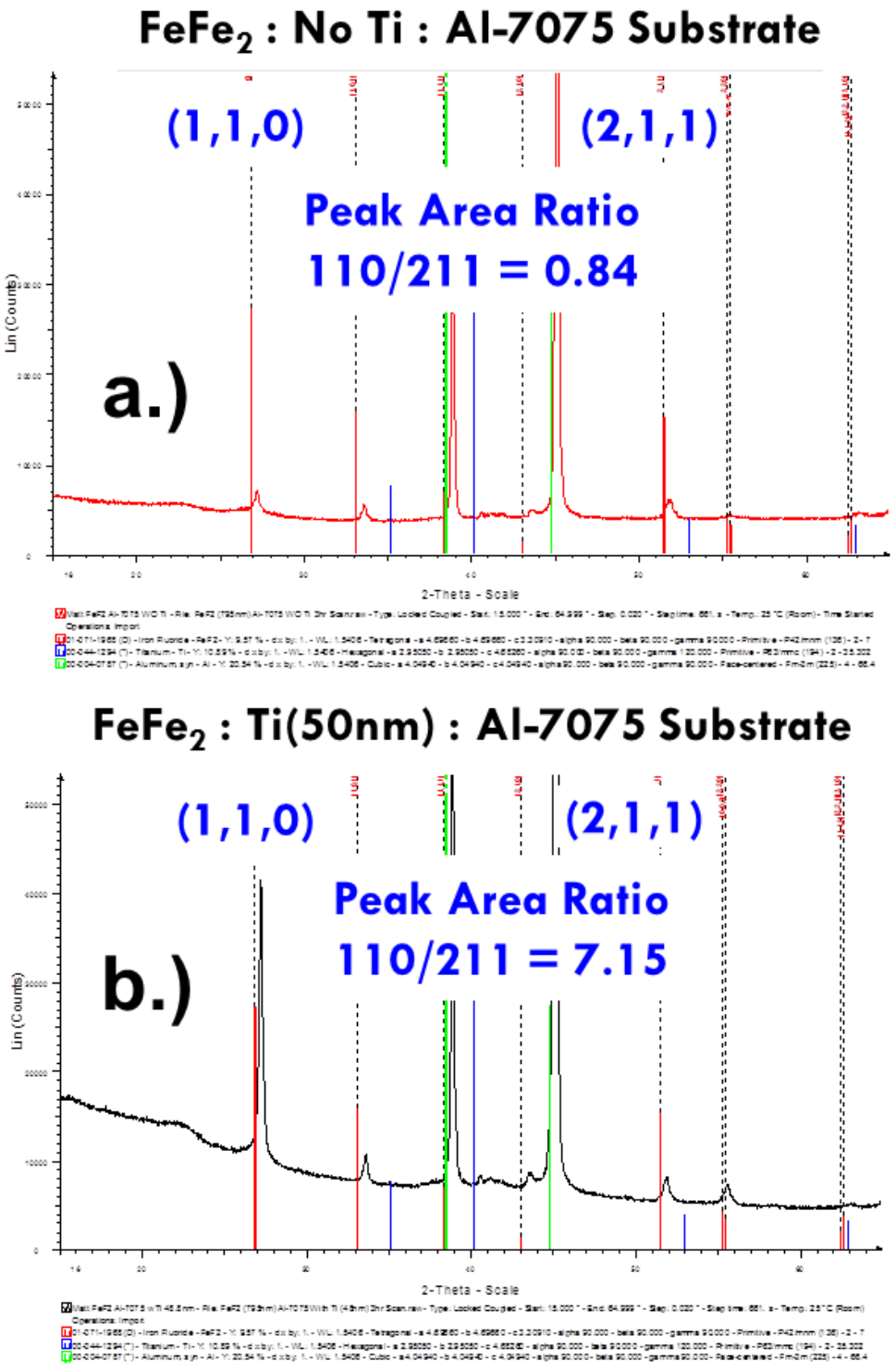

Figure 5.19: XRD results of FeF_2 a.) without Ti adhesion layer and b.) with Ti layer

6 Effect of Vertically Structured Porosity on Electrochemical Performance of FeF_2 Films

6.1 Introduction

There is an increasing demand for high capacity power sources in applications of portable electronics and large scale mobile devices such as electric vehicles. However, commercial lithium batteries typically use intercalation cathode compounds (e.g., $LiFePO_4$, $LiCoO_2$) which have moderate energy density and do not meet the growing demand for higher energy technology. While intercalation materials offer desirable properties such as good cycling life, good rate capability, and high discharge voltages, they are restricted at most to a single electron transfer per formula unit. This restriction limits the energy density that can be achieved with current insertion materials.

In order to achieve higher specific capacity, an alternative process known as conversion reaction has been studied for decades as electrodes for primary batteries but only more recently for secondary.[83-87] In conversion reactions, larger theoretical energy densities are possible because this reaction can utilize all energetically favorable oxidation states of the metal cation that comprises the cathode. As a result, more than one electron transfer occurs per transition metal (TM) cation during the redox cycle. Although, reversible conversion reactions have been demonstrated with a variety of materials including metal sulfides[88,89], oxides[90,91,92], fluorides[93,94], nitrides[95,96] and phosphides[97,98] only metal fluorides have a high enough reaction potential to be used as Li-ion cathodes. This is due to the very ionic nature of the metal fluoride bond.

Despite metal fluorides represent a route for high energy density positive electrodes they are limited by their wide band gap corresponding in electronically

insulating behavior and very poor ionic diffusion through the conversion front. Transport is greatly enhanced by the use of carbon or mixed conducting matrices in combination with metal fluoride domains <30nm. This approach has enabled the electrochemical activity of a wide variety of metal fluorides.[99] Despite the improvements, conversion reaction mechanisms are not well understood and the opportunity to commercialize these electrodes is obstructed by cycling performance issues most notably cycling retention and reversibility.

This study investigates the conversion cathode material iron fluoride (FeF_2) to further understand conversion reaction mechanisms. FeF_2 has a rutile tetragonal structure and is an attractive material for use as nanocomposite cathodes due to its exceptionally high specific theoretical capacity of 571mAh/g. In addition, the rutile difluoride is ubiquitous among the other first row transition metal fluorides such as NiF_2 and CoF_2 which are also of interest for electrochemical applications. During the reaction FeF_2 + Li+ combine to form nanocrystalline LiF crystals and Fe^0 clusters which is represented in eq 1.

$$FeF_2 + 2Li \leftrightarrow 2LiF + Fe \qquad (1)$$

This study uses a combination of dense and highly structured thin films to (a) elucidate the relative contributions of the ionic and electronic transport processes in the rate and cycling limitations of the electrochemical cell, (b) the effect of the electrode structure to absorb the 16.7% electrode expansion on cycling through the reaction.

Almost all reports on metal fluorides as electrode materials have shown a systematic requirement for the metal fluoride crystallite or thin films to be of nanodimensions in

order to have effective utilization approaching the theoretical capacity. However, despite this restriction, no one has unequivocally proved whether this limitation was of ionic or electronic in origin. In order to study this phenomenon we have constructed two contrasting film structures as a function of thickness. These are depicted in Fig. 6.1. The first film structure is of a dense classical thin film deposition shown in Fig.6.1a. In this case, ions from the electrolyte react with the top surface. For the reaction to proceed, it is required that an electron is conducted from the substrate through the film to the surface for the conversion reaction to progress. A limitation in the as formed FeF_2 electronic conductivity would be inhibiting to the reaction initiating and progressing. The contrasting case is depicted in Fig. 6.1b where pore structures would progress from the surface of the film to the substrate. In this case there is excellent ionic contact with a majority of the film bulk, and close to the substrate/film interface. An initiation point of the reaction could proceed at or near the substrate-film-electrolyte triple point interface. It has been shown that the electronic conductivity of converted fluoride films may be significant due to the formation of a percolated network of iron particles.[100] This has been substantiated by electronic conductivity measurements.[101] If this is the case, a fast surface reaction can then proceed up the walls of the film's pores and to the surface. In short, once the reaction is initiated there is no electronic barrier to further progression. Any further limitation would be due solely to the ionic component. If the electronic conductivity is not great enough to support the reaction the reaction progress will cease.

The past decades have resulted in a number of new insights on effective morphology controlled by variations in the static and dynamic substrate positioning.[102,103] For this study, a novel thin film deposition system was developed to produce consistent thin

films of a wide range of thicknesses with unique morphologies which can influence the film's interfacial surface area. The system was based on a physical vapor deposition technique called glancing angle deposition (GLAD) where the morphology of the film growth can be controlled through substrate rotational positioning at defined oblique angles to the deposition source.

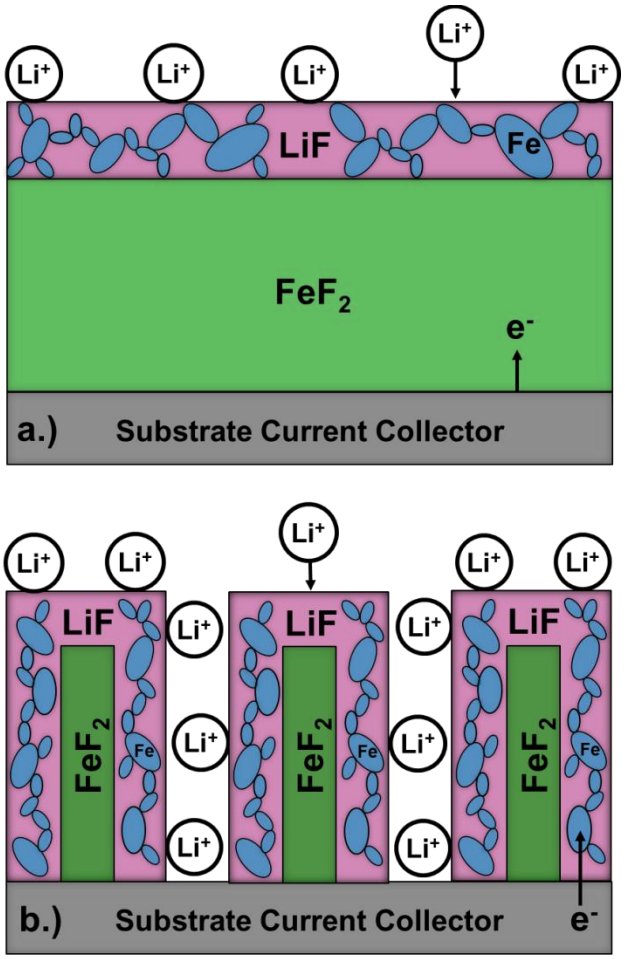

Figure 6.1: Lithiated film structures (a) classical static film and (b) porous dynamic film

In past literature electrochemistry studies using FeF_2 thin film electrodes, the maximum film thickness was less than 150nm due to the limiting insulating characteristic property of FeF_2.[104] In contrast, this study uses films with thicknesses of 850nm produced by the

GLAD concept which show improved electrochemical performance relative to classical statically produced thinner films.

6.2 Experimental

6.2.1 Material Synthesis

The thin films were prepared in a custom fabricated high vacuum electron beam evaporation chamber. The electron beam evaporator consisted of a MDC 3kW Mighty Source with four 2cc rotating crucibles. The substrate was mounted approximately 23cm from the e-beam source onto a 76mm diameter drum 178mm in length that is positional through a programmable logic controlled servo motor (Ormec).

Prior to the deposition the substrate was prepared using unpolished high-strength aluminium alloy 7075 (McMaster-Carr) with a thickness of 0.8mm. The Al-7075 substrate was cut into a 25mm x 75mm strip with the grains running parallel to the width of the strip. The Al-7075 strip was cleaned with acetone then methanol and placed in the center of a flat substrate holding plate along with two cleaned glass microscope slides 25mm x 75mm with a thickness of 1mm. The glass slides were laid flat and place on each side of the Al-7075 strip and the three pieces were secured to the substrate holding plate using Kapton® tape. The glass slides were later used to measure film thickness.

The source material of approximately 5g total of FeF_2 powder (Advanced Research Chemicals) was packed tightly into three of the four 2cc graphite crucible liners. The fourth crucible liner was loaded with titanium (99.99% Ti granules, Alfa). The substrate holder containing the Al-7075 substrate and glass slides was bolted to the 76mm diameter programmable drum with the length of the strips running parallel to the

length of the drum. The vacuum chamber was then brought to a pressure of $3x10^{-6}$ Torr.

To provide an adhesion layer for the FeF_2, 50nm of titanium was first deposited onto the substrate in the Static 0° angle position. During the deposition of titanium a voltage of 4.8kV with a current of 80mA were applied and the deposition rate was approximately 10A°/sec. Next, FeF_2 was deposited with a voltage of 4.8kV with a current of 5mA and the deposition rate was approximately 13A°/sec. Once the deposition was completed, the chamber was vented with a combination of nitrogen then dry air. The films were removed from chamber and then stored in a helium filled glovebox (<0.6 ppm H_2O, <0.1 ppm O_2) until coin cell fabrication and characterization trials. Prior to cell fabrication and in room atmosphere, 14.3mm discs were punched from the film to create electrodes.

Fig. 6.2 shows schematics comparing the static verse dynamic depositions. For the static deposition, the substrate holder was bolted to the drum in an orientation that was parallel to the base of the chamber which was referenced to be a 0° angle. During the static deposition, the substrate position was held constant at a 0° angle. The dynamic deposition consisted of rotating the programmable substrate drum at various angles and rotations per minute (rpm) depending on the specific deposition. For example, during the 48°-52° deposition the 50nm titanium adhesion layer was first deposited statically at a 0° angle. Second, the substrate was rotated counter clockwise (CCW) to an angle of 48° prior to depositing FeF_2. Third, the FeF_2 deposition evaporation flux was started. Next, the program rotated the substrate drum in the following sequence; CCW at 0.65rpm through 48° to 52°, CCW at 26rpm through 52° to

-52° (256°), CCW at 0.65rpm through -52° to -48°, CW at 0.65rpm through -48° to -52°, CW at 26RPMs through -52° to 52° (256°), CW at 0.65rpm through 52° to 48°. The drum was programmed to repeat this rotation sequence throughout the deposition of FeF_2. For this study, films were produced dynamically in a series of substrate angles; 28-32°(600nm), 38-42°(680nm), 48-52°(400nm,700nm and 850nm), 58-62°(525nm) and 68-72°(425nm) which tailored specific percentages of porosity into the film. These films were then compared to films that were produced statically at 0°(400nm, 700nm and 850nm).

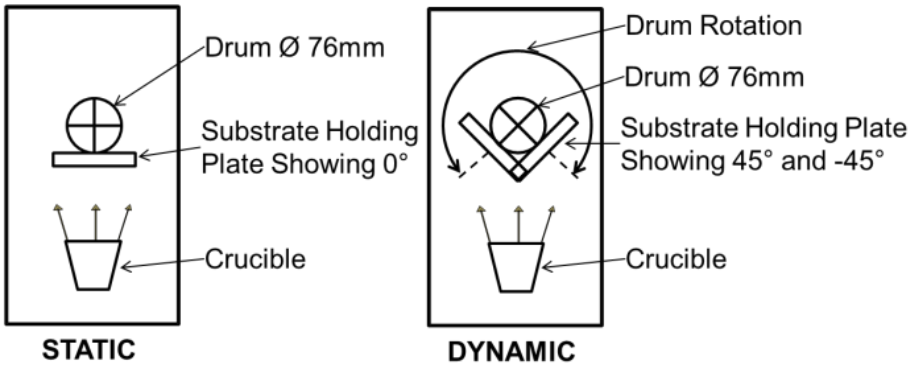

Figure 6.2: Schematic comparing static verse dynamic deposition

6.2.2 Physical Characterization

The thickness of the film was analysed using a stylus profilometer (Dektak 150) in room atmosphere. Two microscope glass slides substrates were used to measure the thickness of the Ti (50nm to aid in adhesion) and FeF_2 layered film. The glass slide allowed for a smoother surface to reference as zero thickness then the alloy Al-7075 substrate which had a surface roughness of Ra=0.3 micron. The FeF_2 film with the Ti

adhesion layer on the glass substrates were measured in four locations and an average thickness was calculated. The average film thickness was then subtracted by 50nm, the titanium adhesion layer, to determine the FeF_2 film thickness.

X-ray Diffraction (XRD) (Bruker) using CuKα radiation was performed to the films to understand the crystallographic orientation. A dedicated 10mm x 10mm piece of film was used for the XRD analysis in room atmosphere. The crystallite size was derived by the Scherrer method. XRD data was processed through the use of Topas software .

FeF_2 films were analyzed with a Field Emission Scanning Electron Microscopy (FESEM) (Zeiss). The films were exposed for approximately 2 minutes to room air while being mounted in the FESEM.

Image-J, an imaging processing and analysis Java based software (National Institute of Health, USA) was used to modify the FESEM images into binary images to calculate the canyon facial porosity percentage and the perimeter length of each canyon. The facial porosity percentage results were used to correct the mass of the film for electrochemical characterization.

6.1.3 Electrochemical Characterization

All batteries fabricated for studies in this paper were fabricated in aluminized (on the positive electrode) 2032 coin cells (Hosen) made with cathodes consisting of a 14.3 mm diameter disc of iron fluoride film on Al-7075 substrate, two layers of borosilicate glass fiber separator (Whatman) with a diameter of 15.9 mm soaked with electrolyte, and a 0.3mm thick 12.7mm diameter lithium metal foil as the anode counter electrode (half-cell) (FMC). The electrolyte was 1 M $LiPF_6$ EC: DMC (Novolyte), stored in a helium filled glovebox and used without additional treatment. Galvanostatic cycling tests were

performed in a dry room on a MacPile II (Biologic). The cells were cycled galvanostatically between 4.50 V and 1.00 V at a constant current of 12.5 mA g-1 in an oven set at 60^{o}C.

6.3 Results

6.3.1 Crystallography

XRD was performed on the films to understand the effect of deposition conditions, on crystallographic orientation, crystallite size and lattice parameters. The films were scanned over the 2θ ranges of 20-37° and 48-65° to avoid the intense reflection from the Al substrate. Fig. 6.3a shows the scans of FeF_2 films produced dynamically in a series of substrate angles, 28-32°(600nm), 38-42°(680nm), 58-62°(525nm) and 68-72°(425nm). Fig. 6.3b shows the scans of films produced dynamically at a substrate angle of 48-52° and systematically increased thicknesses of 400nm, 700nm and 850nm. Fig. 6.3c shows the scans of the films produced statically at a substrate angle of 0° with similar thicknesses to those obtained dynamically at 48-52°. Diffraction reveals that all films are composed of single crystalline phase FeF_2 of rutile structure with the exception of the film obtained dynamically at the substrate angle of 68-72° scan that revealed very poor crystallization. Lattice parameters in Table 1 are fairly consistent with ICDD values of a=4.70Å and c=3.31Å showing some compression in the c parameter.

Molecular dynamics simulations have previously shown that the Li^{+} diffusion barrier along the [110] channel is approximately 70% greater than the barrier along the [001] channel.[105] To understand if the films had preferred crystallographic orientation.

that could directly impact electrochemical performance, the integrated intensity ratios of the (110) and (211) reflections were calculated and summarized in Table 1. The (110)/(211) peak area ratios show dependence on the deposition angle. The (110)/(211) ratio was found to decrease as the thickness increased. As reference, the calculated peak area ratio for the macroscopic phase pure FeF_2 powder was 2.44 suggesting texturing in the preferred <110> for the films. It is important to note that the (110) and (211) peak area ratio is drastically increased with the titanium adhesion layer verse without. All films used in this study comprised a titanium adhesion layer.

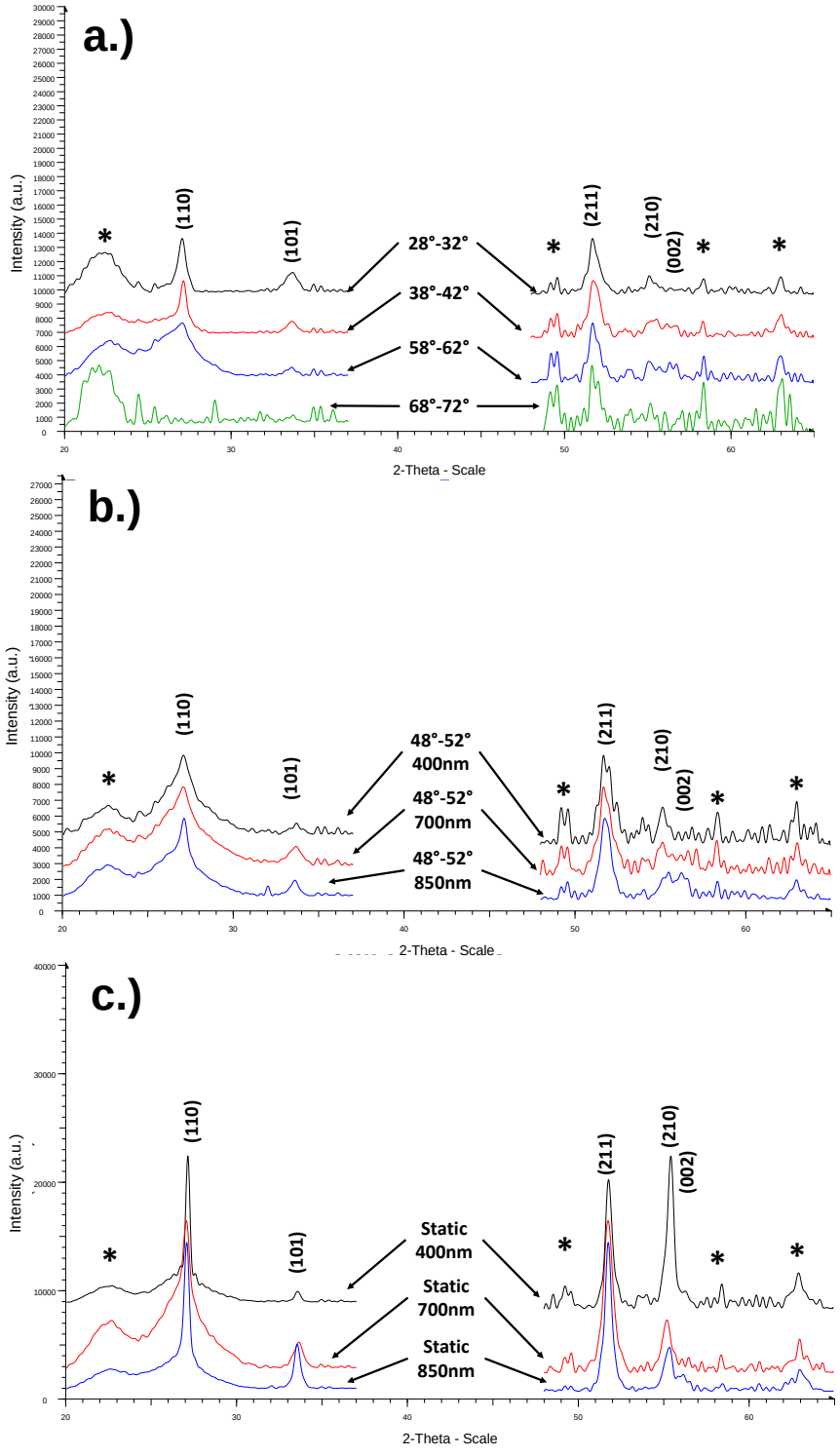

Fig**ure 6.3:** XRD results (a) dynamic angular films (b) 48-52° dynamic films and (c) static films. Substrate reflections are represented by *. Note: larger angle range intensity was magnified for clarity of presentation.

Film	Thickness (nm)	Lattice Parameter (a, c)	Crystallite Size (nm) (110, 211)	110/211 Peak Area Ratio
Static	400	4.7(2), 3.2(7)	31.8, 20.5	7.16
Static	700	4.7(1), 3.2(7)	12.5, 15.2	4.73
Static	850	4.7(3), 3.2(7)	20.2, 20.9	4.42
28°-32°	600	4.7(0), 3.2(6)	11.0, 13.9	3.22
38°-42°	680	4.7(0), 3.2(8)	8.2, 9.7	5.49
48°-52°	400	4.7(2), 3.2(5)	8.1, 11.8	5.23
48°-52°	700	4.7(3), 3.2(6)	8.8, 15.1	5.24
48°-52°	850	4.7(2), 3.2(7)	12.9, 14.7	4.18
58°-62°	525	4.7(1), 3.2(6)	8.1, 19.2	11.03
68°-72°	425	4.7(2), 3.2(5)	NA, 9.6	NA

Table 2: Summary of XRD Analysis

6.3.2 Physical Characterization

The static and dynamic rocking thin film electrodes were analysed with FESEM. Fig. 6.4 shows the static films with a.), c.) and e.) being the 400nm, 700nm and 850nm films respectively at 2kX magnification. In Fig. 6.4 the static films in b.), d.) and f.) are the 400nm, 700nm and 850nm films respectively at 35kX magnification. For the static films, the images show a dense non porous morphology regardless of thickness. The grains of the Al-7075 substrate can be observed textured through the FeF_2 film.

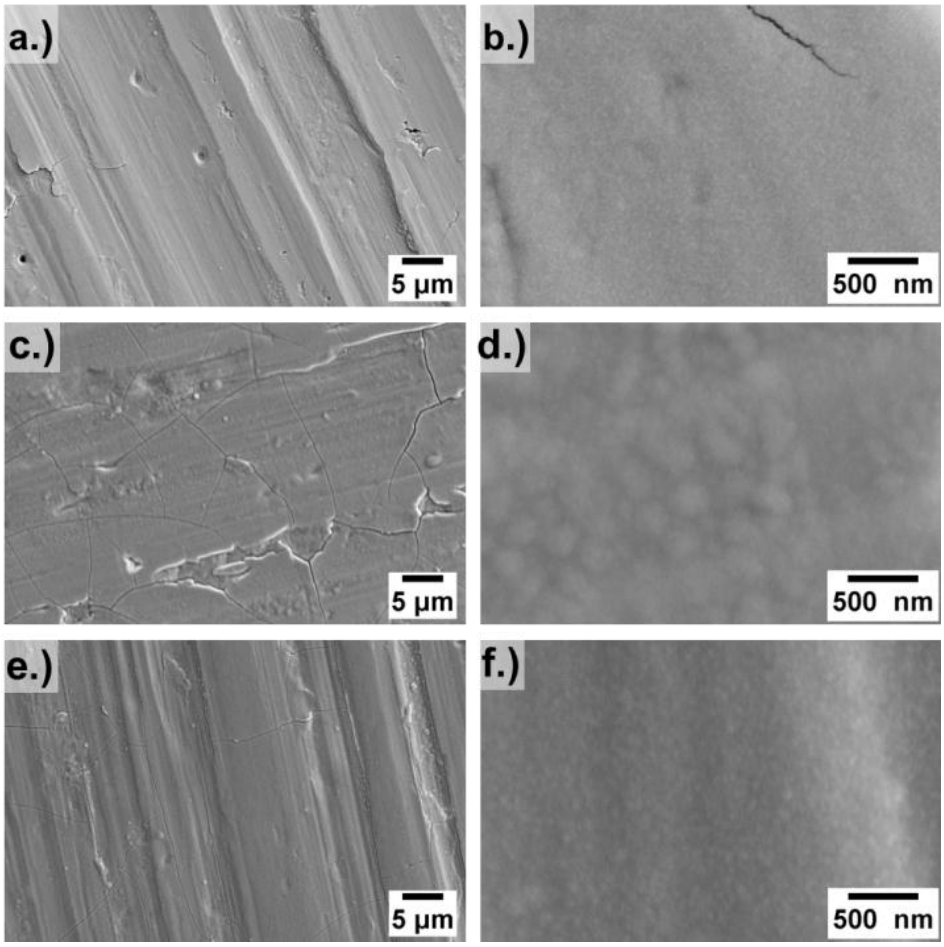

Figure 6.4: FESEM images of Static 400nm (a) 2kX (b) 35kX, Static 700nm (c) 2kX (d) 35kX, and Static 850nm (e) 2kX (f) 35kX

Fig. 6.5 a.), c.), e.), g.) and i.) show the images of the 28-32°, 38-42°, 48-52°, 58-62° and 68-72° respectively at 2kX magnification. In sharp contrast to films deposited in the static mode, these films generate morphology reminiscent of porous canyons. The spacing between the individual porous canyons and the width of the film area is dependent on the angle in which the film was deposited and decreases with increasing deposition angle. For example, when the film is deposited at 28-32° the porous canyons have the greatest spacing (least porosity) and the 68-72° film as the least

spacing (greatest porosity). This can be observed in more detail in Fig. 6.5 b.), d.), f.), h.) and j.) which show the images of the 28-32°, 38-42°, 48-52°, 58-62° and 68-72° respectively at 35kX magnification. These images reconfirm the morphology of the film is one of porous canyons that have a tiger stripe like appearance when viewed perpendicular from the face of the surface. The width of the pore ranges from approximately 50-150nm depending on the deposition angle in which the film was produced.

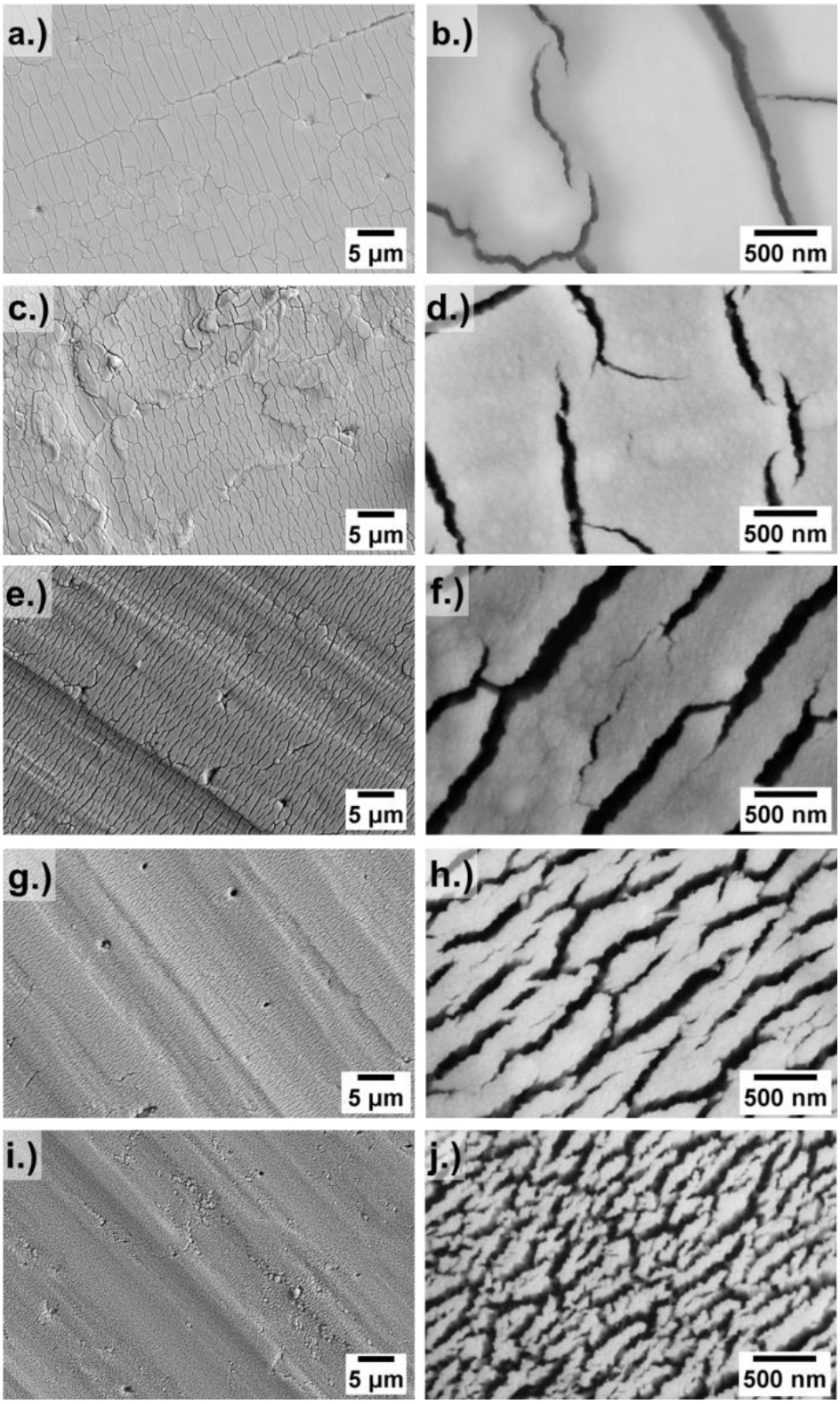

Figure 6.5: FESEM images of 0.65rpm 28°-32°(a) 2kX (b) 35kX, 38°-42°(c) 2kX (d) 35kX, 48°-52°(e) 2kX (f) 35kX, 58°-62°(g) 2kX (h) 35kX and 68°-72°(i) 2kX (j) 35kX

Fig. 6.6 shows images of the 48-52° film at a thickness of 400nm and 850nm. The subsequent micrographs at 2kX and 35kX magnification show that the pore width is additionally dependent on film thickness. It is observed that as the film thickness increases, the spacing between the pores increases along with the porous canyon width. The pore width of the 400nm film was approximately 50-100nm and the 850nm film was approximately 75-150nm.

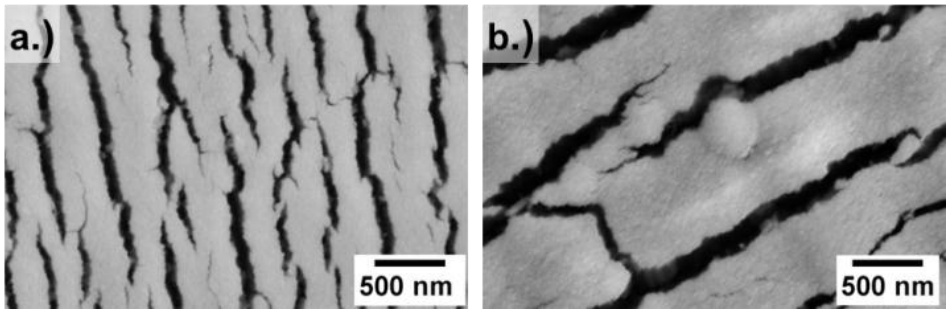

Figure 6.6: FESEM images of 0.65rpm 48°-52° at 35kX (a) 400nm and (b) 850nm

From Fig. 6.5 the grain direction of the Al-7075 substrate can be observed. The directionality of the porous canyons is shown to be perpendicular to the substrate grain and hence parallel to the axis of rotation. Since the substrate is consistently orientated so that the substrate grains are perpendicular to axis of rotation it can be understood that the direction of the porosity is parallel to the axis of rotation. The parallel relationship to the axis of rotation would suggest that the morphology is formed by a glancing angle deposition (GLAD) shadow effect. As discussed earlier, it can be observed that the porosity of the thin film electrode increases as a function of increasing

substrate deposition angle. This angular dependence of the porosity is indicative of traditional glancing angle deposition.

To further understand how the morphology is dependent on the rotation velocity and angle positioning of the substrate, additional dynamic rocking depositions and their respective FESEM images were completed. Fig. 6.7a, 6.7b and 6.7c show images of a 60°-80°, 40°-60° and 40°-80° films respectively. These films were rotated in the same method that was previously explained in Fig. 6.2 and similar to the films produced at 0.65rpms and shown in Fig. 6.5 and Fig. 6.6. However, these films were rotated at a velocity of 6.5rpm (replacing the 0.65rpm of the films previously discussed) through these concentrated angles and then rotated at 26rpm through all other angles. The films show a similar porosity trend as the 0.65rpm films with increasing porosity as the angle is increased.

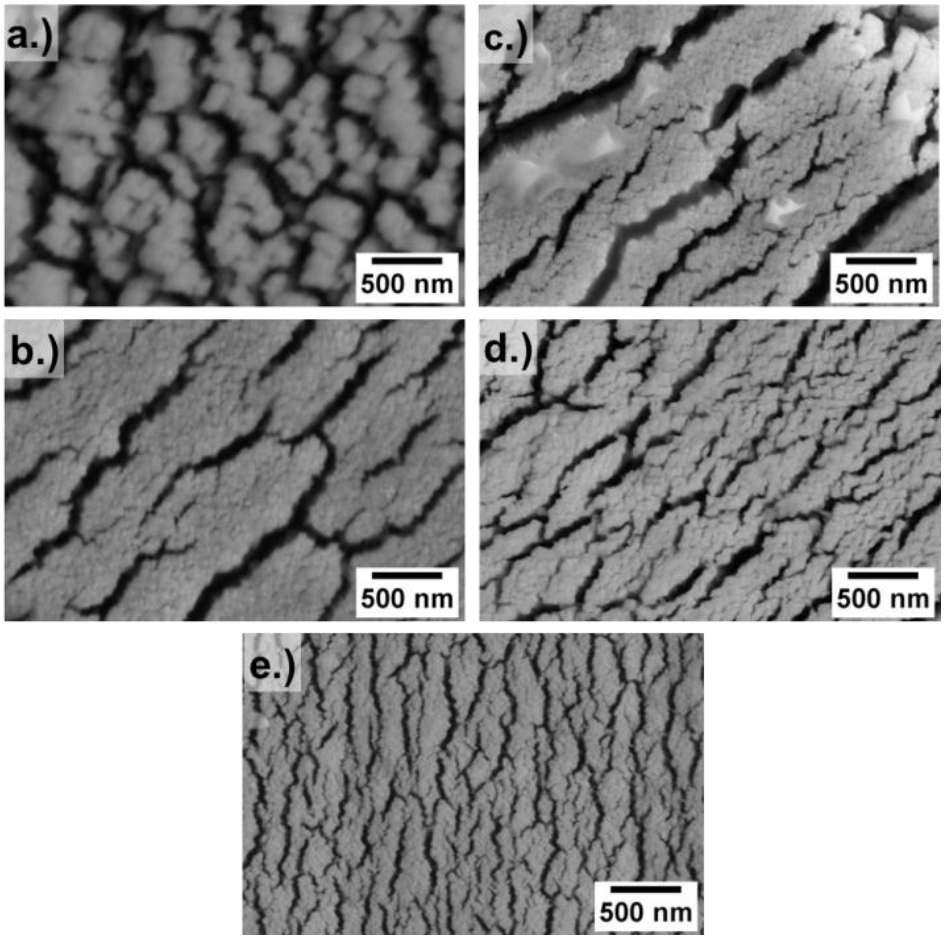

Figure 6.7: FESEM images at 35kX of (a) 60°-80° at 6.5rpm (b) 40°-60° at 6.5rpm (c) 40°-80° at 6.5rpm (d) 40°-80° at 16.25rpm and (e) 40°-80° at 26rpm

To understand the relationship between the rotation velocity and the film's morphology, 40°-80° films were produced at greater velocities of 16.25rpm and 26rpm in addition to 6.5rpm. Fig. 6.7d and 6.7e show the 16.25rpm and 26rpm films respectively. By increasing the velocity a more homogeneous morphology and refined porosity is produced. In addition, increasing the velocity produces pores with a narrower width and spacing distribution. The porosity percentages of the 40°-60°, 40°-80° and 60°-80° films rotated at 6.5rpms were 15.7%, 21.9% and 39.4% respectively.

The porosity percentage of the 40°-80° film rotated at 6.5rpm, 16.25rpm and 26rpm were 21.9%, 27.5% and 32.1% respectively suggesting that an increase in velocity systematically increases the porosity.

6.3.3 Quantitative Micro/Nanostructure

Image processing was used to calculate the canyon facial porosity percentage and the perimeter length of each canyon. The FESEM images were modified into binary images. The results of the binary images for the dynamic depositions 28-32°, 38-42°, 48-52°, 58-62° and 68-72° are shown in Fig. 6.8. The results of the binary images for the static depositions 0° (400nm, 700nm and 850nm) are shown in Fig. 6.9.

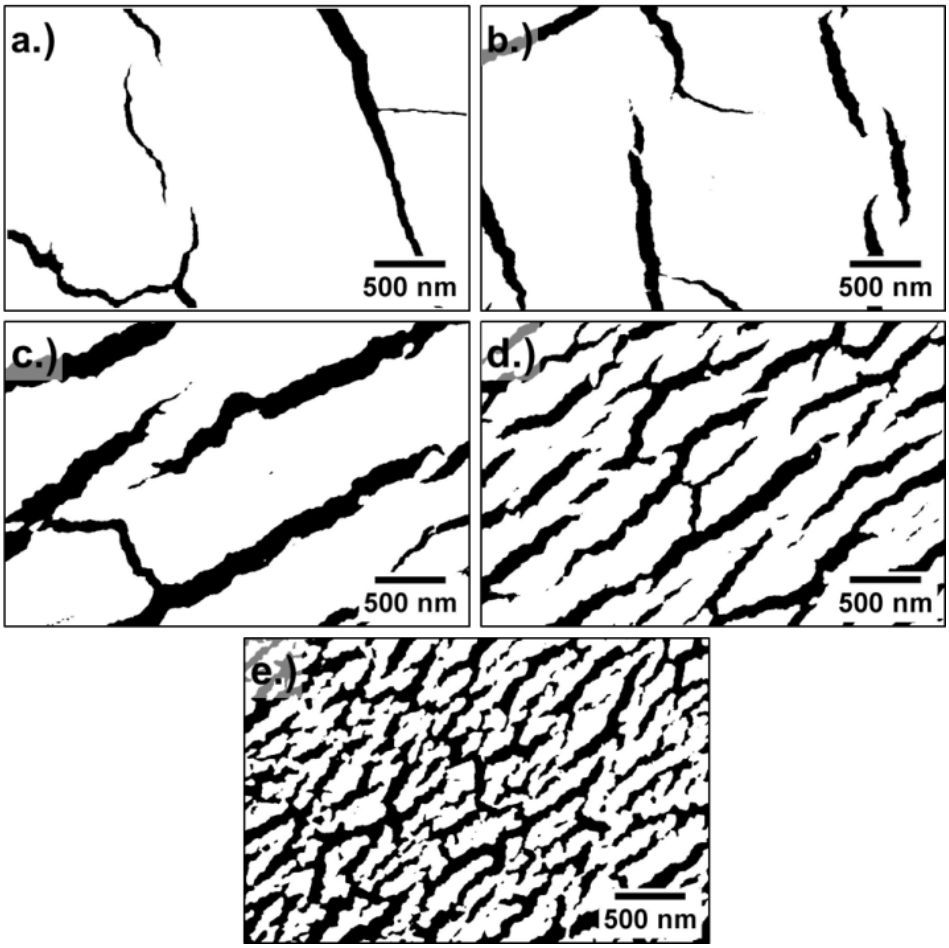

Figure 6.8: Image processing of 0.65rpm at 35kX (a) 28°-32° (5.2%), (b) 38°-42° (8.2%), (c) 48°-52° (19.9%), (d) 58°-62° (26.4%) and (e) 68°-72° (39.2%)

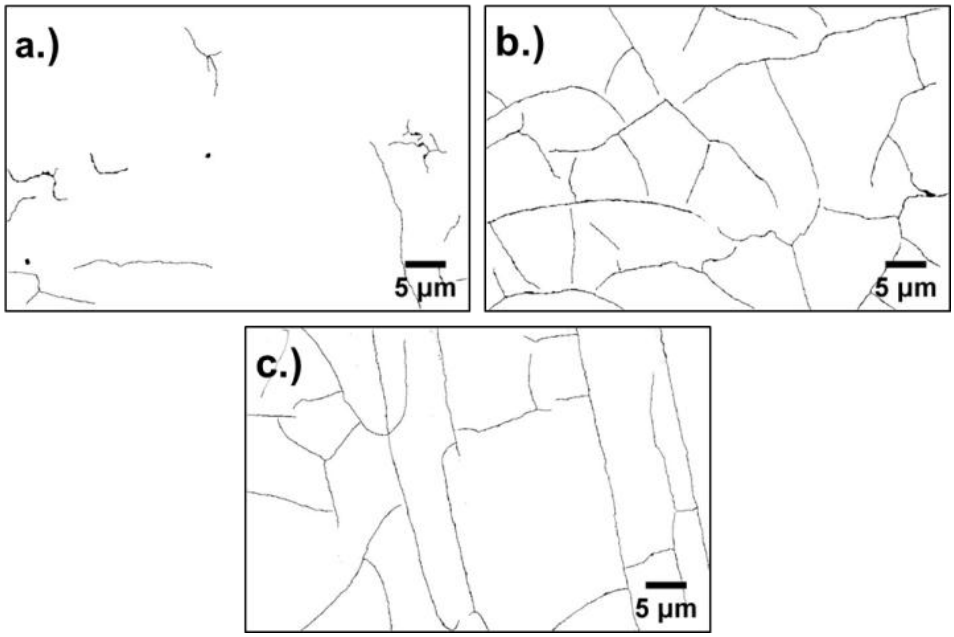

Figure 6.9: Image processing of static films at 2kX (a) 400nm (1.1%), (b) 700nm (1.9%) and (c) 850nm (1.3%)

The results of the binary images for the static depositions 0° (400nm, 700nm and 850nm) are shown in Fig. 6.9. The facial area percentages and the perimeter lengths of the dark contrast in the binary images were calculated. The dark contrast facial area percentage, which represents the percentage of porosity, was calculated to be 5.2% (28-32°), 8.2% (38-42°), 19.5% (48-52° 400nm), 18.3% (48-52° 700nm), 19.9% (48-52° 850nm), 26.4% (58-62°) and 39.2% (68-72°). These results are in sharp contrast to the porosity percentage calculated for the static 0°; 1.1% (400nm), 1.9% (700nm) and 1.3% (850nm). The perimeter length of the porosity was used to calculate the additional interfacial surface area created vertically within the canyon walls. This perimeter length was multiplied by the film thickness to determine the percentage increase in area derived from the pore wall area. The result of this calculation was 103% (28-32°), 148%

(38-42°), 243% (48-52° 400nm), 200% (48-52° 700nm), 282% (48-52° 850nm), 381% (58-62°) and 580% (68-72°). The result of the static 0° was 6% (400nm), 28% (700nm) and 30% (850nm). The facial porosity percentages and the percentage increase of interface area from the perimeter for the dynamic films were plotted as a double y-axis graph verse dynamic deposition angle. The results are represented in Fig. 6.10 which shows a clear, systematic increase in porosity and perimeter area with angle of deposition.

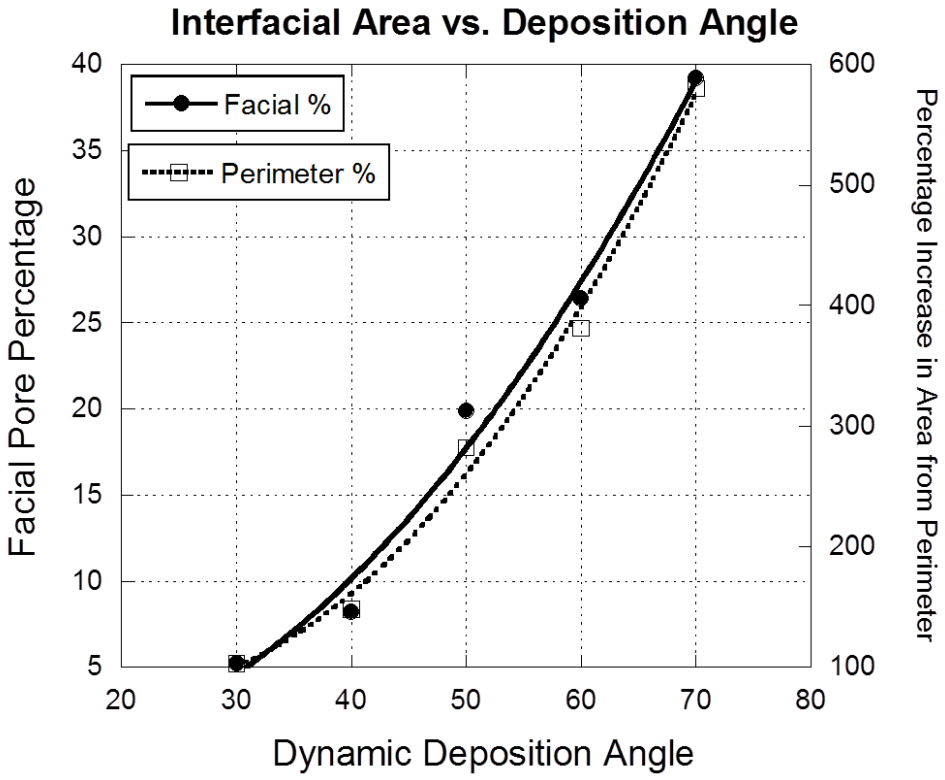

Figure 6.10: Plot of porosity and interfacial area dependence on dynamic deposition angle

6.3.4 Rocking Angle Dependence Electrochemistry

The FeF_2 electrodes produced by dynamic rocking angular deposition (28-32° through 68-72°) were cycled in galvanostatic mode between 4.50 V and 1.0V at 60°C and compared. The post deposition FESEM clearly showed that the canyon porosity extended to the substrate's titanium adhesion layer. Considering theoretical mass of a fully dense and nonporous film to be 100%, the corrected percentages based on porosity were calculated to be 94.8% (28-32°), 91.8% (38-42°), 80.5% (48-52°), 73.6% (58-62°) and 60.8% (68-72°). To improve cycling accuracy, the porosity percentages calculated for the films by image processing was multiplied by the theoretical mass to correct the mass and generate the specific capacity plots. It should be noted that throughout this study the specific current was held constant at 12.5 mA/g for both the dynamic and static samples.

The discharge specific capacity (mAh/g) verse cycle number plots for the films which were deposited over the range of dynamic rocking angles are shown in Fig. 6.11a and their first discharge profiles in Fig. 6.11b. The static 0° films had by far the worst capacity retention. Indeed, a 0° 700nm film had a first discharge capacity and percentage decrease after 10 cycles of 432mAh/g (93%). Regarding the dynamic substrate deposited samples, the capacity loss after 10 cycles was found to increase at the deposition angle and porosity extremes. The smallest angles (28-32° and 38-42°) with the least percentage of porosity and larger angle (68-72°) with the greatest porosity showed to have the most loss in capacity after 10 cycles. The first discharge capacity and percentage decrease after 10 cycles of the 28-32°, 38-42° and 68-72° were 344mAh/g (44%), 283Ah/g (58%) and 437Ah/g (52%) respectively. Capacity loss after

10 cycles improved for the mid-range deposition angles (48-52° and 58-62°) with a corresponding first discharge capacity and percentage decrease of 406mAh/g (21%) and 314mAh/g (12%) respectively. A summary of these results are shown in Fig. 6.12 where the perimeter area porosity percentages and the capacity loss for the dynamic films were plotted as a double y-axis graph verse dynamic deposition angle.

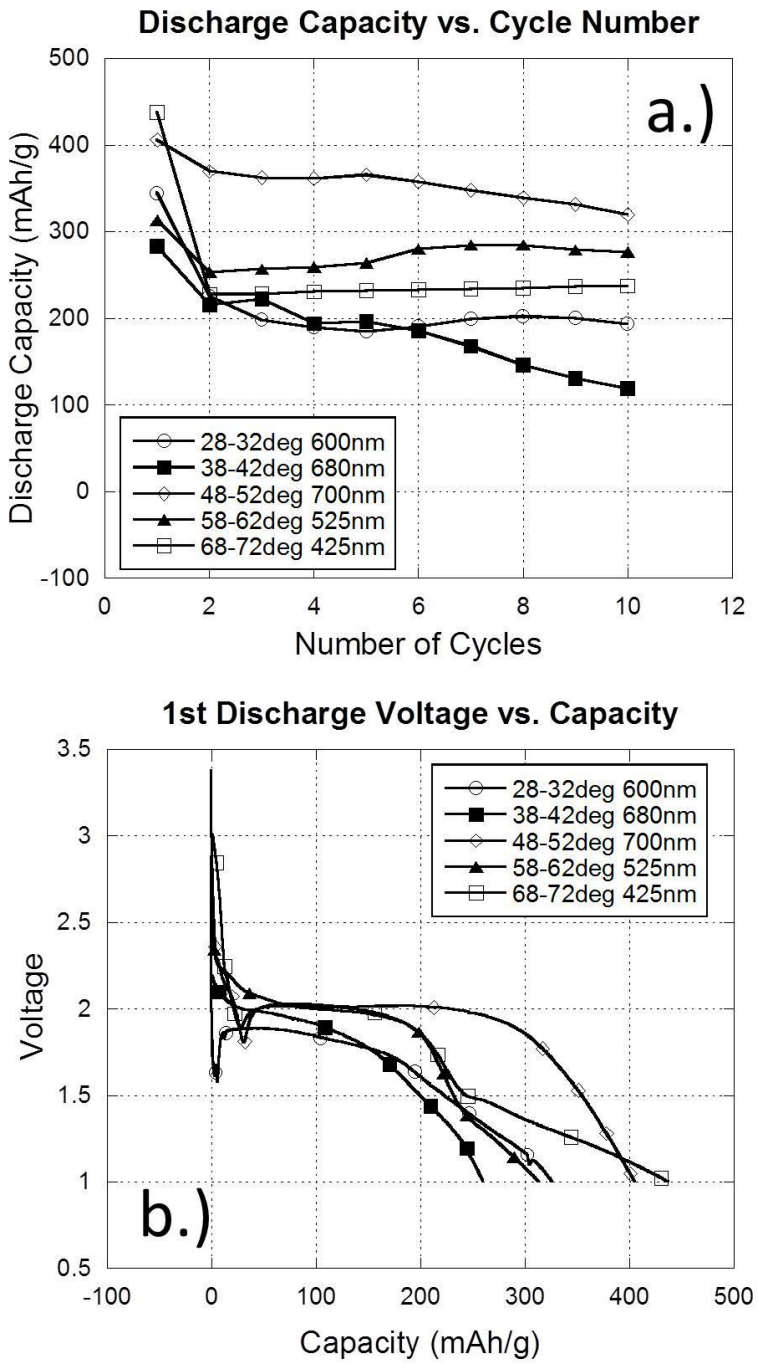

Figure 6.11: Dynamic rocking angular electrodes (a) specific capacity as a function of cycle number and (b) 1st discharge specific capacity profile

In summary, the general trend is that the cycling stability improved systematically

with the porosity generated (i.e. higher angles are associated with higher porosity) especially in contrast to the dense static film which will be discussed in more detail in the proceeding section. This trend abruptly drops off at 68-72° suggesting another mechanism of failure may be generated. This could range from poor interconnection amongst the grains due to the high porosity leading to accelerated de-adhesion from the substrate while cycling from mechanical forces, breakdown of lateral electronic percolation, enhancement of deleterious aspects of electrolyte interaction, or significant change in crystallography previously noted for this film deposition angle.

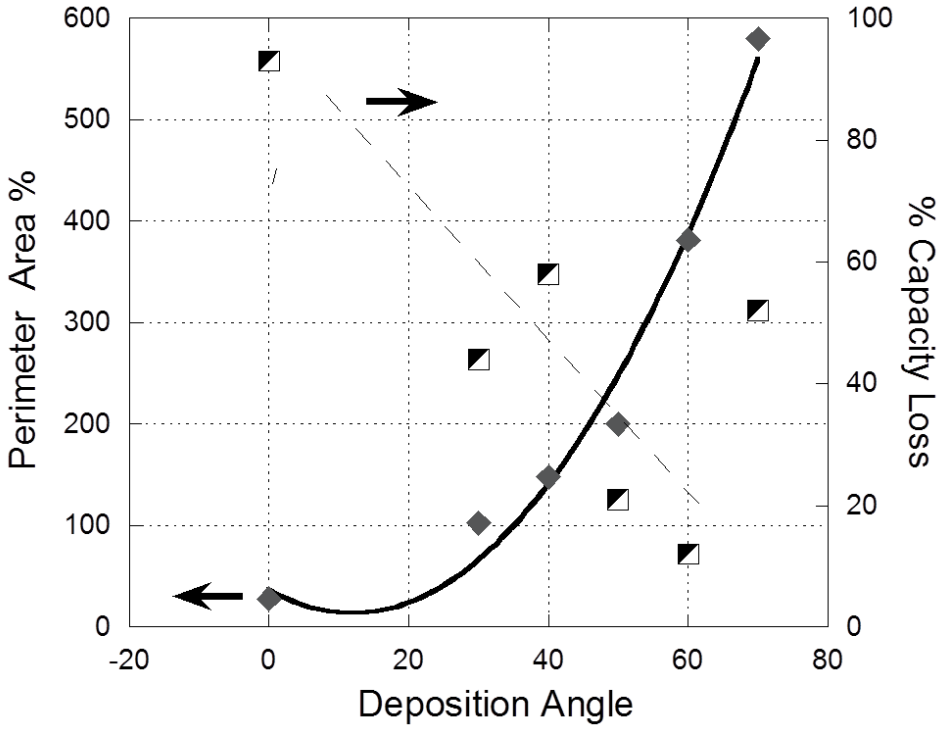

Figure 6.12: Influence of dynamic deposition angle on perimeter surface area and capacity

6.3.5 Electrochemistry Static vs. Dynamic as Function of Thickness

From the rocking angle dependence on electrochemistry results it can was shown that the 48°-52° film maintained the highest capacity over 10 cycles and best first discharge profile. Based on this performance result, this film was selected as the dynamic angle range sample to contrast electrochemistry as a function of deposition thickness to samples deposited at a static 0°.

The FeF_2 thin film static and dynamic electrodes, which have a theoretical conversion voltage of 2.66V, were cycled in galvanostatic mode at 60°C. Fig. 6.13a shows a comparison of the discharge capacity (mAh/g) verse cycle number of FeF_2 thin films cathodes of increasing thicknesses which were deposited dynamically at 48°-52° and statically at 0°. This plot shows the 48°-52° films having much greater discharge capacity retention over 10 cycles then the static films. In addition, the plot shows that the thinner films have a greater discharge capacity over 10 cycles. The first discharge capacity and percentage decrease after 10 cycles of the 48°-52° 400nm, 700nm and 850nm films were 371mAh/g (6%), 406Ah/g (21%) and 437Ah/g (38%) respectively. In sharp comparison, the first discharge capacity and percentage decrease after 10 cycles of the static 0° 400nm, 700nm and 850nm films were 450mAh/g (85%), 432Ah/g (93%) and 511Ah/g (94%) respectively.

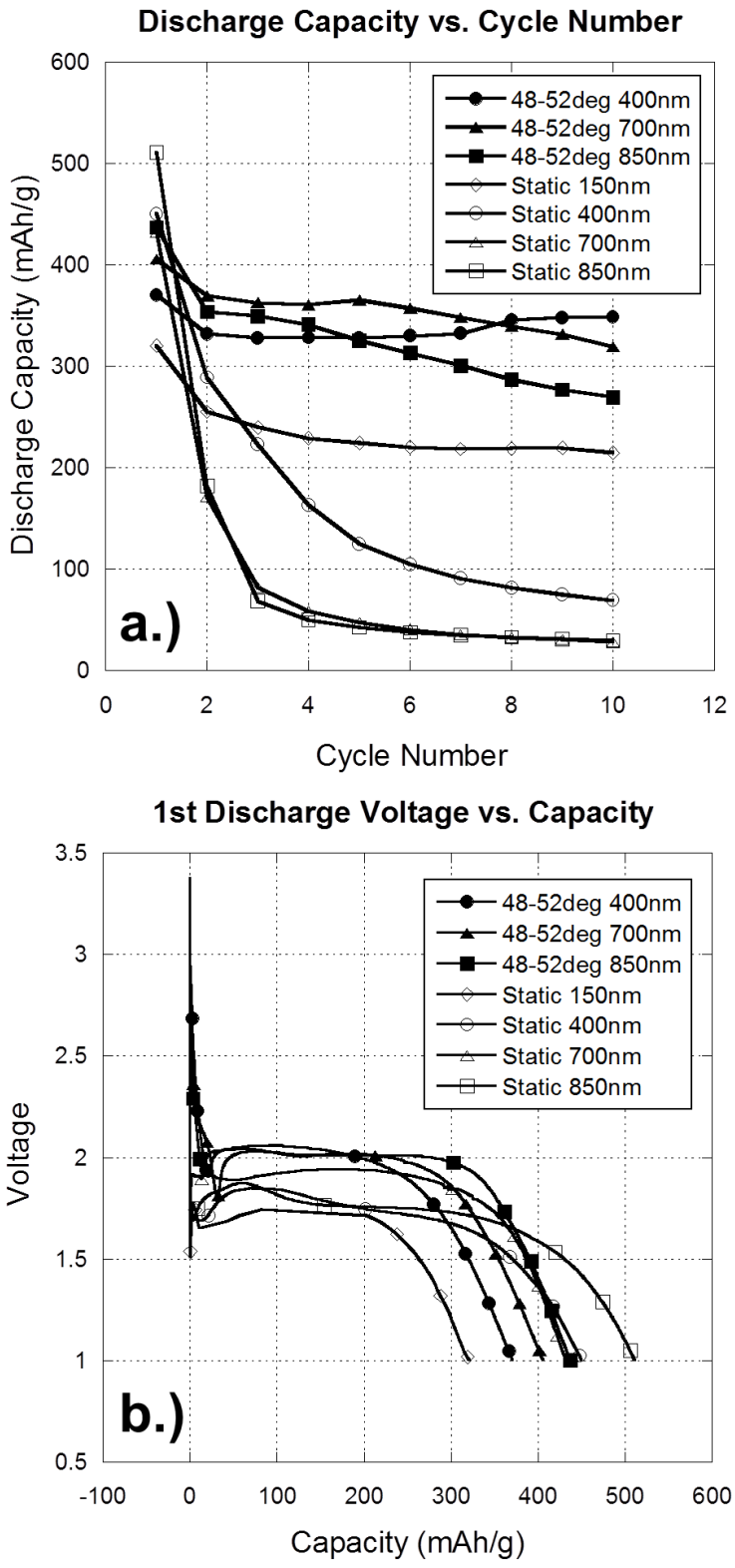

Figure 6.13: Static vs. Dynamic electrodes (a) specific capacity as a function of cycle number (b) 1st discharge specific capacity profile

Fig. 6.11b and Fig 6.13b show that all films regardless of thickness or morphology are able to achieve good utilization during the first lithiation. In all cases the dynamic films containing vertical porosity had a significantly higher 1st discharge voltage of about 2V vs. 1.75V. Fig. 6.14 through Fig. 6.16 shows the voltage profile comparing the static and dynamic 48-52° films. Commencing with the dynamic films, all showed reasonable reversibility even up to a thickness of 850nm. Although the hysteresis is relatively high, it is still quite surprising that such a thick film is electrochemically active. As discussed above, static films represent good initial lithiation capacities, but subsequent cycling was very poor regardless of the thickness resulting in rapid capacity fade.

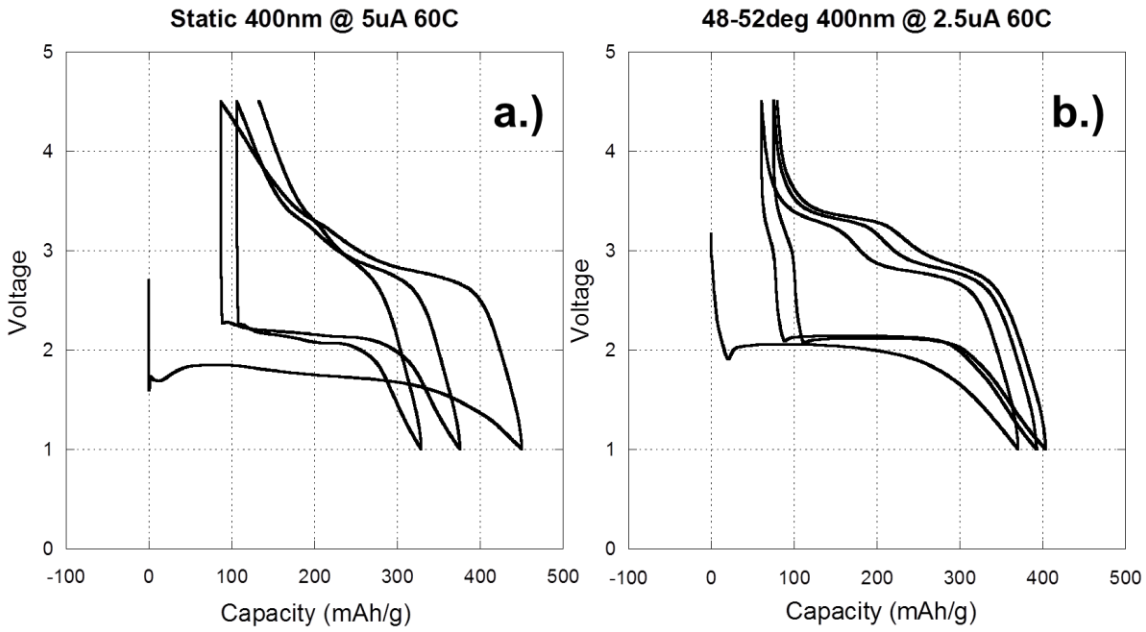

Figure 6.14: 400nm Static vs. Dynamic electrodes cycled galvanostatically between 4.50 V and 1.0V (a) static deposition (b) 48°-52° dynamic deposition

.

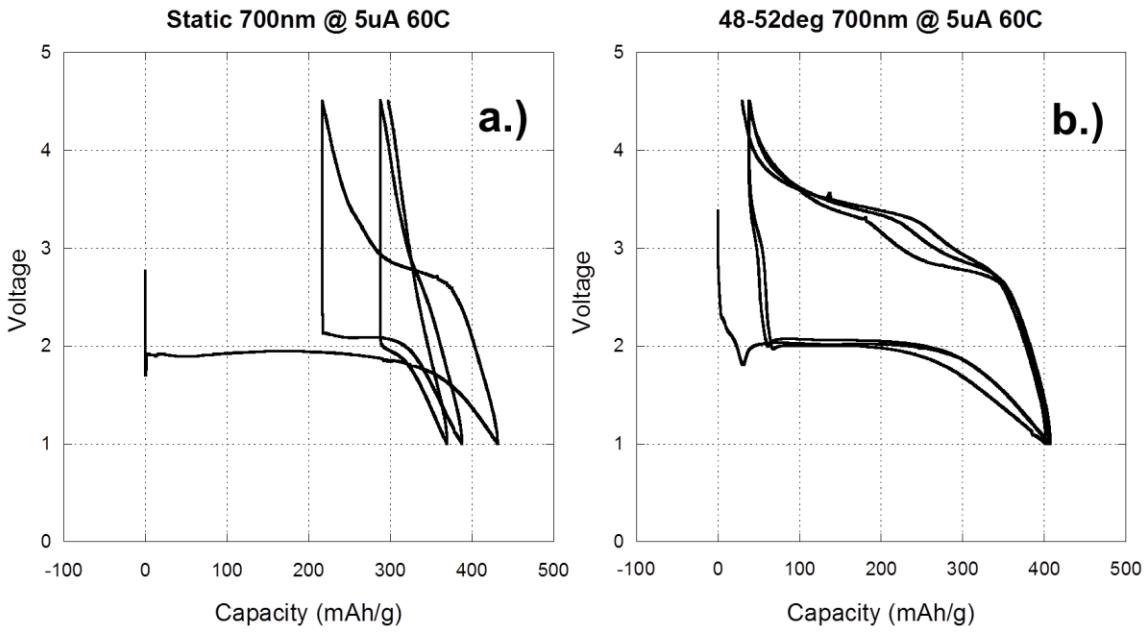

Figure 6.15: 700nm Static vs. Dynamic electrodes cycled galvanostatically between 4.50 V and 1.0V (a) static deposition (b) 48°-52° dynamic deposition.

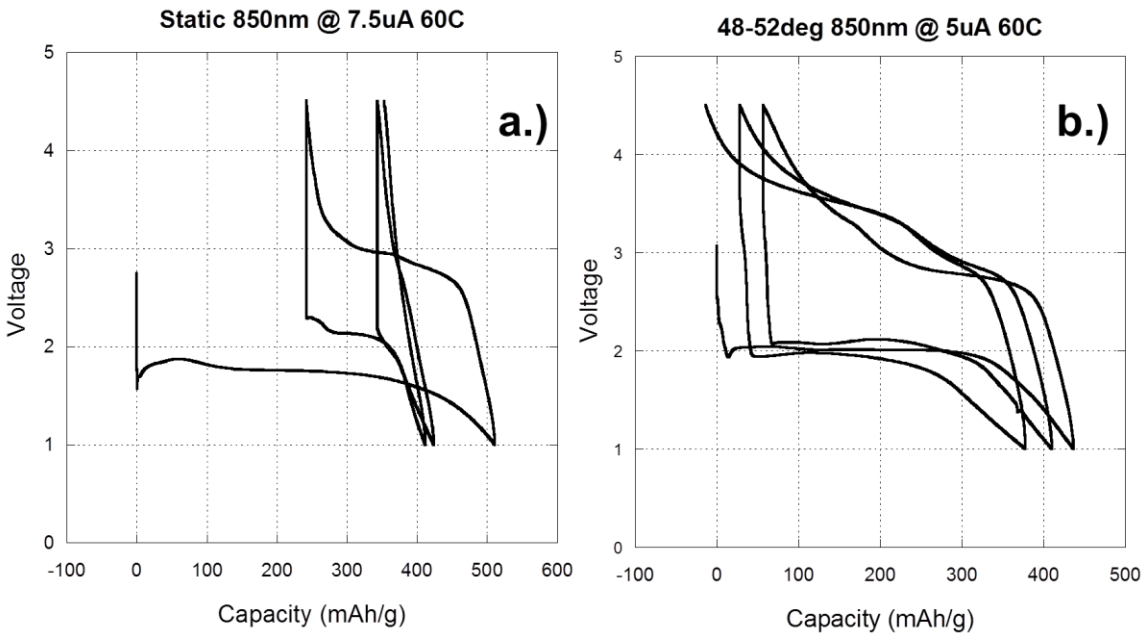

Figure 6.16: 850nm Static vs. Dynamic electrodes cycled galvanostatically between 4.50 V and 1.0V (a) static deposition (b) 48°-52° dynamic deposition

6.4 Discussion

Dynamic glancing angle deposition conditions lead to the production of phase pure FeF_2 films of systematically developed vertical porosity in sharp contrast to traditional films deposited under static 0^o conditions. The subsequent electrochemical analysis revealed significantly improved behavior for such films. The first discharge of the static and dynamic films reveal similar specific capacities although the static films show a significant increase in polarization and poor cycling, especially as the thickness is increased. The textured films result in a very significant improvement in cycling on par or better than published results for 20nm nanocomposites of FeF_2.[99,106] The question remains of how this is possible when the films are almost 1000nm thick and 20 nm has been shown to be a cut off point for reasonable electrochemical performance in typical

porous electrodes.

The width of the ridge-like structures are <300nm with considerable amount of vertically aligned mesoporosity. This electrolyte accessible porosity allows surface interaction with the film leading to known exceptionally fast conversion reaction on the surface of the FeF_2 host.[107] As FeF_2 is a high bandgap insulator, the conversion reaction must proceed at the point of electron transfer located at the substrate surface at the bottom of the vertical porosity (Fig. 6.1). It is known from that the conversion reaction of FeF_2 proceeds with a rapid transport on the surface of material. This occurs as the Fe that is produced is percolated and produces a perfect metallic conducting web embedded in the LiF. Consistent with the nature of a surface reaction, the Li diffusion is minimal and little ionic impedance develops as the Li^+ does not need to proceed through the reaction and into the depths of electrode. From there the conversion can proceed inward relatively quickly as the columns and ridges of materials are 4x thinner than the film itself.

The static “dense” film also exhibits full lithiation although the polarization is much higher. Theoretically, there is no mechanism for the electron to conduct through the relatively thick 800nm insulating film to initiate the reaction at the ionic interface with the electrolyte at the surface. It should be reinforced that the surface conversion reaction is quite fast and can spread an electronically conducting web over the entire surface; all it takes is an initiation point consisting of an electronic transfer from the substrate to the FeF_2 film in proximity to a Li^+ ion source from the electrolyte. In reality, this does exist even in the static dense films. As shown in Fig. 6.9, static films showed evidence of an intermittent film crack over a large spacing in excess of 5000nm that

could proceed to the substrate and allow the electrolyte to flow and initiate the reaction. All films have another possible initiation point existing around the perimeter of the film. This is bathed in electrolyte and will act as an initiation point. Granted, these reactions although rapid would then have to proceed from the outer perimeter to the center of the film which could be represented by the poor lithiation polarization which we observed.

The drastically improved cycling stability of the textured films may be rooted in the improved ability of this film to absorb the stresses of the conversion process (Eq. 1) which leads to a 16.7% volume expansion, In the textured film, the pores may close during the lithiation thereby absorbing the stresses of the expansion without mechanical decomposition of the film as could be imagined for the dense static film. This is not unlike the much improved performance observed for collimated alloy films for high volume expansion negative electrodes relative to static films.[108,109] To test this theory static and dynamic films were analyzed by microscopy after the first lithiation.

A 400nm static and 400nm 48-58° dynamic films were discharged one time and FESEM images were taken to compare the evolution of the microstructure of the lithiated sample. Fig. 6.17 shows the FESEM results of the lithitated static and dynamic films. Static films revealed little change in morphology or apparent damage when compared with the initial film depicted in Fig. 6.4a and 6.4b. In sharp contrast, the micrographs show that the pores on the dynamic sample have been reduced from their original size due to lithiation. The 400nm 48-52° dynamic film image was processed with Image-J software and a 13.7% facial porosity was determined. Fig. 6.18 shows that the pores have been reduced by 29.7% when compared to the original pre-lithiated which had 19.5% facial porosity. The ability to release the stress laterally into the film pore

may preserve the mechanical and subsequent electronic integrity of the film at the substrate interface or across electronic breaks in the films which may occur across grain boundaries due to electromechanical grinding. Indeed, the abrupt capacity loss observed for the static films after a successful first lithiation may be rooted in stress release at the film substrate interface.

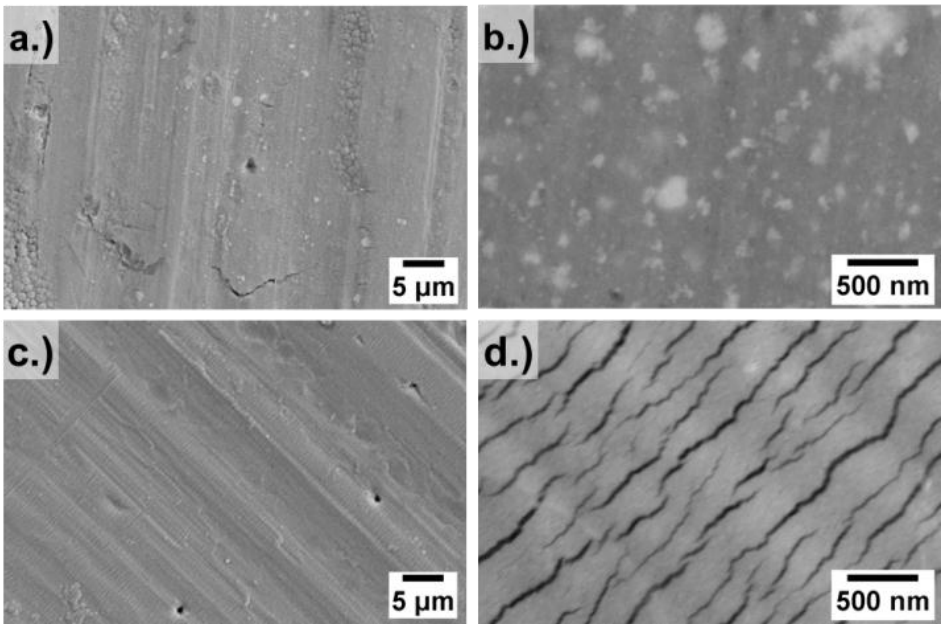

Figure 6.17: FESEM images of lithiated films Static 400nm (a) 2kX (b) 35kX and Dynamic 48°-52° 400nm (c) 2kX (d) 35kX

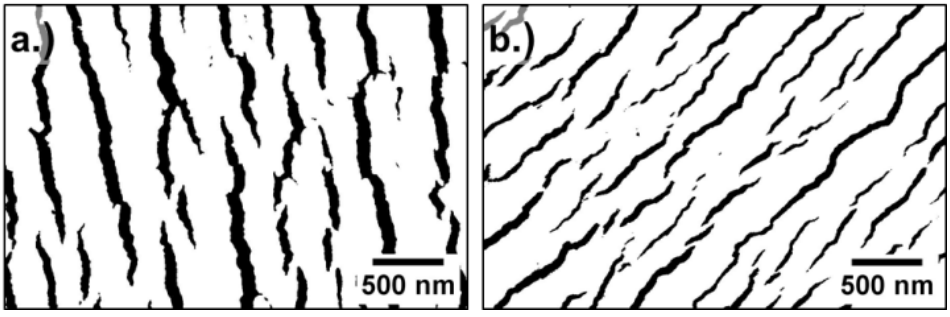

Figure 6.18: Image processing of Dynamic 48°-52° 400nm films at 35kX magnification (a) pre-lithiated and (b) lithiated

6.3.4 LiPON Solid Electrolyte Coated Films

The films were coated with LiPON (lithium phosphorus oxynitride) in an attempt to better understand the FeF_2 reaction mechanism and to determine if possibly the electrode interaction with the $LiPF_6$ EC: DMC electrolyte leads to accelerating the loss in cycling capacity. Discussed earlier, in terms of the FeF_2 reaction mechanism, initial Li^+ insertion into FeF_2 is restricted because Fe^{2+} reduction is required. For Li^+ insertion to occur some Fe^{2+} would need to be reduced to either Fe^{1+} or disproportionation to Fe^0 and Fe^{3+} would need to take place. In general, solid-state Fe^{1+} is very unlikely and oxidation states <2+ are uncommon for elements of the first transition series. If some Fe^{2+} reduction to Fe^0 combines with some Fe^{2+} oxidation to Fe^{3+}, then metallic iron would likely precipitate out of the iron fluoride structure.[7] In addition, it has been noted that the metallic nanodomains formed during lithiation of certain conversion materials can be very catalytic toward the cathodic decomposition of the electrolyte leading to a film of carbonates on the electrode surface.[110] With conversion materials, the solid-electrolyte interphase (SEI) film may decompose or the metal fluoride may reconvert to metal oxide or oxyfluoride phases affecting subsequent cycling behavior.[111]

Once the FeF_2 films were fabricated by the ebeam chamber, the LiPON was applied with a RF sputtering of a Li_3PO_4 source in nitrogen plasma to create lithium phosphorus oxynitride (LiPON). The FeF_2 electrodes were coated with a 50nm and 100nm thick layer of LiPON. The cells were then fabricated in the same method as with the cells discussed previously, including the addition of $LiPF_6$ EC: DMC electrolyte which was placed on top of the LiPON. The electrochemistry cycling results are shown

in Fig. 6.19, 6.20 and 6.21 for the static and dynamic films. Similar to the non-LiPON cells discussed earlier in this chapter there are still some undesirable side reactions that seem to be present indicated by the multiple plateaus above 2.8 V during charge. These reactions may be associated with the oxidization of iron to a higher valence state, such as Fe^{3+} as mentioned by previous literature.[7] Although, these reactions are present in the LiPON cells they appear to be reduced from the cells without LiPON possibly suggesting there is less metallic iron precipitating out of the iron fluoride structure.

To determine if the cycling retention has improved with the LiPON coated cells the discharge capacity verse cycle number was plotted and shown in Fig. 6.22. This plot shows a slight improvement in retention for the static 400nm film. The dynamic films require further long term cycling results from the non-LiPON films to determine if the films showed improvement.

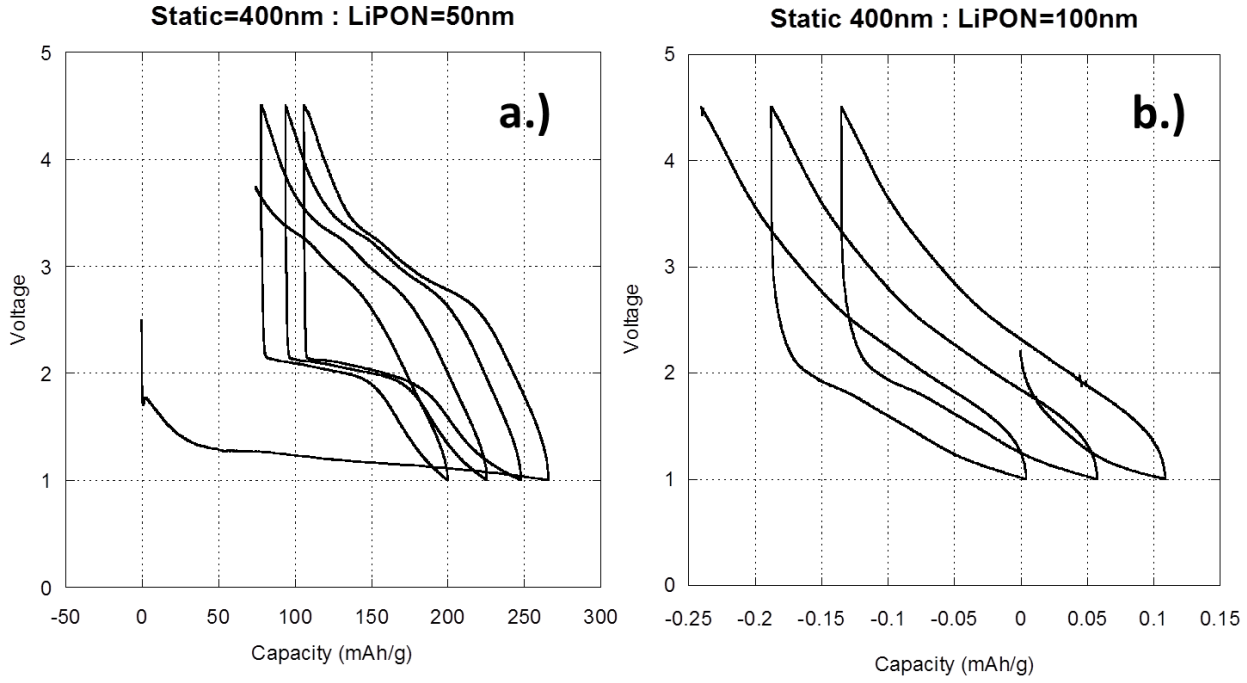

Figure 6.19: Voltage vs. Capacity of Static 400nm (a) LiPON=50nm and (b) LiPON=100nm

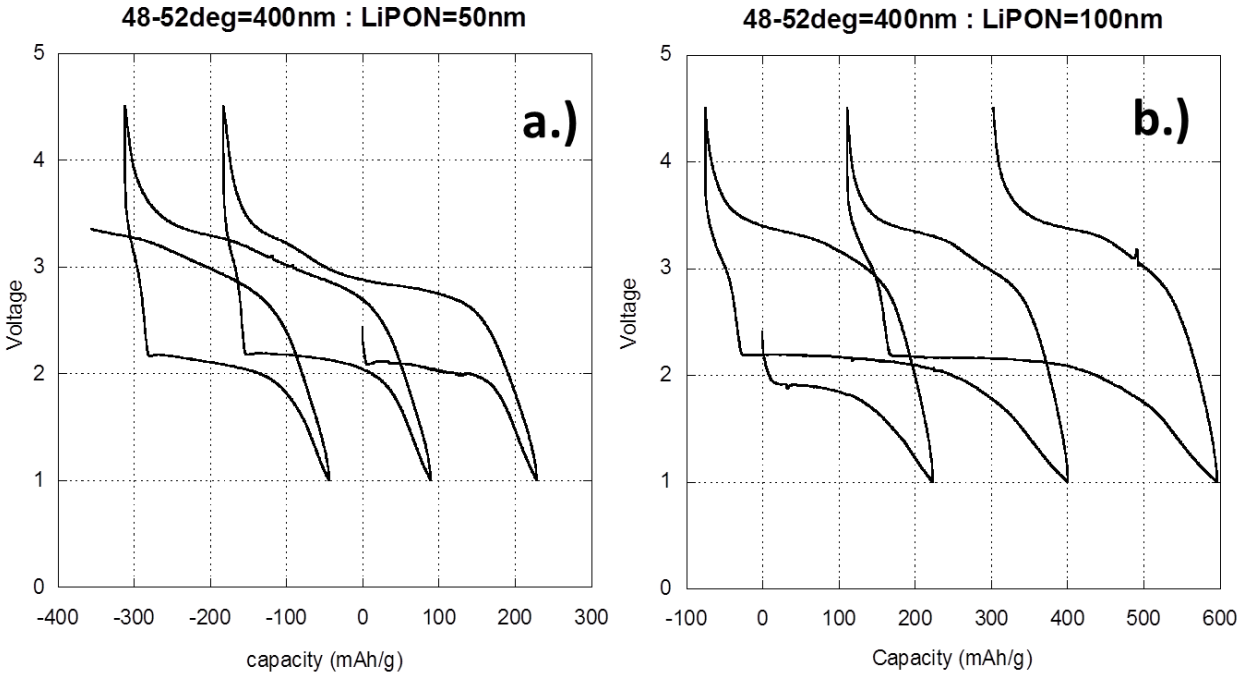

Figure 6.20: Voltage vs. Capacity of 48°-52° 400nm (a) LiPON=50nm and (b) LiPON=100nm

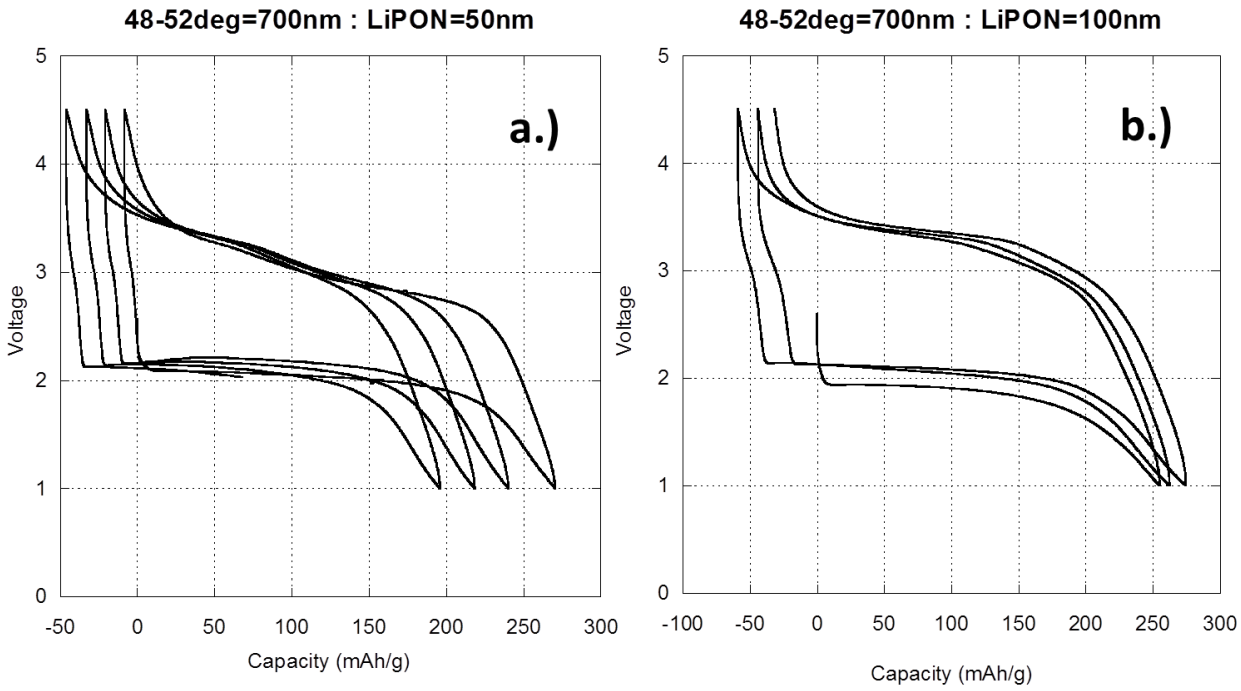

Figure 6.21: Voltage vs. Capacity of 48°-52° 700nm (a) LiPON=50nm and (b) LiPON=100nm

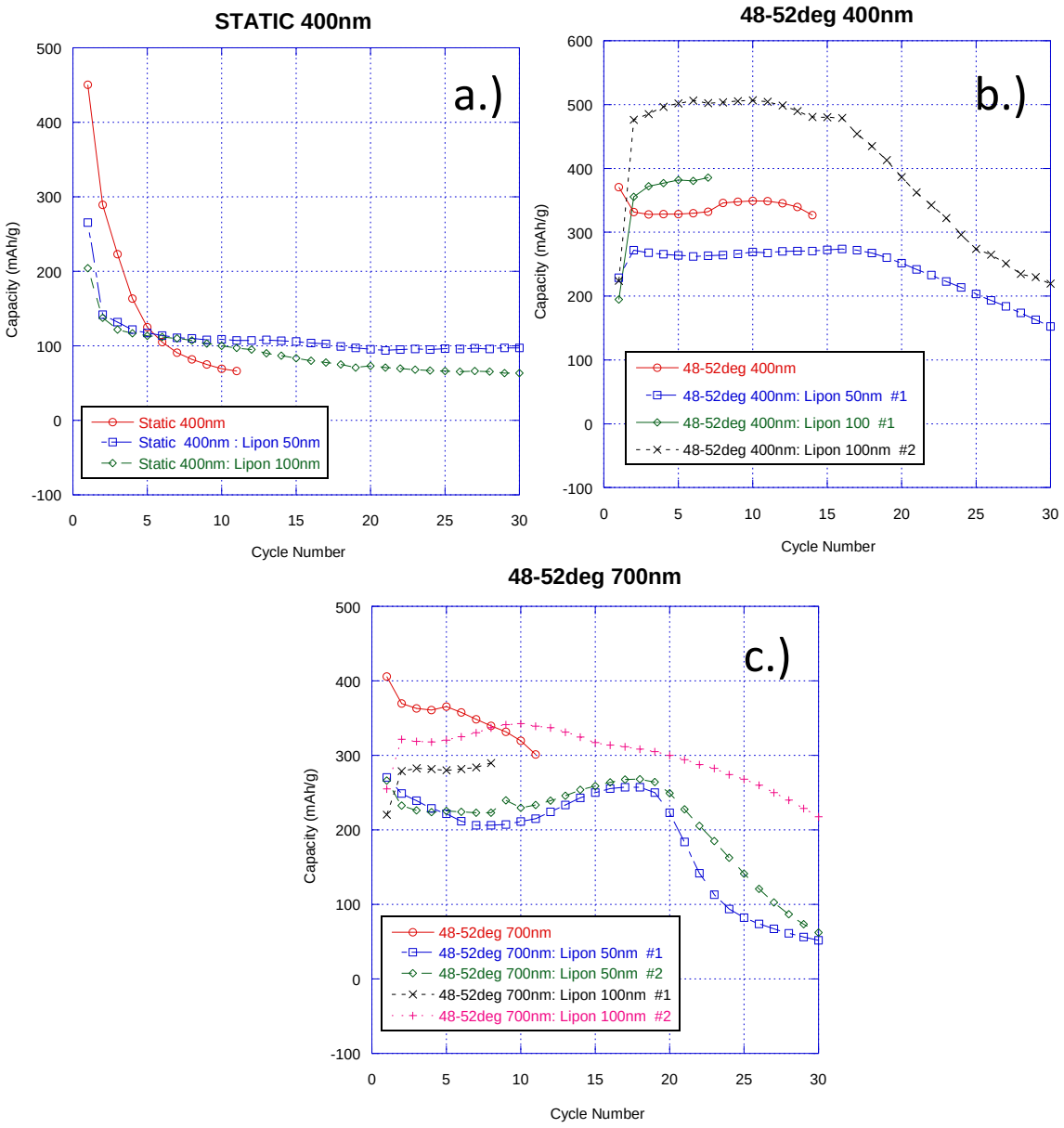

Figure 6.22: LiPON cells Discharge Capacity vs. Cycle Number (a) Static 400nm (b) 48°-52° 400nm and (c) 48°-52° 700nm

6.5 Conclusions

Glancing angle deposition with dynamic rotation of the substrate produced FeF_2 films with tailored percentages of deep channelled porosity. These films have shown to

significantly improve electrochemical performance over statically produced dense films. The improved performance can be associated with both the porosity allowing additional electrolyte surface interaction deep within the film's thickness which leads to known exceptionally fast conversion reaction and the porosity enhancing mechanical stability as they absorb the stress caused from the volume expansion of the reaction.

The study reveals how the performance of conversion reaction electrodes can be improved with deep channelled porosity. These dynamic films have thicknesses of close to 1000nm and are 6x thicker than previous electrochemical studies with FeF_2 films yet have improved performance, providing insight into constructing conversion reaction electrodes in the future with greater potential energy storage.

7 Effect of FeF2 Thin film Microstructure on Surface Specific Capacitance

7.1 Introduction

The rate performance of a battery improves when there is a large contact surface area between the electrode and the electrolyte in electrode materials exhibiting frustrated ionic diffusion. The contact surface area increases as the electrode becomes more porous thereby lowering the surface area specific ionic current for the charge transfer reaction.[56] The porosity relationship holds until approximately the onset of micro porosity at 2nm below which electrolyte species are sterically hindered from entering the porosity.[56] With increasing electrolyte accessible porosity and subsequent surface area of the electrode, the kinetics of mass transfer of Li ion is increased.[62] Such transport issues are exaggerated to even a greater degree in the case of thin films where the film

structure is dense with limited porosity. This is especially beneficial as the film thickness is increased for a gain in area capacity.

Typically the bulk mass transfer may become more difficult as discharge continues as the result of the cathode volume expansion during discharge and temporary or permanent depletion of the porosity near the surface of the primary particle depending on the reaction mechanism. This is especially an issue for reaction mechanisms where large degrees of expansion occur such as conversion or alloying reactions which can range from 10 to 300%, respectively.[35,36,37,38,39] During the cathode volume expansion, the pores with fine openings are easily sealed. As a result, mass transfer in and out of these pores becomes more difficult. Designing an electrode that maintains large internal surface area and allows for fast mass transfer to access this area is one of the keys to achieving high rate capability and mechanical stress release.

In designing an electrode for increased internal surface area it is important to note that the porosity of the electrode is inversely related to the size of the particles which comprise the electrode. For example, if the electrodes are produced from powder the primary particles sinter together due to surface forces to form secondary particles. Pores are formed in between the sintered secondary particles. The pore size depends on the size and shape of primary particles and the conditions in which they are packed. Pores with different sizes have different time constants and cannot be accessed at the same time. In addition, not all the pores can be accessed electrochemically. Due to the aforementioned steric limitations, electrochemically accessible surface area is normally smaller than the common BET measurement method of surface area. Therefore,

electrochemical impedance spectroscopy can be utilized as a rarely used but alternative quantitative measurement approach for determining the accessible surface area.[52,53,54,55] In electrochemical impedance spectroscopy, a small sinusoidal AC excitation signal is applied to the open circuit or DC potential biased cell producing an AC current signal which is recorded as a function of frequency. The regression of the measured impedance as a function of frequency provides insight about the electrochemical capacity of the electrolyte-electrode interface.

Electrochemical impedance spectroscopy is capable of predicting the electrochemical accessibility surface by measuring the double layer capacitance of the electrode show in Fig.7.1.[56] The double layer is established at the electrochemical interface between the electrolyte and electrode where the charge transfer interfacial reaction occurs. The capacitance of the double layer is proportional to the electrochemical accessibility surface area of the electrode and inversely proportional to the thickness of the double layer. Electrochemical impedance spectroscopy can be used for relative comparisons between samples of identical composition with the interface double layer capacitance result being proportional to the electrolyte accessible surface area.

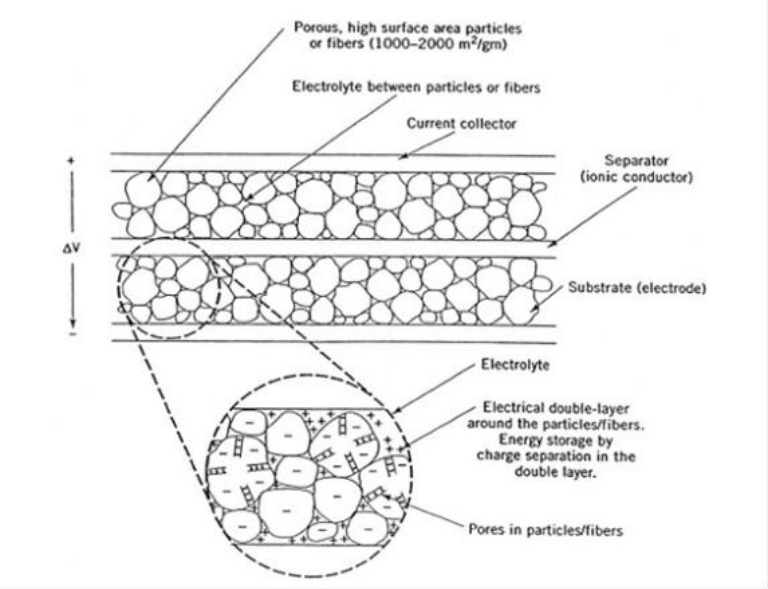

Figure 7.1: Ions from Solution forming a Double Layer Capacitance within Porous Electrode[56]

The Randles circuit in Fig. 7.2 is used to calculate the double layer capacitance of an electrolyte-electrode interface using electrochemical impedance spectroscopy.[57] The equivalent circuit is comprised of the solution (electrolyte) resistance Rs, the charge transfer resistance Rct, the double layer capacitance Cdl and the Warburg impedance W. The Nyquist plot in Fig. 7.2 represents the impedance as a function of frequency. From the Nyquist plot, the double layer capacitance can be calculated from the frequency at the maximum of the semicircle ($\omega=2\pi f=1/Rct*Cdl$). The product of Rct and Cdl is often termed the time constant τ of the electrochemical process. The 45° line indicating Warburg-limited behavior can be extrapolated to the real axis. The intercept is equal to $Rs + Rct - 2\sigma Cdl$, from which σ and diffusion coefficients can be calculated. The solution resistance, Rs, depends on the ionic concentration, type of ions, temperature, and the geometry of the area in which current is carried. The double-layer

capacitance, Cdl, results from charge being stored in the double layer at the electrolyte-electrode interface. The charge transfer resistance Rct refers to current flow produced.

The trend of a typical Nyquist plot for the Randles circuit can be explained. When the oscillation frequency decreases, a very thin film of charge (double layer) starts to grow on the electrode-electrolyte interface with time. With the formation of this film the charge transfer resistance increases with a decrease of frequency. This eventually increases impedance. In the low frequency region (to the right of the plot), the accessible surface area becomes significant because large surface area allows more charge to pass by and thus reduces impedance although surface area normalized impedance will, of course, remain the same.[57]

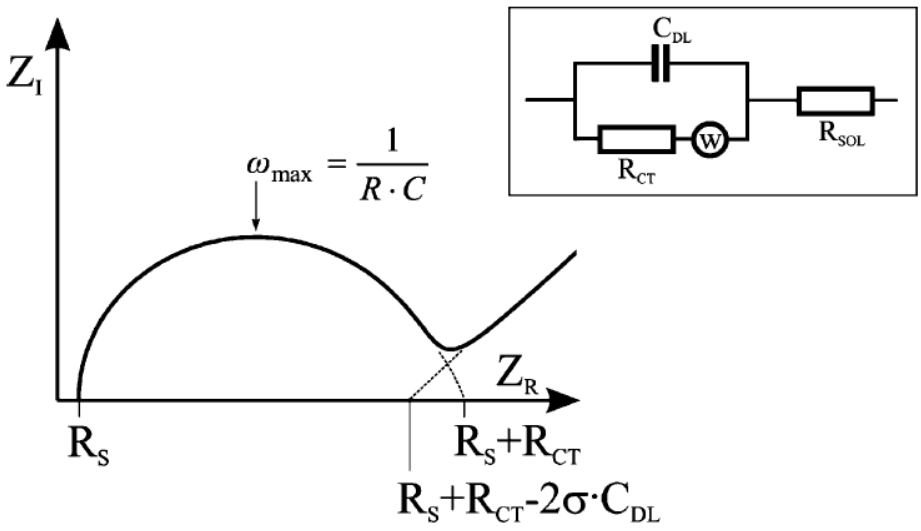

Figure 7.2: Randles Impedance Nyquist Plot and AC Impedance Equivalent Circuit[57]

Despite the simple classical circuit definitions previously discussed, the impedance results for some electrode/electrolyte interfaces cannot be described by simple circuit elements such as resistances, capacitances, inductances or convective diffusion (Warburg) impedance.[59] This occurs in systems where the Nyquist plot is not a

semicircle with the center on the x-axis but instead the observed plot was the arc of a circle with the center some distance below the x-axis. This trend of semicircle has been most commonly explained by some property of the system not being homogeneous or that of the value of some physical property of the system has some frequency distribution (dispersion). The inhomogeneity or frequency dispersion is generally attributed to a capacitance dispersion expressed instead in terms of a constant phase element (CPE). Therefore, constant phase elements (CPE) are used extensively in equivalent electrical circuits for fitting of experimental impedance data.[112-117] The CPE behavior is induced by varying activation energies on the surface causing inhomogeneous reaction rates, varying electrode thickness or composition, surface roughness, fractal geometry, porosity and current and voltage distributions associated with electrode geometry. For homogenous materials which are acting as ideal capacitors the impedance is represented by Eq. 1, where *i* is the imaginary unity and ω is the cyclic frequency. When there is CPE behavior with inhomogeneity or frequency dispersion, the impedance is represented by the CPE and defined by two values, CPE-T and CPE-P described in Eq. 2. CPE-P has a value between –1 and 1 where if CPE-P=1 then Eq. 2 is identical to that of an ideal capacitor and CPE-T is equal to the double-layer capacitance (Cdl).

$$Z = \frac{1}{\mathrm{Cdl}\,(i\omega)} \quad (1) \qquad\qquad Z_{\mathrm{CPE}} = \frac{1}{\mathrm{CPE_T}\,(i\omega)^{\mathrm{CPE_P}}} \quad (2)$$

This study utilizes FeF_2 which is a conversion reaction cathode battery material. Conversion reaction cathodes have been studied as a high energy density replacement

option to commercial intercalation secondary batteries for over a decade. However, commercialization of these electrodes has been obstructed by cycling performance issues most notably cycling retention and reversibility. Past literature have used FeF_2 powder form electrode cycling has been improved through adding conductive matrix such as carbon to form a nanocomposite. In addition, recently it was shown that canyon like porous FeF_2 thin films of specific optimized porosity percentages have improved cycling performance. This study uses electrochemical impedance spectroscopy (EIS) as a method to predict relative comparisons between electrode samples of identical FeF2 composition with the interface double layer capacitance and CPE-T result being proportional to the accessible surface area hence porosity.

The porous films for this study were produced with a novel thin film deposition system. The system has the capability to manufacture consistent thin films of a wide range of thicknesses with unique morphologies which can influence the film's interfacial surface area. The system is based on a physical vapor deposition technique called glancing angle deposition (GLAD) where the morphology of the film growth can be controlled through substrate rotational positioning at defined oblique angles to the deposition source.

7.2 Experimental

The thin films were prepared in a custom fabricated high vacuum electron beam evaporation chamber which has been described elsewhere. The substrate was prepared using unpolished high-strength aluminum alloy 7075 (McMaster-Carr) with a thickness of 0.8mm and was cut into a 25mm x 75mm strip. The Al-7075 strip was

cleaned with acetone then methanol and placed in substrate holding plate. Two cleaned glass microscope slides 25mm x 75mm with a thickness of 1mm were placed on each side of the Al-7075 strip and the three pieces were secured to the substrate holding plate using Kapton® tape. The glass slides were later used to measure film thickness with a stylus profilometer.

The source material of approximately 5g total of FeF_2 powder (Advanced Research Chemicals) was packed tightly into three of the four 2cc graphite crucible liners. The fourth crucible liner was loaded with titanium (99.99% Ti granules, Alfa) as an adhesion layer. The vacuum chamber was brought to a pressure of $3x10^{-6}$ Torr for the depositions. The adhesion layer, 50nm of titanium, was first deposited onto the substrate with an approximate deposition rate of 10A°/sec. Next, FeF_2 was deposited with a rate of approximately 13A°/sec. Once the deposition was completed, the chamber was vented with a combination of nitrogen then dry air. The films were removed from chamber, exposed to room atmosphere for approximately 1 minute and then stored in a helium filled glovebox (<0.6 ppm H_2O <0.1 ppm O_2) until coin cell fabrication and characterization trials began. The cell fabrication consisted of punching 14.3mm electrode discs from the film/substrate with a hand press which took place in room atmosphere for approximately 3 minutes.

7.2.1 Physical Characterization

The thickness of the Ti (50nm adhesion layer) and FeF_2 film was analyzed using the two microscope glass slides substrates with a stylus profilometer (Dektak 150) in room atmosphere. The alloy Al-7075 substrate had a surface roughness of Ra=0.3 micron so the glass slide allowed for a smoother surface to reference as zero thickness.

The FeF_2 film with the Ti adhesion layer on the glass substrates were measured in four locations and an average thickness was calculated and then subtracted by 50nm (the titanium adhesion layer) to determine the FeF_2 film thickness.

X-ray Diffraction (XRD) (Bruker D8 Advance, CuKα radiation) was performed in room atmosphere with a dedicated 10mm x 10mm piece of film.

FeF2 films were analyzed with a Field Emission Scanning Electron Microscopy (FESEM) (Zeiss) and the films were exposed for approximately 2 minutes to room air while being mounted in the FESEM.

Image-J, an imaging processing and analysis Java based software (National Institute of Health, USA) was used to modify the FESEM images into binary images. These binary images were then used to calculate the canyon facial porosity percentage, the perimeter length of each canyon and any surface cracks.

7.2.2 Electrochemical Impedance Spectroscopy (EIS)

All batteries fabricated for studies in this paper were aluminized (on the positive electrode) 2032 coin cells (Hosen) made with cathodes consisting of a 14.3 mm diameter disc of iron fluoride film, two layers of borosilicate glass fiber separator (Whatman) with a diameter of 15.9 mm soaked with electrolyte, and a 0.3mm thick 12.7mm diameter lithium metal foil as the anode counter electrode (half-cell) (FMC). The electrolyte was 1 M $LiPF_6$ EC: DMC purchased from Novolyte, stored in a helium filled glovebox and used without additional treatment.

Electrochemical impedance spectroscopy (EIS) was performed with a Solartron Models SI 1287 and SI 1260. The SI 1287 is capable of controlled potential and current

techniques and was paired with the SI 1260 to perform electrochemical impedance spectroscopy. The two units are controlled by a computer through GPIB running ZPlot software (Scriber Associates). The EIS was performed at room temperature with a frequency range of 10^{-3} to 10^{5} Hz and AC voltage of 80mV. Using the Zplot software, the CPE-T value was generated and used to compare the relative porosity of the thin films.

7.3 Results

7.3.1 Crystallography

XRD was performed on the films to understand the crystallographic orientation. The films were scanned from the 2θ ranges of 20-37° and 48-65° and were not scanned in the 37-65° range due to large peaks created from the Al-7075 substrate preventing evaluation of the film. Fig. 7.3 shows the results of the XRD scans and was produced with Topas software. Fig. 7.3a shows the scans of films produced dynamically in a series of substrate angles, 28-32°(600nm), 38-42°(680nm), 58-62°(525nm) and 68-72°(425nm). Fig. 7.3b shows the scans of films produced dynamically at a substrate angle of 48-52° and thicknesses of 400nm, 700nm and 850nm. Fig. 7.3c shows the scans of films produced statically at a substrate angle of 0° and thicknesses of 400nm, 700nm and 850nm. Fig. 7.3d shows the scans of films produced statically at a substrate angle of 0° and thicknesses of 600nm, 800nm and 1500nm. As presented earlier in chapter 6, all phases were found to be single phase rutile FeF_2 with lattice parameters in good agreement with the reported values of a=4.7 and c=3.31. The film deposited at 68-72° was found to be somewhat amorphous with no defined (110) peak. All films besides the latter were found to be highly textured in the <110>.

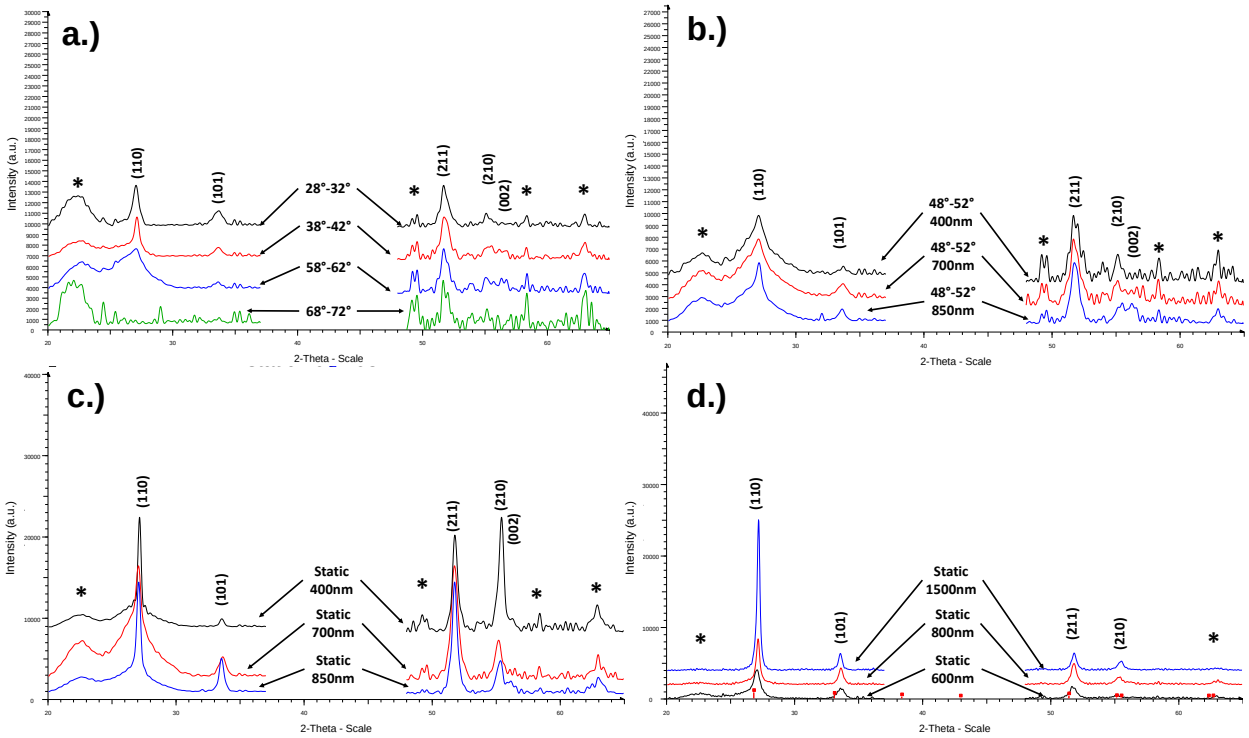

Figure 7.3: XRD results of (a) dynamic (b) 48°-52° 400nm,700nm,850nm (c) Static 400nm, 700nm, 850nm and (d) Static 600nm, 800nm, 1500nm

7.3.2 Micro and Nanostructure

The static and dynamic rocking thin films were analyzed with FESEM. Fig. 7.4 shows the static films of 400nm, 600nm, 700nm, 800nm, 850nm and 1500nm at 2kX and 35kX magnification. For the static films, the images show a dense non porous morphology which contains spurious, random surface cracks that are widely spaced on the order of 5000nm. The general trend is that surface cracks increase with increasing thickness.

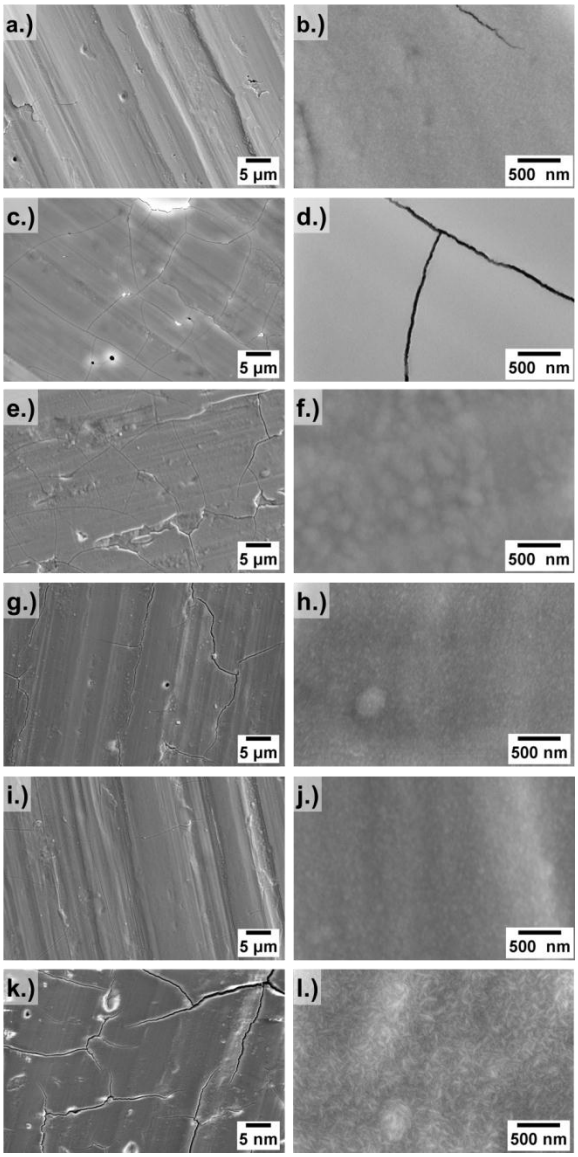

Figure 7.4: FESEM images of Static 400nm (a) 2kX (b) 35kX, Static 600nm (c) 2kX (d) 35kX, and Static 700nm (e) 2kX (f) 35kX, Static 800nm (g) 2kX (h) 35kX, Static 850nm (i) 2kX (j) 35kX and Static 1500nm (k) 2kX (l) 35kX.

Fig. 7.5 shows FESEM images of the dynamically deposited films of 28-32 degree, 38-42 degree, 48-52 degree, 58-62 degree and 68-72 degree at 2kX and 35Kx magnification. These films generate morphology reminiscent of very finely spaced porous canyons which is in contrast to static films which contain surface cracks of large spacing**.** With the dynamic films, the width of the canyon and spacing between them is

dependent on the angle in which the film was deposited. The width and spacing of the canyons decrease with increasing deposition angle. The film that is deposited at 28-32 degree has the greatest spacing of approximately 1200nm and least amount of porosity and the 68-72 degree film as the least spacing of approximately 50nm and greatest porosity. The width of these canyons which appear to be tiger stripe pores when viewed from above range from approximately 50-150nm depending on the deposition angle in which the film was deposited.

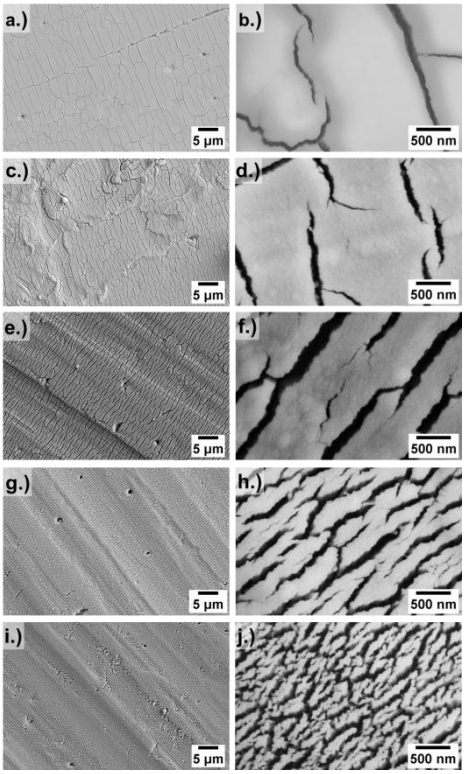

Figure 7.5: FESEM images of 0.65rpm 28°-32°(a) 2kX (b) 35kX, 38°-42°(c) 2kX (d) 35kX, 48°-52°(e) 2kX (f) 35kX, 58°-62°(g) 2kX (h) 35kX and 68°-72°(i) 2kX (j) 35kX.

7.3.2 Quantitative Microstructure Analysis

Image processing was used to calculate the static and dynamic facial porosity percentage and the perimeter length of each crack (static) and canyon (dynamic). The

FESEM images were modified into binary images using Image-J software which are shown in Fig. 7.6 and Fig. 7.7. Using the Image-J software, facial porosity area percentage which is represented in dark contrast and the outlying perimeter length of the pore were calculated. This pore perimeter length was multiplied by the film thickness to calculate the additional interfacial surface area created within the canyon walls.

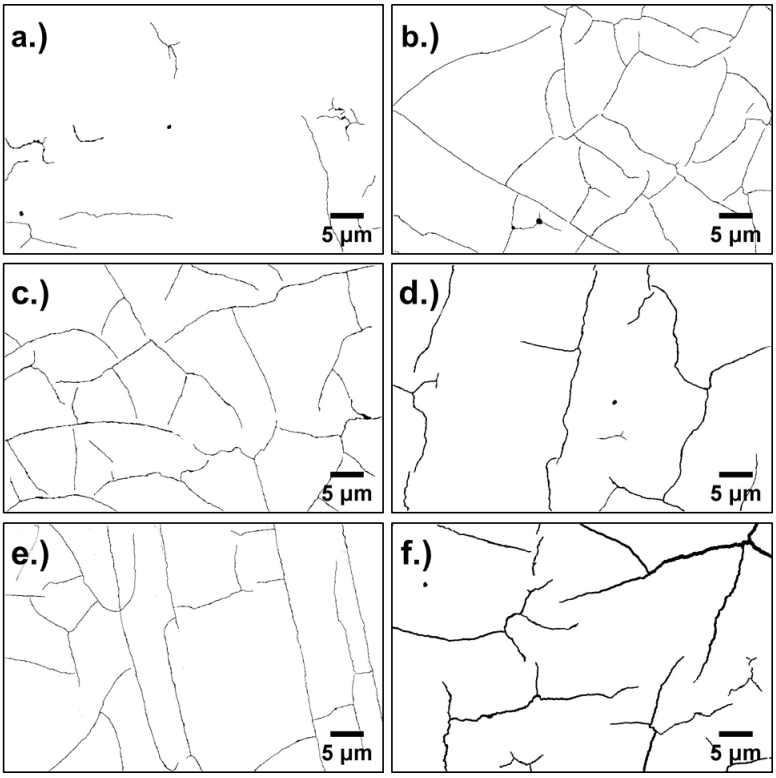

Figure 7.6: Image processing of 2kX FESEM images of Static 400nm (a), Static 600nm (b), Static 700nm (c), Static 800nm (d), Static 850nm (e) and Static 1500nm (f).

The results in Fig. 7.6 a.), b.), c.), d.), e.), f.) show the images of the 400nm, 600nm, 700nm, 800nm, 850nm and 1500nm respectively. The percentage of facial area porosity was calculated to be systematically increasing with film thickness; 1.08% (400nm), 1.68% (600nm), 1.85% (700nm), 1.95% (800nm), 1.29% (850nm) and 3.55%

(1500nm). In Fig. 7.10b the total interfacial area including both from facial and perimeter wall porosity is plotted verse the film thickness. The plot shows a linear dependence between the facial porosity and thickness. The calculated percentage increase in area from the perimeter is 5.9% (400nm), 23.7% (600nm), 27.7% (700nm), 15.8% (800nm), 30% (850nm) and 40.4% (1500nm). The dynamic films were deposited with homogeneous tailored percentages of porosity, in contrast the static films contained non uniform surface cracking of very low % area. Although, the FESEM and binary images reveal that the quantity surface cracks and their width generally increase with increasing thickness, the 800nm and 850nm films are exceptions to this trend. For its thickness, the 800nm film has relatively fewer cracks which reduces the total pore perimeter length and causes the percentage increase in area from the perimeter to be reduced. However, the crack widths of the 800nm film are greater than all of the films except the 1500nm film which causes the facial area porosity to be in agreement with the trend that facial porosity increases with thickness. For its thickness, the 850nm film has relatively narrow cracks that are similar in width to a 400nm film which causes the facial area porosity percentage to be reduced relative to the film's thickness. However, the 850nm film has a proportional quantity of cracks for its thickness which causes the total pore perimeter length to be in agreement with its thickness and hence the percentage increase in area from the perimeter is in agreement.

The results in Fig. 7.7 a.), b.), c.), d.) and e.) show the images of the 28-32 degree, 38-42 degree, 48-52 degree, 58-62 degree and 68-72 degree respectively. The simple area percentage of facial porosity and increase in area from the perimeter wall was calculated to be 5.2%, 103% (28-32 degree), 8.2%, 148% (38-42 degree), 19.9%,

200% (48-52 degree), 26.4%, 381% (58-62 degree) and 39.2%, 580% (68-72 degree). Glancing angle deposition was highly effective to produce a systematic increase in surface area.

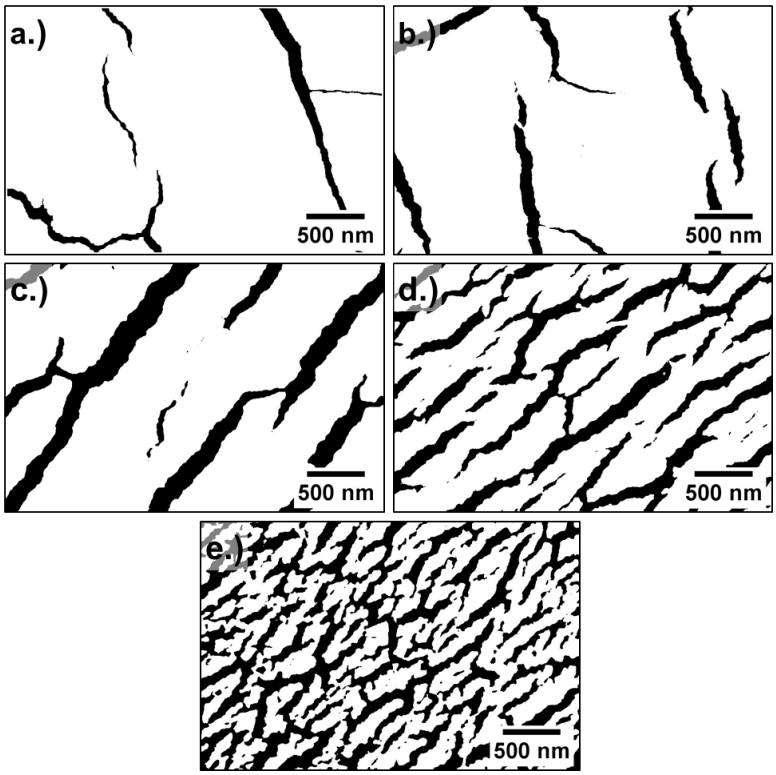

Figure 7.7: Image processing of 0.65rpm (a) 28°-32° 35kX, (b) 38°-42° 35kX, (c) 48°-52° 35kX, (d) 58°-62° 35kX and (e) 68°-72° 35kX.

7.3.3 Static Films EIS

Electrochemical Impedance Spectroscopy (EIS) was completed on the static and dynamic films with frequency range of 10^5 to 10^{-3}Hz. The capacitance plots of the static films are shown in Fig. 7.8. Capacitance from the double layer is expected to develop in the frequency range of 10 to 10^{-2} Hz and increase with decreasing frequency. As expected the figure shows a strong development of the capacitance at the lower frequencies and the general trend with image derived surface area scales

well. Fig. 7.9 shows the Nyquist plot of the static 400nm film which represents the general trend of the static films. The Nyquist plots of the static films show a lack of simple classical circuit behavior and therefore the CPE-T is required to represent the films. CPE-T was determined by Zplot software and the CPE-T values calculated were 2.82E-05(1500nm), 3.45E-06(850nm), 9.27E-06(800nm), 7.29E-06(700nm), 7.03E-06(600nm) and 2.61E-06(400nm). CPE-T verse thickness is plotted in Fig.7.10a and shows how for the static films the CPE-T value increases with increasing thickness. However, this plot can be slightly misleading because the quantity of surface cracks increase with increasing thickness, producing more interfacial area. Fig.7.10b shows the dependence of how the interfacial area increases with increasing thickness. Finally, Fig.7.10c confirms how CPE-T increases with increasing surface area from cracks developed by increasing thickness. Therefore, the CPE-T is dependent on the interfacial surface area from the cracks and not necessarily from the thickness of the film.

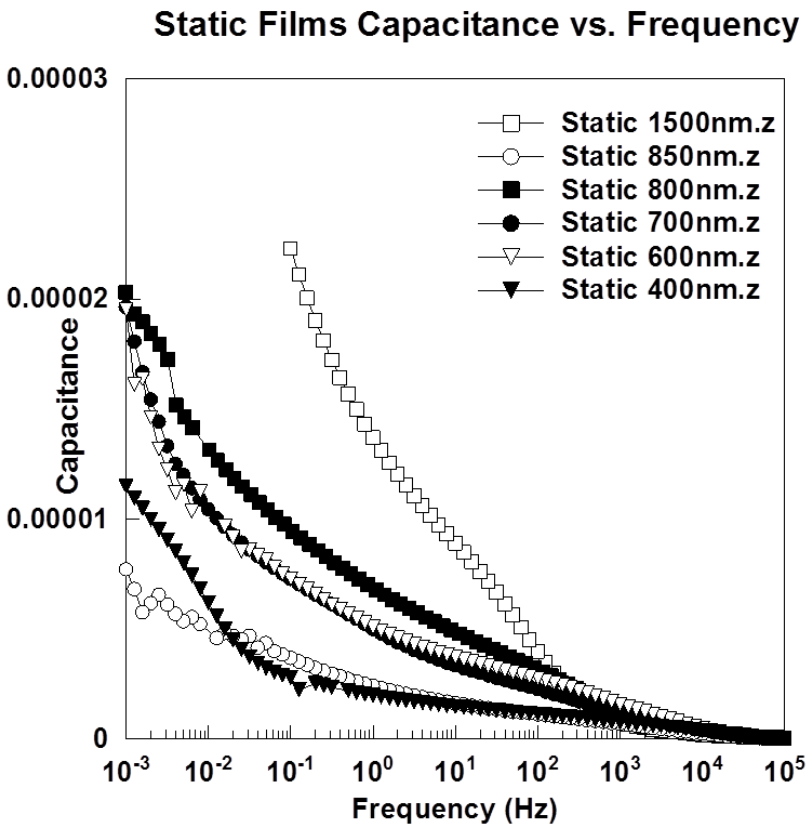

Figure 7.8: Plot of static films capacitance verse frequency

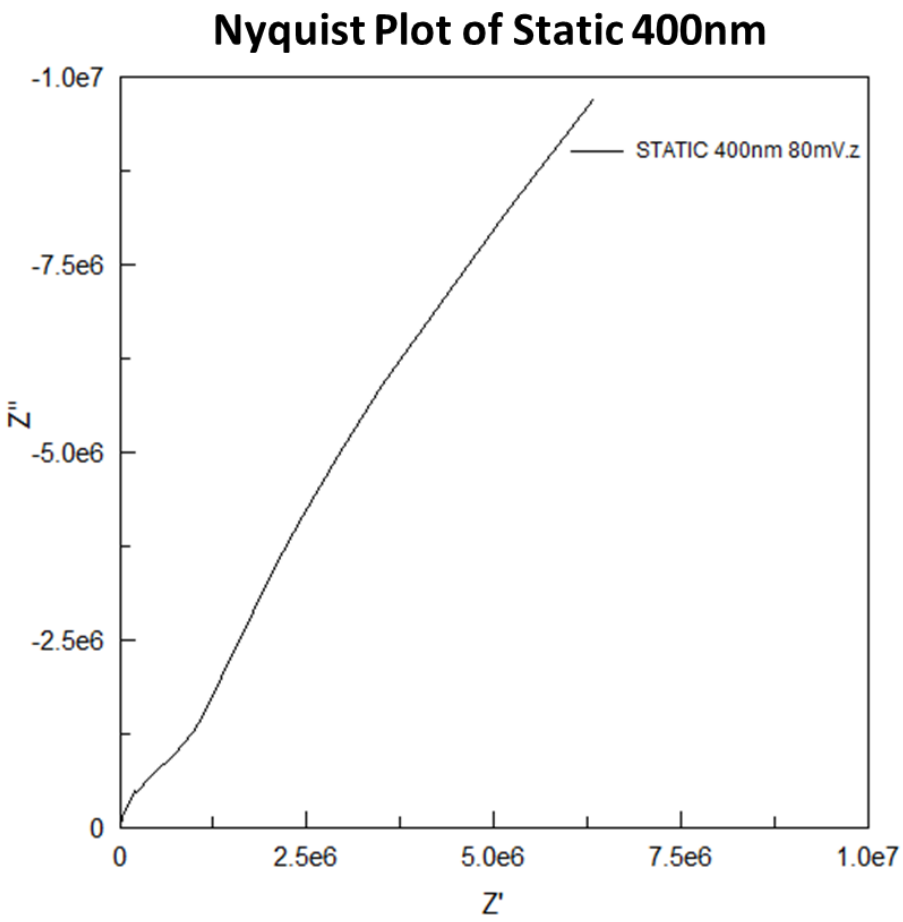

Figure 7.9: Nyquist Plot of Static 400nm

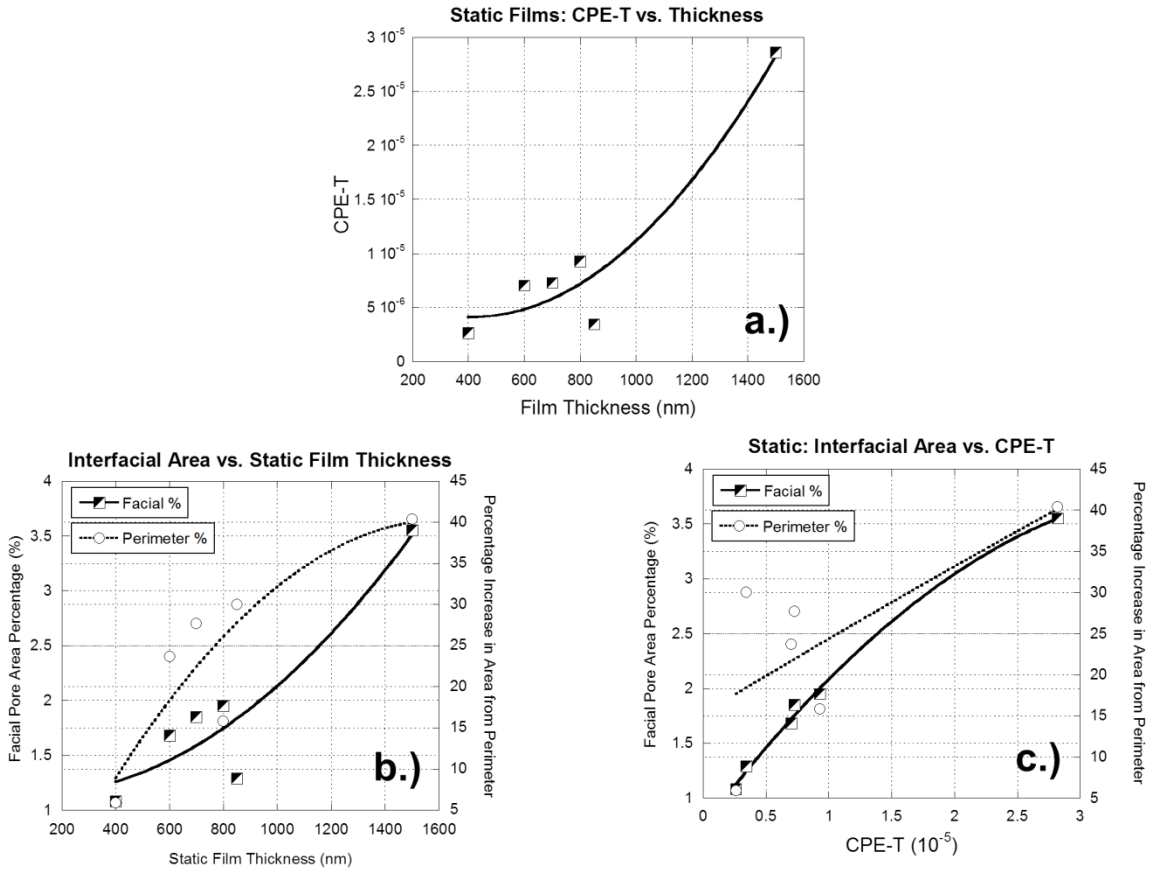

Figure 7.10: Plots of static films (a) CPE-T vs. film thickness, (b) interfacial area vs. film thickness and (c) interfacial area vs. CPE-T

7.3.3 Dynamic Films EIS

The capacitance plots of the dynamic films are shown in Fig. 7.11. Similar to the static films, the figure shows a strong development of the capacitance at the lower frequencies and the general trend scales systematically with surface area developed by the angle of deposition. Fig. 7.12 shows the Nyquist plot of the 48°-52° 700nm film which represents the general trend of the dynamic films. The dynamic Nyquist plots show a lack of simple classical circuit behavior and therefore the CPE-T is required to represent films. The CPE-T values calculated were 5.40E-05(68°-72°), 2.86E-05(58°-62°), 2.29E-05(48°-52°), 1.90E-05(38°-42°)and 1.17E-05(28°-32°). Note that the 38°-42° film's CPE-T value is out of sequence from the other films and does not accurately

reflect the film's facial or perimeter porosity percentage. There is no known explanation for this discrepancy in the data. Perhaps this film could be out of sequence due to some fabrication inconsistency.

CPE-T verse deposition angle was plotted in Fig.7.13a and shows how for the dynamic films the CPE-T value increases with increasing deposition angle. Fig.7.13b shows the dependence of how the interfacial area increases with increasing deposition angle. Finally, Fig.7.13c confirms how CPE-T increases with increasing surface area from porosity developed by the angle of deposition. Therefore, these plots clearly show how the CPE-T value is systematically dependent on the interfacial surface area produced from the pores.

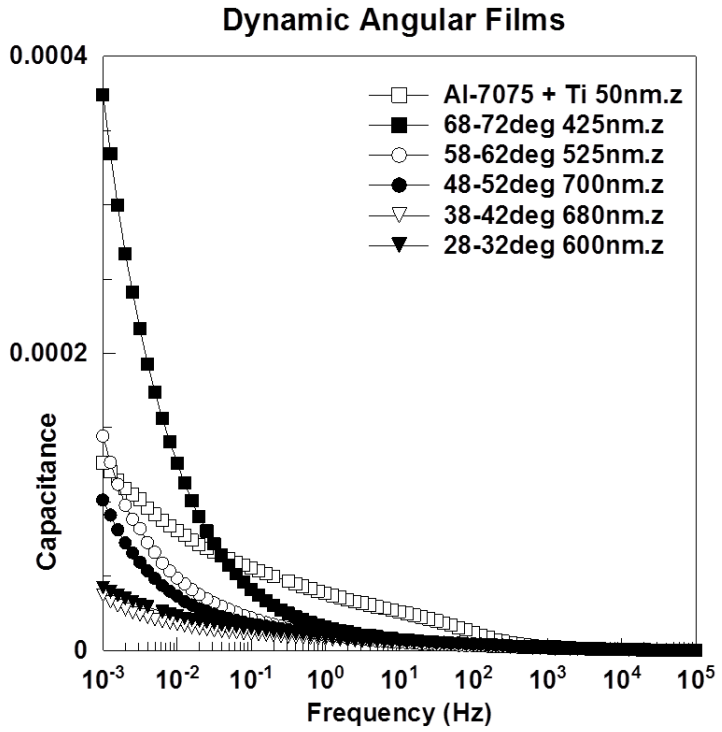

Figure 7.11: Plot of static films capacitance verse frequency

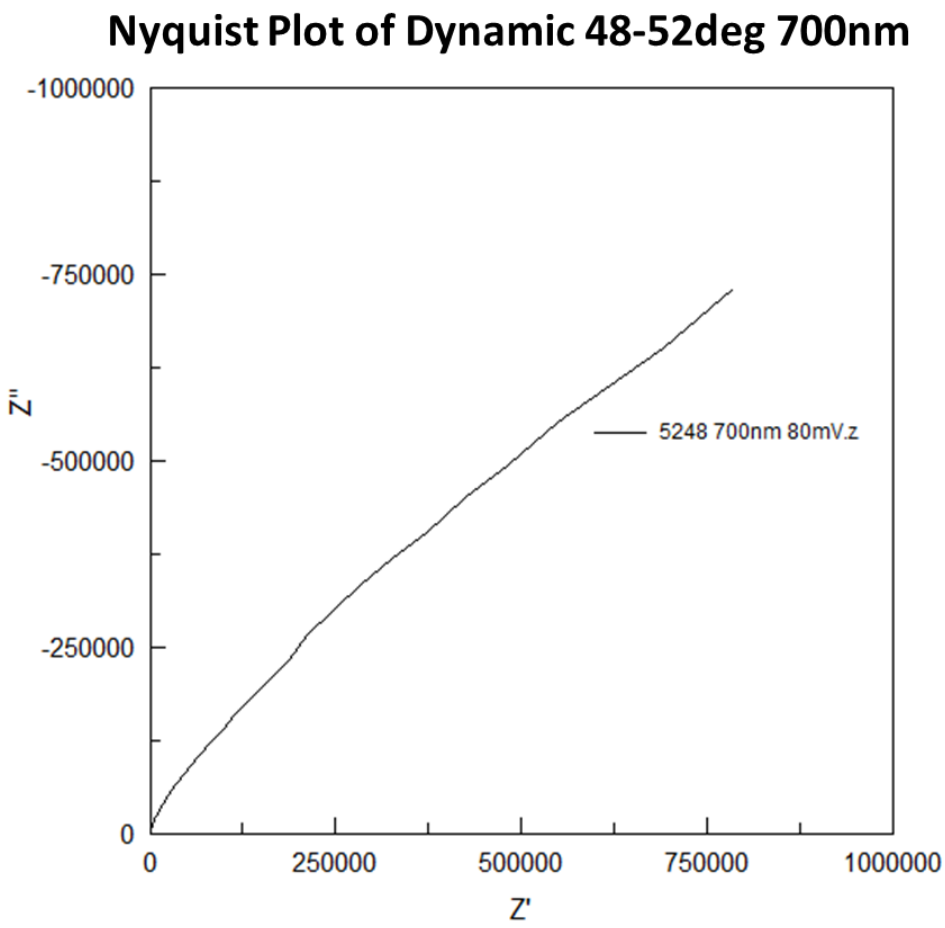

Figure 7.12: Nyquist Plot of Dynamic 48-52deg 700nm

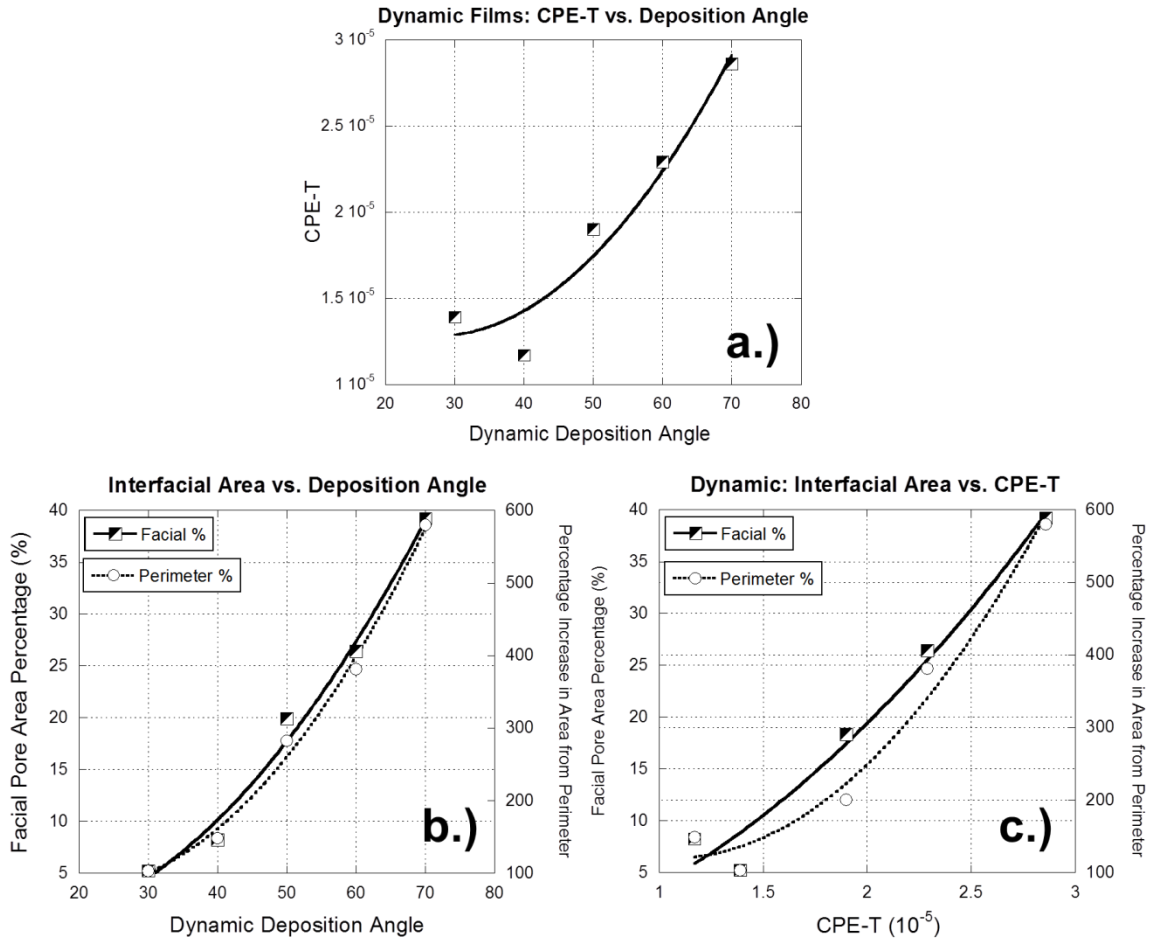

Figure 7.13: Plot of dynamic films (a) CPE-T vs. deposition angle, (b) interfacial area vs. deposition angle and (c) interfacial area vs. CPE-T

7.4 Discussion

The results show the effectiveness of using EIS and the capacitance or CPE-T value to predict static film thickness by evaluating cracks and dynamic film porosity percentage. However, examination of the capacity verse frequency plots for all the FeF_2 films reveal an ever increasing value of capacitance, even at extremely low frequencies below 10^{-3} Hz. Typical double layer capacitance rapidly reach a saturation of capacitance at values of approximately 10^{-1} Hz where the capacitance plateaus. Lower frequencies add little to the capacitance unless the porosity is of such fine dimensions it

requires the stripping of the salvation sphere around the ion of interest for the ion to enter the site. The increasing capacitance without an eventual plateau could be from a redox which might be occurring on the surface of the electrode. The studies were performed at an open circuit voltage of approximately 3V, which is well above the conversion potential of $FeF_2 \rightarrow 2\ LiF + Fe$ of approximately 2.6V. The AC sweep was limited to a very small value of 80mV that still keeps the minimum voltage value well above that of the conversion reaction. Possibilities to explain this behavior can be related to a surface and subsurface phase containing Fe^{3+} species. In this case, the reduction would occur in the 3V range. Also, there may be very fine porosity that is not readily apparent from micrographs that induce the aforementioned solvent stripping. The sample size was by far too small to allow the characterization by BET, but small angle x-ray diffraction (SAXS) and other techniques would be of use to explore to define with more precision.

7.5 Conclusion

Typically, establishing true surface area of a thin film is very tedious done through BET, this study has shown that EIS can routinely establish absolute surface area or a relative difference in surface area from a known standard. In addition, is has been shown that EIS can predict static film thickness simply based on development of a small percentage of stress cracks. The method of using EIS to predict interfacial surface area is highly beneficial. The method is faster, more cost effective, and more accurate (electrolyte accessible service will only be measured) than BET or using electron microscopy along with an imaging software. This study has shown the effectiveness of GLAD to develop films of high texture and porosity. Using the GLAD fabrication method

films with tailored percentages of increasing porosity were produced which allowed for the EIS capacitance and CPE-T to be correlated systematically.

8 Future Work

This research of applying 3D nanostructured porous electrodes to conversion reaction type batteries is only the initial work. The fact that these electrodes are 6x thicker than previous electrochemical studies with FeF_2 films yet have improved performance, has provided insight into constructing metal fluoride conversion electrodes which are limited by their wide band gap. This research has provided a new insight in improving the performance of conversion materials for researchers to consider and has opened the door for future studies using different design and fabrication techniques for producing 3D structures. Among these techniques but not limited to are template synthesis as a means of producing nanotubes, nanowires, and nanorods, other GLAD methods discussed earlier and laser etching. In addition, would be interesting to apply the GLAD fabrication method used in this study and new techniques to other conversion reaction electrode materials to better understand their reaction mechanisms and improve cycling performance. In addition, more refinement is needed in predicting porosity content in conversion electrodes by Electrochemical Impedance Spectroscopy (EIS). This will allow for a highly reliable, quick and inexpensive method to determine the porosity of conversion electrodes in the future. Metal fluorides such as FeF_2, have the potential to be relatively less expensive battery materials with high capacity. It is important to continue to increase the thickness of these electrodes, such as this study has done in order to gain greater potential energy storage and allow conversion electrodes to be more viable.

9 Summary

- A custom e-beam chamber was designed and fabricated to apply novel dynamic rotation of the substrate which can tailor the percentage of porosity in thin films.

- E-beam Deposition and aluminum substrates were used for the first time to produce metal fluoride electrodes (FeF_2) for batteries.

- The dynamic films in this study significantly improve electrochemical performance over statically produced dense films.

- The dynamic porous films were six times in magnitude thicker than previous electrochemical studies with FeF_2 films yet have improved performance.

- This study showed that the performance of conversion reaction electrodes can be improved with deep channeled porosity.

- Electrochemical Impedance Spectroscopy (EIS) can routinely establish absolute surface area or a relative difference in surface area from a known standard allowing for an alternative means to predict the percentage of porosity.

10 References

1 M. S. Whittingham , Proceedings of the IEEE , May (2012), Vol. 100.

2 R.E. Doe, K. A. Persson, Y. S. Meng, and G. Ceder, Chem. Mater. (2008), 20, 5274–5283.

3 B. Dunn, H. Kamath, J.M. Tarascon, Science, (2011), 334, 928.

4 G.G. Amatucci, N. Pereira, Journal of Fluorine Chemistry 128 (2007) 243–262.

5 A.J. Gmitter, PhD Dissertation, Rutgers, the State University of New Jersey (2012).

6 Y. Ma and S. Garofalini, J. Am. Chem. Soc. (2012), 134, 8205−8211.

7 F. Wang, R. Robert, N. Chernova, N. Pereira, F. Omenya, F. Badway, X. Hua, M. Ruotolo, R. Zhang, L. Wu, V. Volkov, D. Su, B. Key, M. S. Whittingham, C. P. Grey, G.G. Amatucci, Y. Zhu, J. Graetz, J. Am. Chem. Soc. (2011), 133, 18828–18836.

8 Yang Zhen-hua, Wang Xian-you, Liu Li, Su Xu-ping, Trans. Nonferrous Met. Soc. China 22(2012) 286−390.

9 Reinaldo Santos-Ortiz, Vyacheslav Volkov, Stefan Schmid, Fang-Ling Kuo, Kim Kisslinger, Soumya Nag, Rajarshi Banerjee, Yimei Zhu, and Nigel D Shepherd, ACS Appl. Mater. Interfaces, (2013).

10 Badway, F., Pereira, N., Cosandey, F., & Amatucci, G. G., Journal of The Electrochemical Society, (2003),150(9), A1209-A1218.

11 Liao P., MacDonald B., Dunlap R.A., & Dahn J.R, Chem. Mater., (2008), 20, 454–461.

12 Wang, F., Robert, R., Chernova, N. A., Pereira, N., Omenya, F., Badway, F. & Graetz, J., Journal of the American Chemical Society, (2011), 133(46), 18828-18836.

13 J.B. Bates, N.J. Dudney, B. Neudecker, A. Ueda, C.D. Evan, Solid State Ionics 135 (2000) 33 – 45.

14 N.J. Dudney, B.J. Neudecker, Curr. Opin. Solid State Mater. Sci. 4 (1999) 479–482.

15 N. J. Dudney, Y. Jang, Journal of Power Sources 119–121 (2003) 300–304.

16 X. Yu, J.B. Bates, G.E. Jellison, F.X. Hart, J. Electrochem. Soc. 144 (1997) 524.

17 Cairns, E. J.; Shimotake, H. Science (1969), 164, 1347.

18 Kennedy J. and Hunter, J., J. Electrochem. Soc. (1976), Volume 123, Issue 1, Pages 10-14.

19 F. Badway, A.N. Mansour, N. Pereira, J.F. Al-Sharab, F. Cosandey, I. Plitz, G.G. Amatucci, Chem. Mater. 19 (2007) 4129.

20 Yan-Hua Cui, Ming-Zhe Xue, Yong-Ning Zhou, Shu-Ming Peng, Xiao-Lin Wang, Zheng-Wen Fu, Electrochimica Acta 56 (2011) 2328–2335.

21 Zheng-Wen Fu, Chi-Lin Li, Wen-Yuan Liu, Jun Ma, Ying Wang and Qi-Zong Qin, J. Electrochem. Soc. 2005, Volume 152, Issue 2, Pages E50-E55.

22 Makimura, Y., Rougier, A., Tarascon, J.M., Applied Surface Science 252 (2006) 4587–4592.

23 P. Fiordiponti, S. Panero, G. Pistoia, C. Temperoni, J. Electrochem. Soc. 125 (1978) 511–515.

24 Gmitter, A.J., Halajko, A., Sideris, P.J., Greenbaumb, S.G., Amatucci, G.G., Electrochimica Acta 88 (2013) 735– 744.

25 Hua Zhang, Yong-Ning Zhou, Qian Sun, Zheng-Wen Fu, Solid State Sciences 10 (2008) 1166-1172.

26 F. Badway, N. Pereira, F. Cosandey, G.G. Amatucci, J. Electrochem. Soc. 150 (2003) A1318.

27 Cui Yan-Hua, Xue Ming-Zhe, Hu Ke, Li Da, Wang Xiao-Lin, Su Wei, Liu Xiao-Jiang, Meng Fan-Ming, Zheng-Wen Fu, Journal of Organic Materials, (2010), Vol 25(2).

28 S V Kuznetsov, V V Osiko, E A Tkatchenko, P P Fedorov, Russian Chemical Reviews, (2006), 75 (12) 1065 – 1082.

29 Domange, L., Ann. chinz.,(1937) 7, 225.

30 Nogues, J., Lederman, D., Moran, T.J., Schuller, I.K., Physical Review Letters, (1996), Volume 76, Number 24.

31 Yamazaki, H., Satooka, J. , RIKEN Review, Focused on Nanotechnology Review (Aug 2001), No. 38.

32 Nishizawa, M., Mukai, K., Kuwabata, S., Martin, C. R., & Yoneyama, H. (1997). Journal of the Electrochemical Society, 144(6), 1923-1927.

33 Li, N., Patrissi, C. J., Che, G., & Martin, C. R. (2000). Journal of the electrochemical Society, 147(6), 2044-2049.

34 Li, N., Martin, C. R., & Scrosati, B. (2000). Electrochemical and solid-state letters, 3(7), 316-318.

35 Fan, J., Wang, T., Yu, C., Tu, B., Jiang, Z., & Zhao, D. (2004). Advanced Materials, 16(16), 1432-1436.

36 Chan, C. K., Peng, H., Liu, G., McIlwrath, K., Zhang, X. F., Huggins, R. A., & Cui, Y. (2007). Nature nanotechnology, 3(1), 31-35.

37 Jiao, F., Bao, J., Hill, A. H., & Bruce, P. G. (2008). Angewandte Chemie, 120(50), 9857-9862.

38 Wang, Y., & Cao, G. (2008). Advanced Materials,20(12), 2251-2269.

39 Oh, S. W., Myung, S. T., Bang, H. J., Yoon, C. S., Amine, K., & Sun, Y. K. (2009). Electrochemical and Solid-State Letters, 12(9), A181-A185.

40 Zhang, Y., Liu, Y., & Liu, M. (2006). Chemistry of materials, 18(19), 4643-4646.

41 Fleischauer, M. D., Li, J., & Brett, M. J. (2009). Journal of The Electrochemical Society, 156(1), A33-A36.

42 Pröll, J., Kohler, R., Adelhelm, C., Bruns, M., Torge, M., Heißler, S., Pfleging, W. (2011, February). In Proc. SPIE (Vol. 7921, p. 79210Q).

43 Bettge, M., Ryu, S. Y., MacLaren, S., Burdin, S., Petrov, I., Yu, M. F., Abraham, D. P. (2012). Journal of Power Sources.

44 Arthur, T. S., Bates, D. J., Cirigliano, N., Johnson, D. C., Malati, P., Mosby, J. M., Dunn, B. (2011). MRS bulletin, 36(07), 523-531.

45 O. Barbieri, M. Hahn, A. Herzog, and R. Kötz, Carbon, 43, 1303 (2005).

46 M. Endo, T. Maeda, T. Takeda, et al., J. Electrochem. Soc., 148, A910 (2001).

47 G. Salitra, A. Soffer, L. Eliad, Y. Cohen, D. Aurback, J. Electrochem. Soc., 147, 2486 (2000).

48 H. Tamai, M. Kouzu, M. Morita, H. Yasuda, Electrochem. Solid-State Lett. 6 (2003) A214.
49 Y. Yamada, O. Tanaike, T. T. Liang, H. Hatori, S. Shiraishi, A. Oya, Electrochem. Solid-State Lett. (2002) A283.
50 S. Yoon, J. Lee, T. Hyeon, S.M. Oh, J. Electrochem. Soc. 147 (2000) 2507.
51 Yu, Y., Gu, L., Dhanabalan, A., Chen, C. H., & Wang, C. (2009). Electrochimica Acta, 54(28), 7227-7230.
52 Leng, Y., Chan, S. H., & Liu, Q. (2008). International Journal of Hydrogen Energy, 33(14), 3808-3817.
53 Da Silva, L. M., Fernandes, K. C., De Faria, L. A., & Boodts, J. F. (2004). Electrochimica acta, 49(27), 4893-4906.
54 Opitz, A. K., & Fleig, J. (2010). Solid State Ionics, 181(15), 684-693.
55 Robyr, C., Agarwal, P., Mettraux, P., & Landolt, D. (1997). Thin solid films, 310(1), 87-93.
56 P. Simon, A. Burke, the Electrochemical Society Interface, Spring 2008.
57 F. Lisdat, D. Schäfer Anal Bioanal Chem (2008) 391:1555–1567.
58 C.Gabrielli, Solartron Analytical, Technical Report (1998) 004/83, Issue 3.
59 J. B. Jorcin, M. E. Orazem, N. Pébère, B. Tribollet, Electrochimica Acta 51 (2006) 1473–1479.
60 J. N. Barisci, G. G. Wallace, D. Chattopadhyay, F. Papadimitrakopoulos, R. H. Baughmanc, Journal of The Electrochemical Society, (2003), 150, E409-E415.
61 MIT OpenCourseWare, Electrochemical Energy Systems, Spring 2011.
62 D. Qu, Journal of Power Sources (2001), 102, 270–276.
63 J. M. Lafferty, Foundations of vacuum science and technology, New York: Wiley, 1998.
64 D. Mattox, Handbook of physical vapor deposition (PVD) processing, Elsevier Inc., 2010.
65 D. L. Smith, Thin-film deposition: principles and practice, New York: McGraw-Hill, 1995.
66 Brooks Automation CTI-Cryogenics Owner's Manual.
67 Vacuum Technology,(2002), 60A & 60B p171-212.
68 E.Chen, Applied Physics 298r Lecture Notes, (4-12-2004).
69 http://groups.ist.utl.pt/rschwarz/rschwarzgroup_files/PLD_files/PLD.htm.
70 http://www.iestechsales.com.
71 www.wfu.edu/~ucerkb/Nan242/L11-Thin_Film_Growth.pdf.
72 Glancing Angle Deposition Research Group, University of Alberta, http://www.ece.ualberta.ca/~glad/glad.html
73 Y.-P. Zhao, D.-X. Ye, G.-C. Wang and T.-M. Lu, Proceedings of SPIE, (2003), Vol. 5219 Nanotubes and Nanowires pages 59-73.
74 B. Dick, M. J. Brett, T. Smy, J. Vac. Sci. Technol., (Nov/Dec 2003) B 21, 6.
75 Ormec Servo Motion Controller User Manual, 1995.
76 http://prism.mit.edu/xray/Basics%20of%20X-Ray%20Powder%20Diffraction.pdf.
77 http://www.lesker.com.

78 Rougier, Y. Makirnura, N. Penin, X. Darok and J.-M. Tarascon, M. J. Condensed Mater, (January 2006), Volume7, number 1.

79 M. R. Fitzsimmons, C. Leighton, J. Nogue´s, A. Hoffmann, Kai Liu, C. F. Majkrzak, J. A. Dura, J. R. Groves, R. W. Springer, P. N. Arendt, V. Leiner, H. Lauter, Ivan K. Schuller, Physical Review B, Volume 65, 134436.

80 M. Birkholz, J. Appl. Cryst. (2007). 40, 735–742.

81 H-R Wenk1 and P Van Houtte, Rep. Prog. Phys., (2004), 67, 1367–1428.

82 J. Nogue´s, T. J. Moran, D. Lederman, I. K. Schuller, K. V. Rao, Physical Review B, (March 1999),Volume 59, Number 10.

83 Poizot, P., Laruelle, S., Grugeon, S., Dupont, L., & Tarascon, J. M. (2000). Nano-sized transition-metal oxides as negative-electrode materials for lithium-ion batteries. Nature, 407(6803), 496-499.

84 Grugeon, S., Laruelle, S., Herrera-Urbina, R., Dupont, L., Poizot, P., & Tarascon, J. M. (2001). Particle size effects on the electrochemical performance of copper oxides toward lithium. Journal of The Electrochemical Society, 148(4), A285-A292.

85 Bervas, M., Badway, F., Klein, L. C., & Amatucci, G. G. (2005). Bismuth fluoride nanocomposite as a positive electrode material for rechargeable lithium batteries. Electrochemical and Solid-State Letters, 8(4), A179-A183.

86 Tarascon, J. M., Grugeon, S., Morcrette, M., Laruelle, S., Rozier, P., & Poizot, P. (2005). New concepts for the search of better electrode materials for rechargeable lithium batteries. Comptes Rendus Chimie, 8(1), 9-15.

87 Amatucci, G. G., & Pereira, N. (2007). Fluoride based electrode materials for advanced energy storage devices. Journal of Fluorine Chemistry, 128(4), 243-262.

88 Débart, A., Dupont, L., Patrice, R., & Tarascon, J. M. (2006). Reactivity of transition metal (Co, Ni, Cu) sulphides versus lithium: The intriguing case of the copper sulphide. Solid state sciences, 8(6), 640-651.

89 Ji, X., & Nazar, L. F. (2010). Advances in Li–S batteries. J. Mater. Chem., 20(44), 9821-9826.

90 Pralong, V., Leriche, J. B., Beaudoin, B., Naudin, E., Morcrette, M., & Tarascon, J. M. (2004). Electrochemical study of nanometer Co< sub> 3</sub> O< sub> 4</sub>, Co, CoSb< sub> 3</sub> and Sb thin films toward lithium. Solid State Ionics, 166(3), 295-305.

91 Taberna, P. L., Mitra, S., Poizot, P., Simon, P., & Tarascon, J. M. (2006). High rate capabilities Fe3O4-based Cu nano-architectured electrodes for lithium-ion battery applications. Nature materials, 5(7), 567-573.

92 Balaya, P., Li, H., Kienle, L. & Maier, J. (2003). Fully reversible homogeneous and heterogeneous Li-storage in RuO2 with high capacity. Adv. Funct. Mater. 13, 621–625.

93 Badway, F., Cosandey, F., Pereira, N., & Amatucci, G. G. (2003). Carbon metal fluoride nanocomposites high-capacity reversible metal fluoride conversion materials as rechargeable

positive electrodes for Li batteries. Journal of The Electrochemical Society, 150(10), A1318-A1327.

94 Nishijima, M., Gocheva, I. D., Okada, S., Doi, T., Yamaki, J. I., & Nishida, T. (2009). Cathode properties of metal trifluorides in Li and Na secondary batteries. Journal of Power Sources, 190(2), 558-562.

95 Pereira, N., Klein, L. C., & Amatucci, G. G. (2002). The Electrochemistry of Zn3 N 2 and LiZnN A Lithium Reaction Mechanism for Metal Nitride Electrodes. Journal of The Electrochemical Society, 149(3), A262-A271.

96 Pereira, N., Balasubramanian, M., Dupont, L., McBreen, J., Klein, L. C., & Amatucci, G. G. (2003). The electrochemistry of germanium nitride with lithium. Journal of The Electrochemical Society, 150(8), A1118-A1128.

97 Pralong, V., Souza, D. C. S., Leung, K. T., & Nazar, L. F. (2002). Reversible lithium uptake by CoP< sub> 3</sub> at low potential: role of the anion. Electrochemistry communications, 4(6), 516-520.

98 Silva, D. C. C., Crosnier, O., Ouvrard, G., Greedan, J., Safa-Sefat, A., & Nazar, L. F. (2003). Reversible lithium uptake by FeP2. Electrochemical and solid-state letters, 6(8), A162-A165.

99 Badway, F., Pereira, N., Cosandey, F., & Amatucci, G. G. (2003). Carbon-Metal Fluoride Nanocomposites Structure and Electrochemistry of. Journal of The Electrochemical Society, 150(9), A1209-A1218.

100 Wang, F., Robert, R., Chernova, N. A., Pereira, N., Omenya, F., Badway, F., ... & Graetz, J. (2011). Conversion Reaction Mechanisms in Lithium Ion Batteries: Study of the Binary Metal Fluoride Electrodes. Journal of the American Chemical Society, 133(46), 18828-18836.

101 Ko, J. K. (n.d.). FeF2 conductivity measurement study. Rutgers University.

102 Robbie, K., & Brett, M. J. (1997). Sculptured thin films and glancing angle deposition: Growth mechanics and applications. Journal of Vacuum Science & Technology A: Vacuum, Surfaces, and Films, 15(3), 1460-1465.

103 Robbie, K., Sit, J. C., & Brett, M. J. (1998). Advanced techniques for glancing angle deposition. Journal of Vacuum Science & Technology B: Microelectronics and Nanometer Structures, 16(3), 1115-1122.

104 Makimura, Y., Rougier, A., & Tarascon, J. M. (2006). Pulsed laser deposited iron fluoride thin films for lithium-ion batteries. Applied surface science, 252(13), 4587-4592.

105 Ma, Y., & Garofalini, S. H. (2012). Atomistic Insights into the Conversion Reaction in Iron Fluoride: A Dynamically Adaptive Force Field Approach. Journal of the American Chemical Society, 134(19), 8205-8211.

106 Liao P., MacDonald B., Dunlap R.A., & Dahn J.R (2008). Combinatorially Prepared [LiF]1-xFex Nanocomposites for Positive Electrode Materials in Li-Ion Batteries. Chem. Mater., 20, 454–461.

107 Wang, F., Yu, H. C., Chen, M. H., Wu, L., Pereira, N., Thornton, K., Graetz, J. (2012). Tracking lithium transport and electrochemical reactions in nanoparticles. Nature Communications, 3, 1201.

108 Li, N., Martin, C. R., & Scrosati, B. (2000). A High-Rate, High-Capacity, Nanostructured Tin Oxide Electrode. Electrochemical and solid-state letters, 3(7), 316-318.

109 Wu, M. S., Chiang, P. C. J., Lee, J. T., & Lin, J. C. (2005). Synthesis of manganese oxide electrodes with interconnected nanowire structure as an anode material for rechargeable lithium ion batteries. The Journal of Physical Chemistry B, 109(49), 23279-23284.

110 A.J. Gmitter, F. Badway, S. Rangan, R.A. Bartynski, A. Halajko, N. Pereira, G.G. Amatucci, (2010), Formation, dynamics, and implication of solid electrolyte interphase in high voltage reversible conversion fluoride nanocomposites, Journal of Materials Chemistry 20, 4149.

111 Gmitter, A. J., Halajko, A., Sideris, P. J., Greenbaum, S. G., & Amatucci, G. G. (2012). Subsurface diffusion of oxide electrolyte decomposition products in metal fluoride nanocomposite electrodes. Electrochimica Acta.

112 Qian, X., Gu, N., Cheng, Z., Yang, X., Wang, E., & Dong, S. (2001). Impedance study of (PEO)< sub> 10</sub> LiClO< sub> 4</sub>–Al< sub> 2</sub> O< sub> 3</sub> composite polymer electrolyte with blocking electrodes. Electrochimica acta, 46(12), 1829-1836.

113 Fekry, A. M., Gasser, A. A., & Ameer, M. A. (2010). Corrosion protection of mild steel by polyvinylsilsesquioxanes coatings in 3% NaCl solution. Journal of applied electrochemistry, 40(4), 739-747.

114 Jarjoura, G., & Kipouros, G. J. (2006). Effect of nickel on copper anode passivation in a copper sulfate solution by electrochemical impedance spectroscopy. Journal of applied electrochemistry, 36(6), 691-701.

115 Eldarrat, A. H., Wood, D. J., Kale, G. M., & High, A. S. (2007). Age-related changes in ac-impedance spectroscopy studies of normal human dentine. Journal of Materials Science: Materials in Medicine, 18(6), 1203-1210.

116 Proskuryakov, Y. Y., Durose, K., Taele, B. M., & Oelting, S. (2007). Impedance spectroscopy of unetched CdTe/CdS solar cells—equivalent circuit analysis. Journal of Applied Physics, 102(2), 024504-024504.

117 Macdonald, J. R. (1987). Impedance spectroscopy and its use in analyzing the steady-state AC response of solid and liquid electrolytes. Journal of electroanalytical chemistry and interfacial electrochemistry, 223(1), 25-50.

11 Curriculum vitae

EDUCATION

Doctor of Philosophy Material Science and Engineering May 2013	Rutgers, the State University of New Jersey New Brunswick, NJ
Master of Engineering in Automotive Engineering	University of Michigan Ann Arbor, MI
Bachelor of Science in Mechanical Engineering	Michigan Technological University Houghton, MI

INDUSTRY EXPERIENCE

Design Engineer	Toyota Technical Center, Ann Arbor, MI
Design Engineer	Honda Research and Development, Raymond, OH
Product Engineer	Chrysler Technical Center, Auburn Hills, MI

COMMERCIALIZED INDUSTRY PATENTS

1.) US Patent 8,308,226: Parkinson Matthew Frank, Steinbrecher Robert Charles; November 13, 2012; Toyota Motor Engineering & Manufacturing North America, Inc.

2.) US Patent 8,196,987: Parkinson Matthew Frank, Steinbrecher Robert Charles; June 12, 2012; Toyota Motor Engineering & Manufacturing North America, Inc.

3.) US Patent 8,167,347: Parkinson Matthew Frank, Steinbrecher; Robert Charles; May 1, 2012; Toyota Motor Engineering & Manufacturing North America, Inc.

4.) US Patent 8,011,714: Parkinson Matthew Frank, Steinbrecher Robert Charles, Dhamrat Hamshivraj Singh, Deming; William; September 6, 2011; Toyota Motor Engineering & Manufacturing North America, Inc.

5.) US Patent 7,823,947: Parkinson Matthew Frank, Steinbrecher Robert Charles; November 2, 2010; Toyota Motor Engineering & Manufacturing North America, Inc.

6.) US Patent 11,609,479: Matt Parkinson, Yukio Akimoto, John Hwang; June 21, 2007; Honda Motor Co. Ltd.

PUBLICATIONS AND PRESENTATIONS

- Parkinson M., Ko J., Halajko A., Sanghvia S. and Amatucci G.G. Effect of Vertically Structured Porosity on Electrochemical Performance of FeF2 Films for Lithium Batteries. Journal of Materials Chemistry A. (Submitted March 2013).

- Parkinson M., Vaning B., Gural J., and Amatucci G.G. Design of a Servo Controlled Rotating Substrate Drum Containing Deposition Height Adjustment. 54th Annual Society of Vacuum Coaters Technical Conference, Chicago, IL April 16–21, 2011.